10-18-2017 9:30 AM

Comparison of DC Motors and Dielectric Elastomer Actuators For Wearable Wrist Exoskeletons

Myles Lidka, *The University of Western Ontario*

Supervisor: Dr. Ana Luisa Trejos, *The University of Western Ontario*

A thesis submitted in partial fulfillment of the requirements for the Master of Engineering Science degree in Electrical and Computer Engineering

Comparison of DC Motors and Dielectric Elastomer Actuators for Wearable Wrist Exoskeletons

Myles Lidka

M.E.Sc. Thesis, 2017

Department of Electrical and Computer Engineering

The University of Western Ontario

Abstract

Paralysis or loss of strength resulting from stroke requires patients to undergo extensive rehabilitation therapy. It is known that intensive therapy contributes significantly to recovery, but as the number of surviving stroke patients increases, it is difficult for clinics to provide patients with the optimal level of therapy. Robotic devices for wrist rehabilitation have been developed to lessen these problems, but at the moment they are physically large and must be used within a clinical setting. More benefit could be obtained if the devices were portable, so that they could be used by the patients on a daily basis. To reduce the size of these devices, other means of actuation need to be considered, as currently DC motors and the required transmission are too large and heavy. Dielectric elastomer actuators (DEAs) may provide a solution to the actuation problem.

The focus of this thesis was to compare DC motors with DEAs for use in a wearable wrist exoskeleton to assist with stroke rehabilitation. A simple setup of the forearm, wrist, and hand was developed for testing DC motors and DEAs. For testing the DC motors, kinematic and dynamic models of the arm were created to develop an inverse dynamics controller used to control the movement of the hand. DEAs were fabricated and tested to determine their capabilities in terms of force and range of motion. Based on the data collected, an electromechanical model was optimized to characterize the behavior of the DEAs.

The results show that a single DEA strip of reasonable dimensions is not capable of providing the force or range of motion required for a wearable wrist exoskeleton. Future work can be done to improve DEA design so that they may actuate a wearable wrist exoskeleton or could also be considered for use in other wearable rehabilitation devices.

Keywords: dielectric elastomer actuator, electroactive polymer, exoskeleton, rehabilitation, stroke.

Acknowledgements

First and foremost, I would like to thank my supervisor, Dr. Ana Luisa Trejos. She has always been able to provide much needed guidance and support throughout these past three years. She was able to help me keep going when I didn't think I could, and has helped me grow as an engineer and a person. I would not have completed my thesis without her, and I will always be grateful for everything she has done.

The work in this thesis was funded by the Ontario Graduate Scholarship (OGS), the Natural Sciences and Engineering Research Council (NSERC) of Canada under grant RGPIN-2014-03815 and by the Ontario Ministry of Economic Development, Trade and Employment and the Ontario Ministry of Research and Innovation through the Early Researcher Award (A.L. Trejos).

I want to thank Eugen Porter of the Western University Electronics shop for making parts with the laser cutter, and for helping me find a safe way to test the DEAs. Thanks go to Abelardo Escoto for assisting with the mechanical design and for 3D printing parts. I would also like to thank Yue Zhou for providing help with the motors, 3D printing, and more. I would like to thank everyone who currently is or has been part of the Wearable Biomechatronics Lab, especially Jacob Tryon for not realizing I was the one who made his CD drive keep opening for the past ten months.

I am very thankful to Dr. Aaron Price for helping me learn about EAPs, giving advice, and for allowing me to use his lab to fabricate the DEAs.

Lastly, I want to thank my parents, Sandy and Richard, and my sister Michelle, for their constant love and support.

Contents

List of Figures

List of Tables

Nomenclature and Acronyms

Acronyms

DEA	Dielectric Elastomer Actuator
DH	Denavit–Hartenberg
DOF	Degree of Freedom
EAP	Electroactive Polymer
FE	Flexion–Extension
IMU	Inertial Measurement Unit
PS	Pronation–Supination
RMS	Root Mean Square
UR	Ulnar–Radial

Variables

$C(q, \dot{q})$	Christoffel Symbols
c_m	Center of mass
D	Inertia matrix of the manipulator
G(q)	Gravitational energy
J	Manipulator Jacobian
l	Length
m	Mass

P	Force
q_i	Angle of Joint i
t	Thickness
w	Width
W_s	Strain energy density
η	Efficiency
ε_r	Relative permittivity
λ_i	Stretch ratio
σ_i	Stress in direction i
τ	Torque
μ_i	Material parameter for Ogden model

Units

cm	Centimetres
g	Grams
kg	Kilograms
kPa	Kilopascals
mm	Millimetres
MPa	Megapascals
N	Newton
V	Volts
°	degrees

Chapter 1

Introduction

Stroke is a leading cause for long-term disability in the United States. Approximately 795,000 people suffer a stroke each year in the United States, which resulted in a combined direct and indirect cost of approximately $68.9 billion in 2009 [4], and it was estimated that 405,000 Canadians were experiencing the effects of a stroke in 2013 [5]. A stroke is caused by a disturbance of blood supply to the brain. This disturbance can be from a lack of blood caused by a blood clot or from internal bleeding in the brain. Stroke results in damage to cortical tissue, which leads to reduced or absent motor control in the upper limbs [6]. Following a stroke, up to 75% of survivors become mentally or physically disabled [7] and require rehabilitation to regain control of the affected side of their body. By undergoing rehabilitation, stroke patients are able to regain some or all motor function due to neural plasticity. Unfortunately, the rehabilitation process is intensive and expensive and many patients have difficulties complying with the required protocol. By not performing the required exercises, motor function in the affected limb does not improve. Technological advances that can provide daily therapy may provide a solution to these problems.

1.1 Motivation

Classical rehabilitation usually involves asking the patient perform task-oriented repetitive motions to improve muscle strength and coordination [8]. The effectiveness of the rehabilitation is dependent on the duration and intensity of the exercises, and the effort put forth by the patient.

In traditional rehabilitation, the therapist assists the patient with the required exercises, which are labour intensive for the therapists. This increases the cost and can cause the duration of the exercises to be shorter than they should be [9]. The use of robotics in rehabilitation has been growing to help counteract these problems [10] by providing consistent movements that mimic what the therapist would do to assist and guide the patient's limbs during exercises.

However, most robotic devices developed for rehabilitation are required to be used in a clinic. Ideally, a rehabilitation device would be wearable and portable so that patients can take the device home to assist with their rehabilitation exercises. Unfortunately, the actuators and transmission required to actuate the devices make them large and heavy, such that they can only be used in a clinical setting. Work has been done to reduce their size and weight to improve their portability. For this, other methods of actuation need to be considered to reduce their weight and size.

1.2 General Problem Statement

A majority of stroke patients suffer from hemiparesis, a weakness on one side of their body. The patients can undergo rehabilitation to improve their condition, but it is time consuming and tiring for both the patient and the therapist, and requires the patient to attend a clinic multiple times a week. Robotic devices have been developed that are able to assist with rehabilitation [11], but the actuation and transmission for these devices are large and heavy.

This work proposes that methods of actuation other than DC motors should be considered to reduce the size of wearable wrist exoskeletons. One possible actuator to do this is a dielectric elastomer actuator (DEA).

1.3 Research Objectives

The main goal of this thesis is to compare the actuation of DEAs and DC motors for wrist rehabilitation exoskeletons. To achieve this goal, work has been done towards implementing DC motors for a wearable wrist exoskeleton to evaluate their performance, and designing and building DEAs to be used for a wearable wrist exoskeleton and evaluating their performance.

To evaluate DC motors for a wearable wrist exoskeleton, the objectives were the following:

- Identify specifications for a model of the arm for testing the actuators.
- Develop a kinematic and dynamic model of the arm.
- Design and build a device to test the use of DC motors for a wearable wrist exoskeleton.
- Design a controller for the device.
- Evaluate the performance of DC motors for providing wrist flexion–extension and ulnar–radial deviation.

To evaluate DEAs for a wearable wrist exoskeleton, the objectives were the following:

- Determine a method for fabricating DEAs.
- Determine an appropriate size and shape of the DEAs for a wrist rehabilitation device
- Evaluate the force and range of motion that the DEAs are capable of providing.
- Optimize a model for DEAs based on the data collected from the experiment.

Once all those objectives have been completed, the performance of DC motors and DEAs for use in a wearable wrist exoskeleton can be compared.

1.4 Overview of the Thesis

Chapter 2 Literature Review: A review of wrist rehabilitation methods, devices that have been developed to assist with wrist rehabilitation, and a review of electroactive polymers with a focus on dielectric elastomers.

Chapter 3 Electric Motor Design and Testing Setup: Includes the design of an arm for testing, the design for testing motors for wrist rehabilitation, determining the kinematics and dynamics of the arm, and designing a controller for the motor setup. This chapter also includes an evaluation and discussion of using an IMU for getting joint positions and an evaluation and discussion on the use of the motors for wrist rehabilitation.

Chapter 4 DEA Development: This chapter includes the design of the setup for testing the DEAs, and details the process for fabricating the DEA. Also, the DEAs are evaluated, discussed, and an electromechanical model is fitted to the data.

Chapter 5 Conclusions and Future Work: Highlights the contributions of this work and proposes ideas for future work.

Appendix A Code Used: MATLAB code used for calculating the kinematics and dynamics of the arm.

Appendix B Data Sheets: Includes the data sheet for the motors used in Chapter 3.

Appendix C Permissions: Includes permission to use a figure in Chapter 2.

Chapter 2

Literature Review

This chapter presents a review of literature in the areas of wrist biomechanics, current rehabilitation methods, prior art in robotic rehabilitation devices, and smart material actuators. By reviewing the literature, design requirements for a wrist rehabilitation device were developed. Literature was searched for using Google Scholar between the time of January 2015 to July 2017. The keywords used for the searches included dielectric elastomer actuators, electroactive polymers, wrist rehabilitation devices, dielectric elastomer actuator electrodes, stroke rehabilitation, wrist rehabilitation, rehabilitation devices, wrist biomechanics, wrist anatomy, and a combination of some of those keywords. A total of 211 papers resulted of which 80 were relevant.

2.1 Wrist Rehabilitation

Most people who suffer a stroke will also suffer from weakness or partial paralysis on one side of their body, which is caused by cell death in the affected region of the brain and cell dysfunction around that area [12, 13]. This weakness or partial paralysis can make activities of daily living difficult to nearly impossible for the patient to perform by themselves depending on the severity of the stroke. Fortunately, most patients are capable of regaining some motor function due to the neuroplasticity of the brain—the brain's ability to form new neural connections [12,14]. These new neural connections can be formed through the use of different methods of rehabilitation. Some patients can also suffer from spasticity, which is where some muscles are continuously contracted

[15]. Spasticity can affect the patients' movement, their range of motion and, depending on the severity of the spasticity, it can be painful. To recover fully following a stroke, rehabilitation therapy is required, as outlined in the following section.

2.1.1 Methods of Wrist Rehabilitation

Rehabilitation between patients varies depending on the severity and location of the stroke, but treatment that involves physical therapy and occupational therapy is usually recommended [16]. Both the physical therapist and the occupational therapist aim to improve motor and sensory abilities, which can include increasing the range of motions, strengthening the muscles, improving motor coordination, and to teach the patient strategies for activities of daily living.

Therapy provided to the patient should begin as soon as the patient is stable and capable of beginning because early intervention has a significant positive effect on recovery [17, 18]. In the early stage of therapy, the therapist will move a joint in one degree of freedom by putting the patient in a safe sitting or lying position, and carefully applying a force to the limb to move it through the patient's range of motion. For the wrist, the therapist would move the patient's hand through flexion–extension and ulnar–radial deviation. Next the therapist will have the patient try to actuate a joint through a motion while the therapist assists the patient to perform the motion as needed. As the patient's motor control improves, the therapist will decrease the assistance provided. If the patient is capable of actuating the joint on their own, the therapist will then have them perform the motions on their own and will add some resistance to the movement as the patient's strength and motor control improves.

If the patient is capable of some movement with the affected limb, an effective method of rehabilitation is doing task-oriented exercises [19, 20]. Usually this involves tasks that would normally be performed during their daily life, such as opening a jar, or picking up and putting down an item. The therapist would choose the task to be done based on the patient's current level of motor function. These exercises can be done with assistance from a helper or device, or they can be done with no assistance if the patient is capable.

Therapy is often done in either an inpatient facility, outpatient facility, or at home. Details of these are as follows:

Inpatient Facility

An inpatient facility is a facility that is either part of a hospital or freestanding that a patient will stay for usually 2 to 4 weeks to receive intensive rehabilitation. Inpatient facilities have a large range of medical staff that makes it easier for patients to receive everything they need for rehabilitation. The Canadian Best Practices for Stroke Care recommends that patients at an inpatient facility receive at least 3 hours per day and 5 days per week of active rehabilitation [21].

Outpatient Facility

Similar to the inpatient facility, an outpatient facility can be part of a hospital or be freestanding with a large range of medical staff. The Canadian Best Practices for Stroke Care recommends that patients receive active therapy from the facility for 45 minutes to 3 hours per day for 3 to 5 days per week [21].

Home-Based Rehabilitation

Some patients may choose or need to receive therapy at home. Patients receiving therapy at home should also receive active therapy from the facility for 45 minutes to 3 hours per day for 3 to 5 days per week [21].

There is an increase in demand for physiotherapy due to lower stroke mortality rates, and an increase in the aging population [11]. Unfortunately there are not enough physiotherapists to provide everyone the required amount of rehabilitation. In Ontario, only 43.3 % of patients receive stroke unit care [22]. Part of the problem is that the rehabilitation is tiring and time consuming for the therapist and other methods of rehabilitation need to be considered.

2.2 State of the Art in Rehabilitation Devices

Due to the difficulties encountered in current stroke rehabilitation, it would be beneficial to consider other methods that use similar techniques and overcome some or all of the current difficulties. In recent years, researchers have been developing mechatronic devices to assist during rehabilitation of joints. By implementing robotics, it is possible to improve some aspects of the rehabilitation procedure as well as to allow for more possibilities in therapeutic treatments.

The following sections outline the existing solutions categorized according to the components

Device	Sensor(s)	Controls
EXOWRIST [23]	Linear flex sensor for angular displacement and proportional pressure regulator to measure the pressure of compressed air	PID controller
3-DOF Self-Aligning Exoskeleton [24]	Force sensors to measure torque and potentiometers to measure position	N/A
Cable-Driven Wrist Robotic Rehabilitor (CDWRR)	Orientation sensors and encoders	Closed-loop control with joint angle feedback
Articulated Rehabilitation Robot [25]	Potentiometer, motor encoder, EMG, and force sensors	Has 4 modes: PID controller, impedance controller, EMG-trigger, and a switch
RUPERT [26]	Potentiometer, and inertia sensors	N/A
Wrist Gimbal [27]	Encoders	P controller and PD controller
Upper Limb Exoskeleton Powered via Pneumatic Electric Hybrid Actuators [28]	Force Sensors	Torque based feed-forward control for gravity compensation
RiceWrist-S [8]	Encoders	PD controller, impedance controller, and a modified adaptive controller [29, 30]

Table 2.1: Sensors and controls in rehabilitation devices.

of a mechatronic system: sensors, control systems, and actuators.

2.2.1 Sensing and Control Methods

2.2.1.1 Sensors

A sensor is a device that measures a physical property then records and/or displays it in some way. The sensors required for a wearable wrist rehabilitation device are going to depend on the physical constraints of the device, and the signals required for the controller. The types of signals that might be needed for the controller are kinematic, dynamic, and EMG signals. Kinematic signals are the signals related to the position, velocity, and acceleration of the joints. Dynamic signals are signals related to the force, and torque at the joints [9]. Systems needing the joint position most often use rotary encoders or potentiometers attached at the joint and/or on the motor shaft, such

as in the devices [8,24–27] shown in Table 2.1. Another sensor often used for position is an inertial measurement unit (IMU), which measures acceleration forces, angular rate. Some IMUs measure magnetic field as well.

2.2.1.2 Control Methods

The control system manages the behaviour of the rehabilitation devices. The control system used for wrist exoskeleton devices will depend on the task that the device is being used for. Most of the devices in Table 2.1 have used a PID controller for trajectory control of each joint in the exoskeleton. The PID controller is used often because it is simple and easy to implement. For rehabilitation, the PID would likely be used as a low level controller in the control system. More complex control systems are dynamic model control systems. The dynamic model treats the limb as a mechanical system with rigid links and rotational joints in which the model will predict the torque generated from inertial, gravitational, centrifugal, and Coriolis effects [31]. The dynamic model can then be used for control systems such as an inverse dynamics controller for joint trajectory control, or an impedance controller [25] for a force interaction controller. Another type of model based controller is one that uses a muscle model. A muscle model based control system predicts the torque generated at a joint based on the muscle activation signals [32].

2.2.2 Actuation and Transmission Systems

The main requirement of the actuation systems is to be able to supply the required forces repeatedly and efficiently. A summary of the actuators that have been used for wrist rehabilitation devices is presented in Table 2.2. Actuators that have been used in wrist rehabilitation devices include electromagnetic motors [8,9,24,25,27,33–37], and pneumatic actuators [23,26] where electromagnetic motors are used much more often than other types of actuation. In rehabilitation devices for other joints, other types of actuation have been used such as hydraulic [38], shape memory alloys [39], electroactive polymers [40,41], and electrorheological fluids [42].

Most upper-arm rehabilitation devices use DC motors for actuation because they are precise and easy to obtain. A majority of researchers have used brush DC motors over brushless DC motors. Brush DC motors are generally less expensive, they are reliable, and they are easier to

Device Name	Actuation	Transmission	Torque
3-DOF Self-Aligning Exoskeleton [24]	3 Brush DC Motors	A geared differential drive mechanism and gearheads	0.15 Nm
Cable-Driven Wrist Robotic Rehabilitator [33]	4 Brush DC Motors	Cable transmission. 4 motors driving cables winded by winch	N/A
RUPERT [26]	McKibben Pneumatic Actuator	Direct drive	Shoulder, Elbow, and Wrist FE: 15Nm; Forearm PS: 3 Nm
Ricewrist-S [8]	2 Brush Motors and 1 Brushless DC Motor	Cable drive used for FE and UR deviation. Direct drive used for PS	Wrist FE: 2.805 Nm; UR Deviation: 1.058 Nm; Forearm PS: 1.68 Nm
Articulated Rehabilitation Robot [25]	DC Motors	Motors with attached gearheads are attached directly to the joint	N/A
InMotion Wrist [9]	3 Brushless DC Motors	Uses a geared differential drive mechanism	N/A
Wrist Gimbal [27]	3 Brush DC Motors	Cable and pulley	Wrist FE and UR Deviation: 1.77 Nm; Forearm PS: 2.87 Nm
MAHI EXO II [43, 44]	6 Brushless DC Motors	Cable drive mechanism	Elbow FE: 7.35 Nm; Forearm PS: 2.75 Nm; Wrist FE and UR deviation: 1.45 Nm
Gopura and Kiguchi Exoskeleton [34]	RH Mini Series Harmonic Drive Servo Motors	Geared transmission	Wrist FE and UR Deviation: 0.58 Nm; Forearm PS: 4.2 Nm
Wrist Rotation Robot [35]	Brushless DC Motor	Planetary gearhead	Forearm PS: 4.65 Nm
ETS-MARSE [36]	Brushless DC Motor	Harmonic drive gearbox	Wrist FE and UR Deviation, and Forearm PS: 5 Nm
Compact Wrist Rehabilitation Robot [37]	DC Servomotor	N/A	N/A
EXOWRIST [23]	Pneumatic Air Muscle	Direct drive	N/A
Pneumatic-Electric Hybrid Actuator [28]	Pneumatic Air Muscles and Brushless DC Motor	Low Reduction gear and Bowden Cables	Shoulder Flexion–Extension: 100Nm; Elbow FE: 76 Nm
SMA driven exoskeleton [45]	Shape Memory Alloy Actuators	Cable and Pulleys	N/A

Table 2.2: Actuation and transmissions in wrist rehabilitation devices. FE: flexion–extension, UR: ulnar–radial, PS: pronation–supination.

control than brushless motors. Brushless DC motors are generally more accurate for positioning, they are more efficient, low noise, and have a better speed/torque trade-off. The disadvantage for all DC motors is that they require mechanical coupling and transmission, which will greatly increase the weight. To avoid this, some researchers have tried using pneumatic actuators. The power to weight ratio in pneumatic actuators is much greater than electronic motors and they can usually be attached directly to where you need the force applied, which makes this very appealing. Unfortunately, the pneumatic actuators require a pressure source, which will be heavy and loud. Shape memory alloy actuators have been implemented for a wrist and forearm exoskeleton but the actuators required cooling, which was difficult to achieve as part of an exoskeleton [45].

The methods of transmissions used include gears or cables, or they are directly attached to the joint. Direct drive can be beneficial because it is simple and reduces the total size of the device, however, for the purpose of wrist rehabilitation, having an actuator at the wrist would be inconvenient and may also increase the moment at the elbow and shoulder compared to when the actuator was attached closer to the elbow. Gearheads are effective because they can increase the torque with a compact box, although, it is necessary to account for backlash from the gears, as well as the losses due to friction in the gears. Two of the devices [9, 24] use a geared differential drive mechanism, which is used to allow two motors to work together for the flexion–extension and radial–ulnar deviation of the wrist. This allows the torque required from both motors to be reduced by nearly half (there will be losses in the mechanisms) compared to having one motor. There is also a similar mechanism that uses cables instead of gears, which has been used in an elbow rehabilitation device for elbow flexion–extension and forearm pronation–supination [46].

2.2.3 Other Considerations

Apart from the sensors, actuators, and control system, the overall configuration of the devices has to be considered. Two different ways to categorize the wrist rehabilitation devices is through exoskeleton vs. end-effector, and grounded vs. ungrounded as shown in Table 2.3. An exoskeleton based robot has a structure similar to the human body part it is actuating, and also has the joints of the robot aligned with the human joints, allowing the device to actuate each joint individually [8]. In contrast, the end-effector based robot is a robot that will only apply force at one point to move

one or more joints.

Grounded devices are those that are attached to the ground, table, or wall, whereas ungrounded means that the device is not attached to anything but to the user (excluding cables). A majority of the devices listed in Table 2.3 are grounded because of the constraints required for an ungrounded device. An ungrounded device is required to be lightweight so that the user can support it, and it also needs to be small and unobtrusive so that it does not limit the movement of the user.

The summary presented below, shows that truly wearable and portable devices that could be used for home rehabilitation are lacking. Although the weight of the devices is often not reported, the fact that DC motors are used indicates that their weight would be too high for use as a wearable device. A possible solution to this problem is through the incorporation of smart materials into novel actuation systems. In particular, this thesis aims to explore the use of a special kind of material, called electroactive polymers (EAPs).

2.3 Electroactive Polymers

Electroactive polymers (EAPs) are lightweight, low cost polymers that generate a mechanical motion in reaction to an electric field allowing them to be used as actuators [48, 49]. One type is also capable of generating an electrical voltage when deformed making them possible to be used as sensors or generators [50].

2.3.1 Types of EAPs

There are two different categories of EAPs: ionic and electronic. Ionic EAPs are actuated by a displacement of ions and often causes a bending motion. Electronic EAPs are actuated by electrostatic forces between the two electrodes causing expansion in the planar direction [49]. A comparison of ionic and electronic EAPs is shown in Table 2.4.

2.3.2 Dielectric Elastomer Actuators

Dielectric elastomers are a type of electronic EAP. The main components of the dielectric elastomer is a polymer film that is soft and a good insulator, and compliant electrodes. By applying a high

Device Name	Device Type	Joints	Other Notes
3-DOF Self-Aligning Exoskeleton [24]	Grounded Exoskeleton	Wrist: FE, UR Deviation; Forearm: PS	Uses a dynamic self-aligning mechanism using linkages
Cable-Driven Wrist Robotic Rehabilitator [33]	Grounded Exoskeleton	Wrist: FE, UR Deviation; Forearm: PS	Requires the arm to be pointing down
RUPERT [26]	Ungrounded Exoskeleton	Shoulder: FE; Elbow: FE; Forearm: PS; Wrist: FE	Exoskeleton worn on the user's back held with straps around the chest
Ricewrist-S [8]	Grounded Exoskeleton	Wrist: FE, UR Deviation; Forearm: PS	N/A
Reconfigurable Rehabilitation Robot [47]	Grounded End Effector	Wrist: FE; Forearm: PS	Reconfigurable robot capable of 1 joint movement at a time. Requires adjustment of the setup to switch between joints moved
Articulated Rehabilitation Robot [25]	Grounded End Effector	Shoulder: FE, Abduction-Adduction, Internal/External Rotation; Elbow FE	Very large and heavy (23 kg)
InMotion Wrist [9]	Grounded Exoskeleton	Wrist: FE, UR Deviation; Forearm PS	A commercial device that can be used by itself or combined with the InMotion Arm. Uses a differential drive mechanism.
Wrist Gimbal [27]	Grounded Exoskeleton	Wrist: FE, UR Deviation, Forearm: PS	N/A
MAHI EXO II [43]	Grounded Exoskeleton	Wrist: FE, UR Deviation; Forearm: PS; Elbow: FE	N/A
Gopura and Kiguchi Exoskeleton [34]	Ungrounded Exoskeleton	Wrist: FE, UR Deviation; Forearm: PS	It is ungrounded but will be heavy and uncomfortable for patients to wear for extended periods of time
Wrist Rotation Robot [35]	Grounded End Effector	Forearm: PS	A simple design only capable of rotating the forearm
ETS-MARSE [36]	Grounded Exoskeleton	Shoulder: FE, Abduction-Adduction, Internal/External Rotation; Elbow FE; Forearm: PS; Wrist: FE, UR Deviation	Large exoskeleton for whole upper-arm rehabilitation
Compact Wrist Rehabilitation Robot [37]	Grounded Exoskeleton	Wrist: FE	Compact device but must be clamped to a table
EXOWRIST [23]	Ungrounded Exoskeleton	Wrist: FE, UR Deviation	Light device(430 g) but has limited range of motion

Table 2.3: General information on wrist rehabilitation devices.

	Ionic	Electronic
Voltage Requirements	Within the range of a few volts	High voltage in the kilovolt range, but small current and power
Operational State	Requires electrolyte	Dry state

Table 2.4: Comparison of ionic and electronic EAPs.

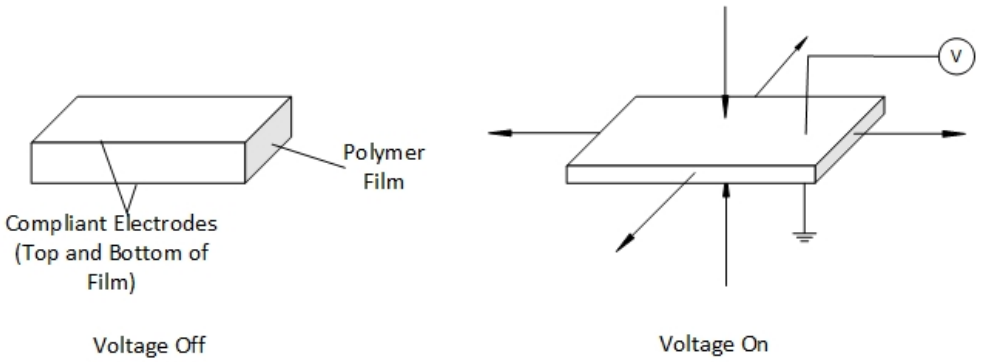

Figure 2.1: Actuation of a DEA.

voltage, usually around 1–10 kV [51, 52], the positive and negative electrodes attract each other and squeeze the polymer film causing it to stretch out, as shown in Figure 2.1. The simple design means that actuators can be made in many different ways to suit the actuation.

2.3.2.1 Review of Existing Actuators

One of the advantages of dielectric EAPs is that they can easily be tailored towards the application. Operating by expanding in the planar direction and compressing in the thickness direction help open more ways to use the dielectric EAP as an actuator. It is possible to use a dielectric EAP for linear motion, bending motion, and rotary motion. Some examples of dielectric EAP actuators are:

- Bow-tie [53]

  The bow-tie shown in Figure 2.2 has rigid spars on the ends, and each side is supported by two hinged spars. When the DEA is elongated, the hinged spars on the sides help preserve the prestrain in the direction perpendicular to the elongation. When high voltage is applied to the electrodes, it elongates in the direction shown in Figure 2.2.

- Stacked [54, 55]

  The stacked actuator shown in Figure 2.3 is made by stacking dielectric film with electrodes in between each layer of film. The electrode in the stack alternates between being connected to the high voltage supply and ground. When high voltage is applied to the electrodes, the stack compresses in the direction perpendicular to the electrodes, and expands in the direction planar with the electrodes.

- Diamond-Shaped [56]

  The diamond-shaped actuator in Figure 2.4 has legs on either side of the film that hold the prestrain. When high voltage is supplied to the electrodes, the film relaxes and the system contracts in the direction perpendicular to the electrodes.

- Rolled [57]

  The rolled actuator in Figure 2.4 is made from a prestrained dielectric film being wrapped around a compressed coil spring. When high voltage is supplied to the electrodes, the film relaxes and the spring elongates.

- Tubular [58, 59]

  The tubular actuator in Figure 2.4 is similar to the rolled actuator but it is just rolled around a cap at either end, and no spring inside. The actuator would require that some outside forces keep it in tension and would elongate when supplied high voltage.

- Planar [60, 61]

  The planar actuator in Figure 2.4 is a strip of dielectric film with an electrode on either side and is fixed at one end of the strip and the other end would attach to an object that would hold it in tension. When high voltage is supplied to the electrodes, the strip will elongate.

- Folded [62]

  The folded actuator in Figure 2.4 consists of a rigid part with arms connected by elastic hinges, and the electrode coated dielectric film on either side. Supplying a high voltage to one of the films causes the arms to bend towards the opposite side.

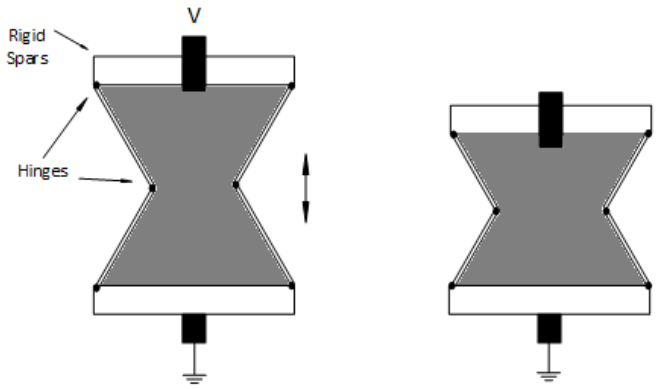

Figure 2.2: Bowtie DEA modified from [63].

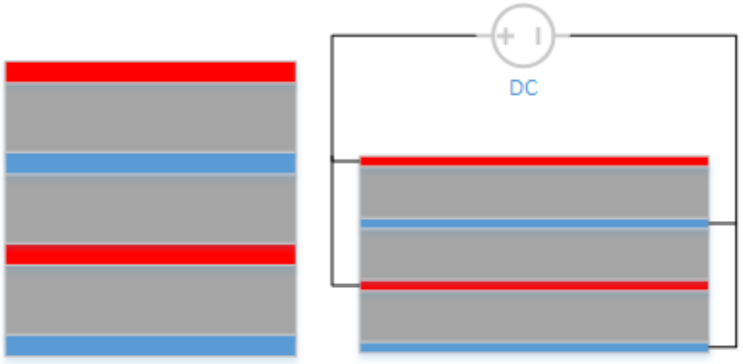

Figure 2.3: Stacked DEA modified from [64].

- Bender [49]

  The bender actuator in Figure 2.4 is made from a dielectric film that is constrained on one side. When a high voltage is supplied to the electrodes, it bends towards the side that is constrained.

In this chapter, the motivation and methods for wrist rehabilitation after stroke have been reviewed. A literature review of current mechatronic technologies for wrist rehabilitation have been presented. Most of the current devices use DC motors, which combined with the required transmission are too large and heavy for a wearable device. DEAs were reviewed to provide the required background to determine if they are a possible alternative for DC motors in a wearable wrist exoskeleton.

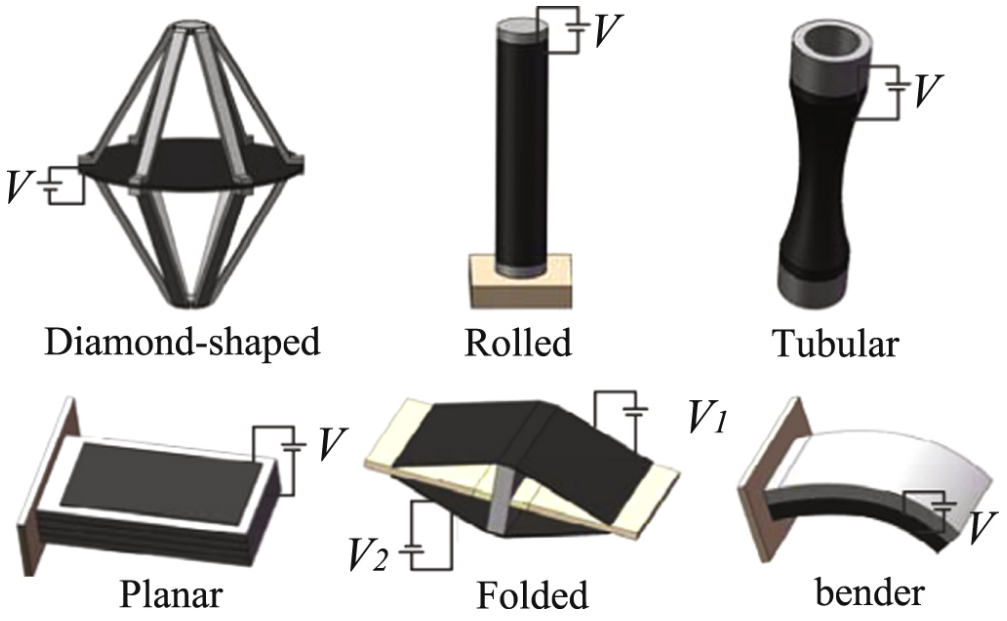

Figure 2.4: Different configurations for DEAs. Used with permission from [65].

Chapter 3

Electric Motor Design and Testing Setup

In Chapter 2, a review of wrist rehabilitation devices was performed. Nearly all the devices reviewed use DC motors for actuation. Other methods of actuation should be considered to decrease the size and weight of a wearable wrist exoskeleton. In order to do that, this chapter will test the use of DC actuators for a wearable wrist exoskeleton. The results of this chapter can be used to compare this method of actuation with dielectric elastomer actuators in the next chapter. For testing DC actuators, as well as DEAs, the first step was to develop a setup that mimics forearm and wrist motion. The requirements of such a setup rely on basic arm and hand anatomy, as presented in the following section.

3.1 Anatomy and Biomechanics

The two main motions of the wrist are flexion–extension and ulnar–radial deviation as shown in Figures 3.1 and 3.2, respectively. The average ranges of those motions can be seen in Table 3.1.

Table 3.2 displays data on the mass and center of mass of the hand. The data were gathered from 13 male cadavers from the United States of America [66], which means that the values are higher than if female cadavers had been used or cadavers from some other areas of the world. The data should still be sufficient for this study because a device that is able to assist with a heavier

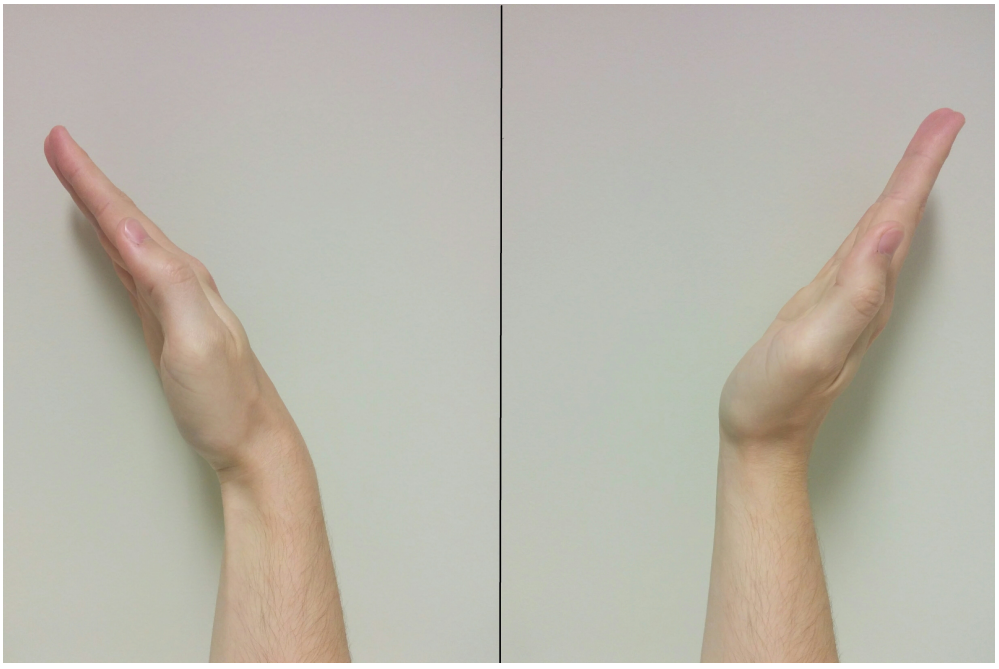

Figure 3.1: Wrist flexion (*left*) and wrist extension (*right*).

Figure 3.2: Wrist ulnar deviation (*left*) and wrist radial deviation (*right*).

Motion	Range (°)
Flexion	76.4 ± 6.3
Extension	74.9 ± 6.4
Radial Deviation	21.5 ± 4.0
Ulnar Deviation	36 ± 3.8

Table 3.1: Wrist ranges of motion [1]

	5^{th} Percentile	50^{th} Percentile	95^{th} Percentile
Mass (g)	460	530	610
Center of Mass (cm)	5.1	5.6	6.0

Table 3.2: Mass and center of mass of the hand [2, 3].

hand should also be capable of assisting a hand that is lighter. Based on these dimensions, a physical setup of the arm and hand was developed.

3.2 Physical Setup

To test DC motors, it is necessary to construct an imitation of the forearm and hand. For this setup, it was more important to replicate the joint than the actual shape of the arm and hand so the arm was made to be wider and flatter for convenience. Two joints that need to be replicated are the wrist flexion–extension and wrist ulnar–radial deviation, as the device was being designed to assist with wrist movement. The other two joints that needed to be replicated were forearm pronation–supination and elbow flexion–extension, as they affect the required torque at the wrist from the gravitational force from the hand. The forearm joint needed to be manually controlled and the joint needed to be able to be locked at set angles.

Using the 95^{th} percentile mass and center of mass in Table 3.2 represented by m_{95} and c_{95} respectively, the highest torque required to compensate for the gravitational forces of the hand, τ_g, is described by:

$$\tau_g = c_{95} m_{95} g, \Rightarrow \tau_g = 359 \text{ N·mm}. \tag{3.1}$$

For this model of the hand, two different weighted hands were used using the properties shown in

	Hand 1	Hand 2
Mass (g)	249	544
Center of Mass (cm)	7.45	6.72
Torque at the Wrist(N·mm)	182	357

Table 3.3: Mass, center of mass, and torque at the wrist for two different hands.

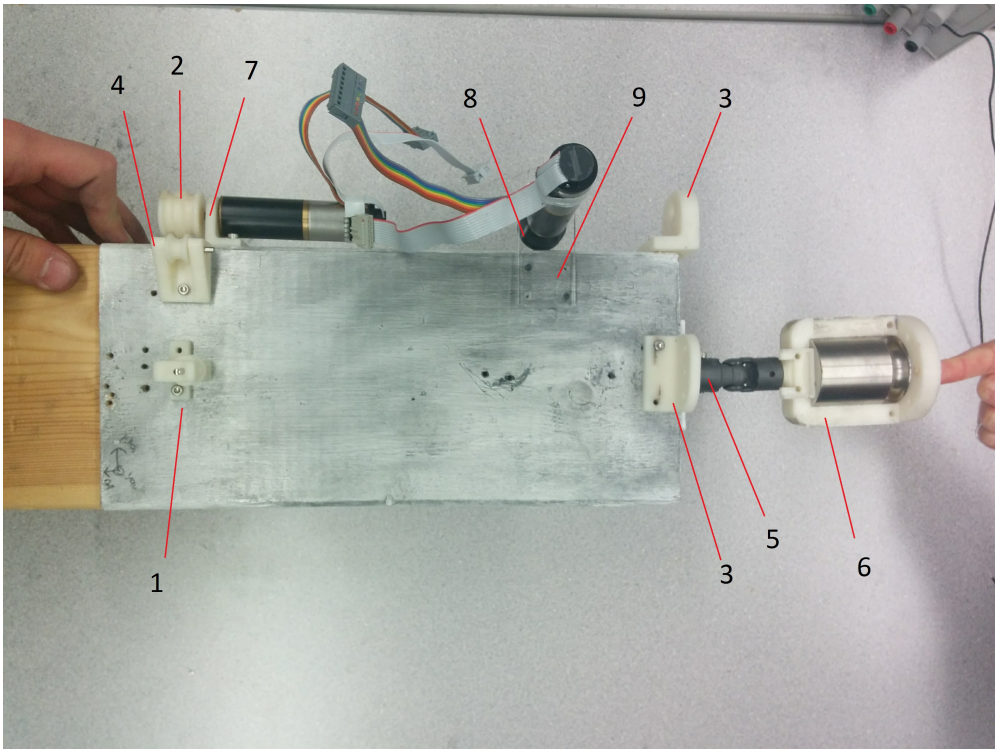

Figure 3.3: A top down view of the motor setup with the parts labels. 1. Pulley 1, 2. FE motor pulley, 3. Cable raiser, 4. Pulley 2, 5. U-joint connector, 6. Hand, 7. FE motor holder, 8. UR deviation motor pulley, 9. UR deviation motor holder.

Table 3.3.

The setup for testing the DC motors is shown in Figures 3.3 and 3.4. Each part of the DC motor setup is listed in the order as shown in Figure 3.3 and is described as follows:

1. *Pulley 1*: This part is shown in Figure 3.5.a. The pulley is used to adjust the direction of force from the cable to the hand for flexion–extension.

2. *Flexion–Extension Motor Pulley*: This part is shown in Figure 3.5.b. This pulley is attached to the shaft of the motor and has two grooves and holes so that one cable can be used for

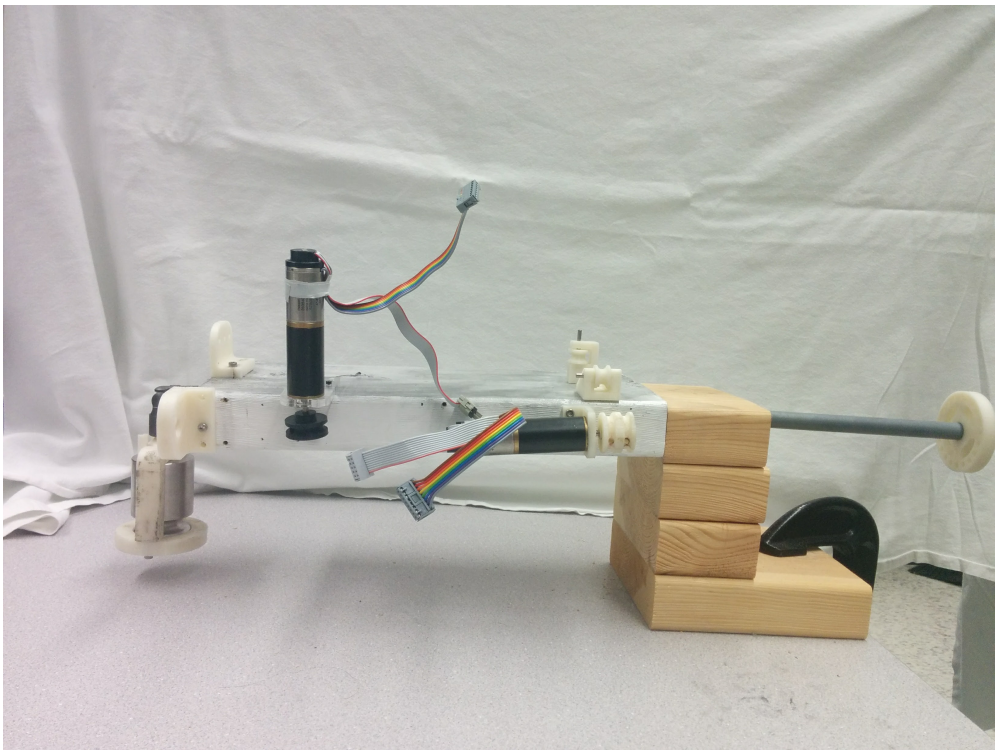

Figure 3.4: A side view of the motor setup.

flexion, and a different cable can be used for extension using the same motor.

3. *Cable Raiser*: This part is shown in Figure 3.5.c. This part is attached just before the wrist joint for both the flexion–extension joint, and the ulnar–radial deviation joint. It is used to raise and hold the cables at a certain spot. The two bottom holes are to screw the part on to the arm. The cable raiser part used for flexion–extension uses the left and right holes on the top to raise the cables. The cable raiser part used for ulnar–radial deviation uses the middle hole on the top to raise the cable.

4. *Pulley 2*: This part is shown in Figure 3.5.d. The pulley is used to adjust the direction of force from the cable to the hand for flexion–extension.

5. *U-joint Connector*: This part is shown in Figure 3.5.e. This part is screwed on to the end of the arm and has one half of the u-joint attached to it. The u-joint is used to mimic the wrist.

6. *Hand*: This part is shown in Figure 3.5.f. The part consists of a slotted piece and a cap

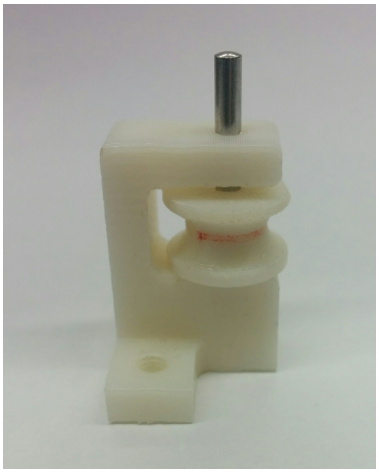

(a) Pulley 1.

(b) Flexion–extension motor pulley.

(c) Cable raiser.

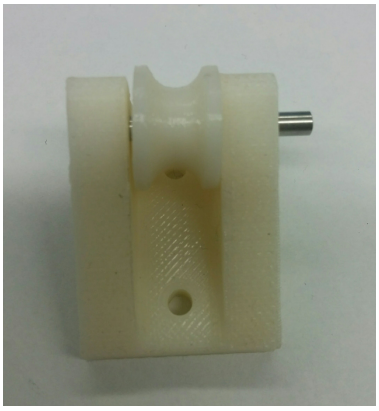

(d) Pulley 2.

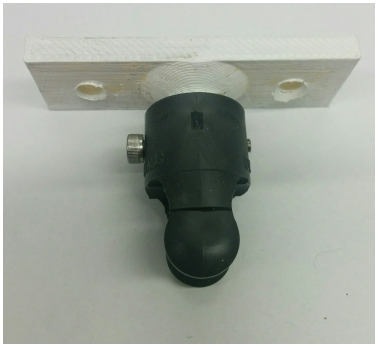

(e) U-joint connector.

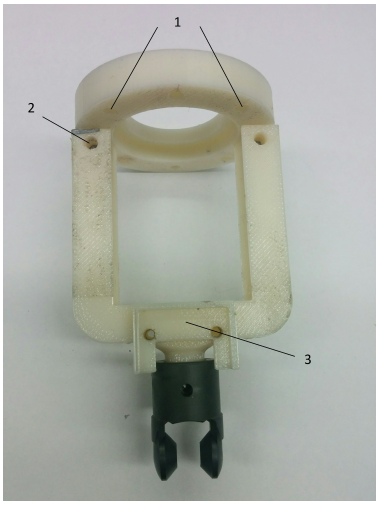

(f) Hand.

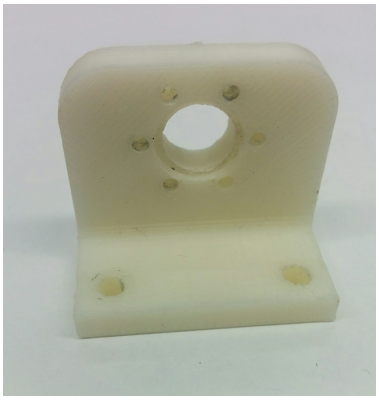

(g) Flexion–extension motor holder.

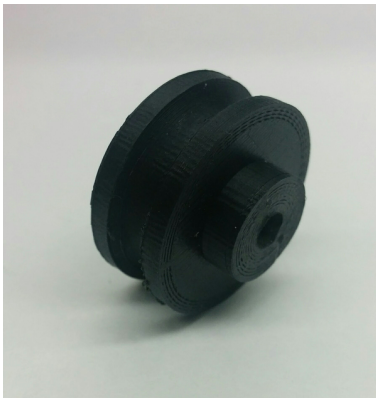

(h) Ulnar–radial deviation motor pulley.

(i) Ulnar–radial deviation motor holder.

Figure 3.5: Parts used in the DC motor setup.

that can be attached onto the slotted piece. The slot is used to hold a 500 g mass and the cap holds it in place. One half of the u-joint is attached on the end of the hand and will connect to the other half of the u-joint. This part was designed to have the same torque due to gravity at the wrist as a hand with the 95^{th} percentile mass and center of mass of the hand. There is a slot near the base of the hand to attach an inertial measurement unit (IMU) sensor.

7. *Flexion–Extension Motor Holder*: This part is shown in Figure 3.5.g. The part is used to fix the flexion–extension motor to the arm.

8. *Ulnar–Radial Deviation Motor Pulley*: This part is shown in Figure 3.5.h. The pulley attaches to the shaft of the motor for ulnar–radial deviation. There is a hole in the pulley to attach the cable to the pulley.

9. *Ulnar–Radial Deviation Motor Holder*: This part is shown in Figure 3.5.i. This part is used to fix the ulnar–radial deviation motor to the arm.

The actuators that were used are two 12 watt EC-max 22 brushless DC motors from Maxon Motors (see Appendix B.1 for the specification sheet), which are powered by a 24 V DC power supply and are controlled using an EPOS 24/5 motor controller connected to each motor. The EPOS controllers communicate with the PC using RS-232 communication.

3.3 Kinematics and Dynamics

To make the controller for the device, the kinematics and dynamics needed to be determined first. Although the device will only be actuating the wrist joints, it was necessary to include the forearm pronation–supination and elbow flexion–extension joints because they will affect the dynamics of the wrist. The kinematics were created using the Denavit–Hartenberg (DH) method [67].

Figure 3.6 shows the joint configuration of the arm in the zero position made following the DH method. The DH parameters that were found are shown in Table 3.4 where d is the length of the forearm, c_m is the distance from the wrist to the center of mass of the hand, and q_i is the angle of joint i for each of the four joints. The DH parameters are then used to make the transformation

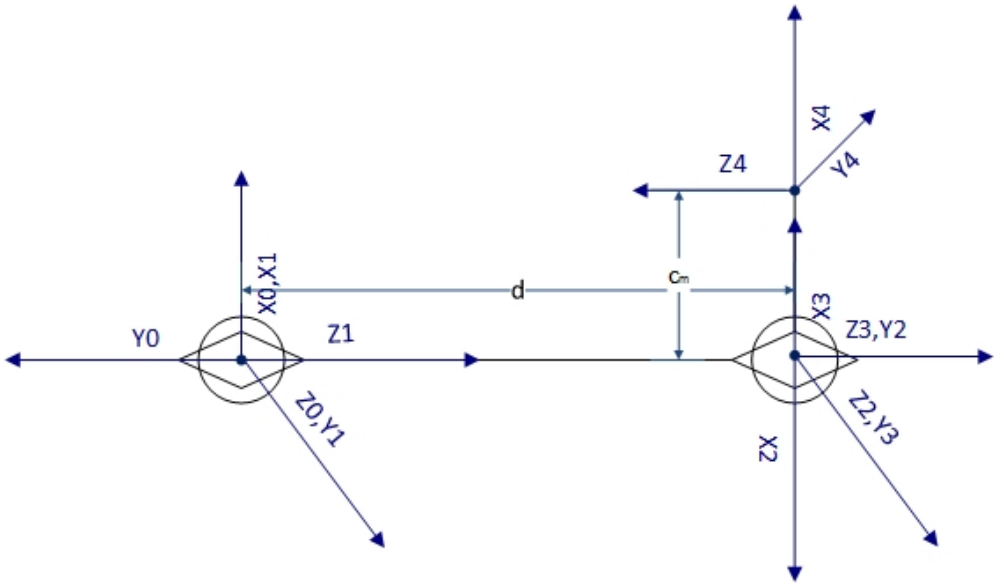

Figure 3.6: Joint configuration of the arm. The circles represent the elbow FE joint and wrist FE joint rotating about axis Z0 and Z2. The diamonds represent the forearm PS joint and wrist UR deviation joint rotating about axis Z1 and Z3. The elbow FE joint and forearm PS joint share the same origin, and the wrist FE joint and UR deviation joint share the same position.

matrices between each joint, which are then multiplied together to get the final transformation matrix T_{04}:

Joint	a	d	α	θ
1	0	0	$\frac{\pi}{2}$	q_1
2	0	d	$-\frac{\pi}{2}$	q_2
3	0	0	$\frac{\pi}{2}$	q_3
4	c_m	0	0	q_4

Table 3.4: Denavit–Hartenberg parameters.

$$R_{04} = \begin{bmatrix} c_4(s_1s_3 + c_1c_2c_3) + c_1s_2s_4 & c_1s_2c_4 - s_4(s_1s_3 + c_1c_2c_3) & c_1c_2s_3 - s_1c_3 \\ s_1s_2s_4 - c_4(c_1s_3 - s_1c_2c_3) & s_4(c_1s_3 - s_1c_2c_3) + s_1s_2c_4 & c_1c_3 + s_1c_2s_3 \\ s_2c_3c_4 - c_2s_4 & -c_2c_4 - s_2c_3s_4 & s_2s_3 \end{bmatrix} \tag{3.2}$$

$$P_{04} = \begin{bmatrix} ds_1 + c_m c_4(s_1 s_3 + c_1 c_2 c_3) + c_m c_1 s_2 s_4 \\ c_m s_1 s_2 s_4 - c_m c_4(c_1 s_3 - s_1 c_2 c_3) - d c_1 \\ c_m s_2 c_3 c_4 - c_m c_2 s_4 \end{bmatrix} \tag{3.3}$$

$$T_{04} = \begin{bmatrix} & R_{04} & & P_{04} \\ \begin{bmatrix} 0 & 0 & 0 \end{bmatrix} & & & 1 \end{bmatrix} \tag{3.4}$$

where $c_i = \cos q_i$, and $s_i = \sin q_i$.

The inverse kinematics are solved by first finding the solution for Joint 1. Joint 1 can be solved by getting the position of the wrist center P_c:

$$H = T(1:3, 1) \tag{3.5}$$

$$P_c = P_{04} - c_m \cdot H \tag{3.6}$$

$$q_1 = atan2(P_c(1), -P_c(2))^1 \tag{3.7}$$

where H is a vector in the direction from the wrist to the center of the hand. The solutions to the remaining three joints can be solved by treating it as a spherical wrist:

$$R_{14} = R_{01}^T \cdot R_{04} \tag{3.8}$$

$$n = R_{14}(1:3,1); s = R_{14}(1:3,2); a = R_{14}(1:3,3) \tag{3.9}$$

There are two cases for solving for the three remaining joints depending on whether q_3 is between 0 and π or 0 and $-\pi$, but because the application only requires for the range of q_3 to be between 0 and π, the other scenario will not be included. When $0 < q_3 < \pi$,

$$q_2 = atan2(a(2), a(1)) \tag{3.10}$$

$$q_3 = atan2(\sqrt{a(1)^2 + a(2)^2}, -a(3)) \tag{3.11}$$

[1] atan2 is the arctangent that considers the signs of its inputs.

$$q_4 = atan2(-s(3), n(3)) \tag{3.12}$$

It should be noted that there is an internal singularity when $q_3 = 0$ or $q_3 = \pi$. This is due to the axis of motion of Joint 2 and Joint 4 being aligned. This is within the range of human wrist motion and should be considered in future applications, but it is outside of the range of testing that was performed in this chapter.

The dynamics for the arm were found using an energy-based approach through the implementation of the Euler-Lagrange equations of motion [68], as follows:

$$D(q)\ddot{q} + C(q, \dot{q})\dot{q} + G(q) = \tau \tag{3.13}$$

where *D(q)* is the inertia matrix, $C(q, \dot{q})$ combines the Coriolis and centrifugal terms, *G(q)* is the gravitational term, and τ is the torque. The inertia matrix is described by the equation:

$$D(q) = \sum_{i=1}^{4} m_i J_{v_i}(q)^T J_{v_i}(q) + J_{\omega_i}(q)^T R_{0i}(q) I_i R_{0i}(q)^T J_{\omega_i}(q) \tag{3.14}$$

where m_i is the mass of link i, I_i is the inertia for link i with reference to the center of mass, and $J_{\omega_i}(q)$ and $J_{v_i}(q)$ is from the manipulator Jacobian:

$$J = \begin{bmatrix} J_v \\ \\ J_\omega \end{bmatrix}. \tag{3.15}$$

The Coriolis and centrifugal matrix are described by:

$$C_{kj}(q, \dot{q}) = \sum_{i=1}^{4} c_{ijk}(q)\dot{q}_i \tag{3.16}$$

where the elements of the matrix is described by:

$$c_{ijk}(q) \equiv \frac{1}{2}\left(\frac{\partial D_{kj}}{\partial q_i} + \frac{\partial D_{ki}}{\partial q_j} - \frac{\partial D_{ij}}{\partial q_k}\right). \tag{3.17}$$

The gravitational term in Equation 3.13 is described by the following equation:

$$G(k) = \frac{\partial U_g}{\partial q_k} \tag{3.18}$$

where the U_g is the gravitational potential energy of the manipulator. U_g can be described by the following equation:

$$U_g = \sum_{i=1}^{4} m_i g r_i \tag{3.19}$$

where m_i is the mass of link i, g is the gravity of Earth, and r_i is the vertical distance to the center of mass of link i. The calculations to solve for the terms in Equation 3.13 were performed in MATLAB. The code used to equations calculate those terms is shown in Appendix A.1.

3.4 Controller

The purpose of the setup is to test the motion control of the hand. The control system was developed in Simulink, shown in Figure 3.7, which consists of an inverse dynamics controller, a sensor reading block, motor output blocks, friction models, and a wrist torque to motor torque block. The Simulink model uses the Simulink Desktop Real-Time add-on to make the model run in real-time.

Since the setup has a motor pulling on a cable that is attached at the hand, the torque applied by the motor will not be the same as the torque at the wrist. The relationship between the wrist and motor torque was modeled using a geometric solution. In Figure 3.8 Point A refers to the spot where the cable is held above the arm, and Point v refers to where the two side cables are attached to the hand. The relationships between the various points and distance, as described in Figure 3.8 are as follows:

$$A_x = -x_0, A_y = d_1 \tag{3.20}$$

$$v_x = x_1 \cos\theta - d_3 \sin\theta, v_y = x_1 \sin\theta + d_3 \cos\theta \tag{3.21}$$

$$\Delta x = v_x - A_x, \Delta y = v_y - A_y \tag{3.22}$$

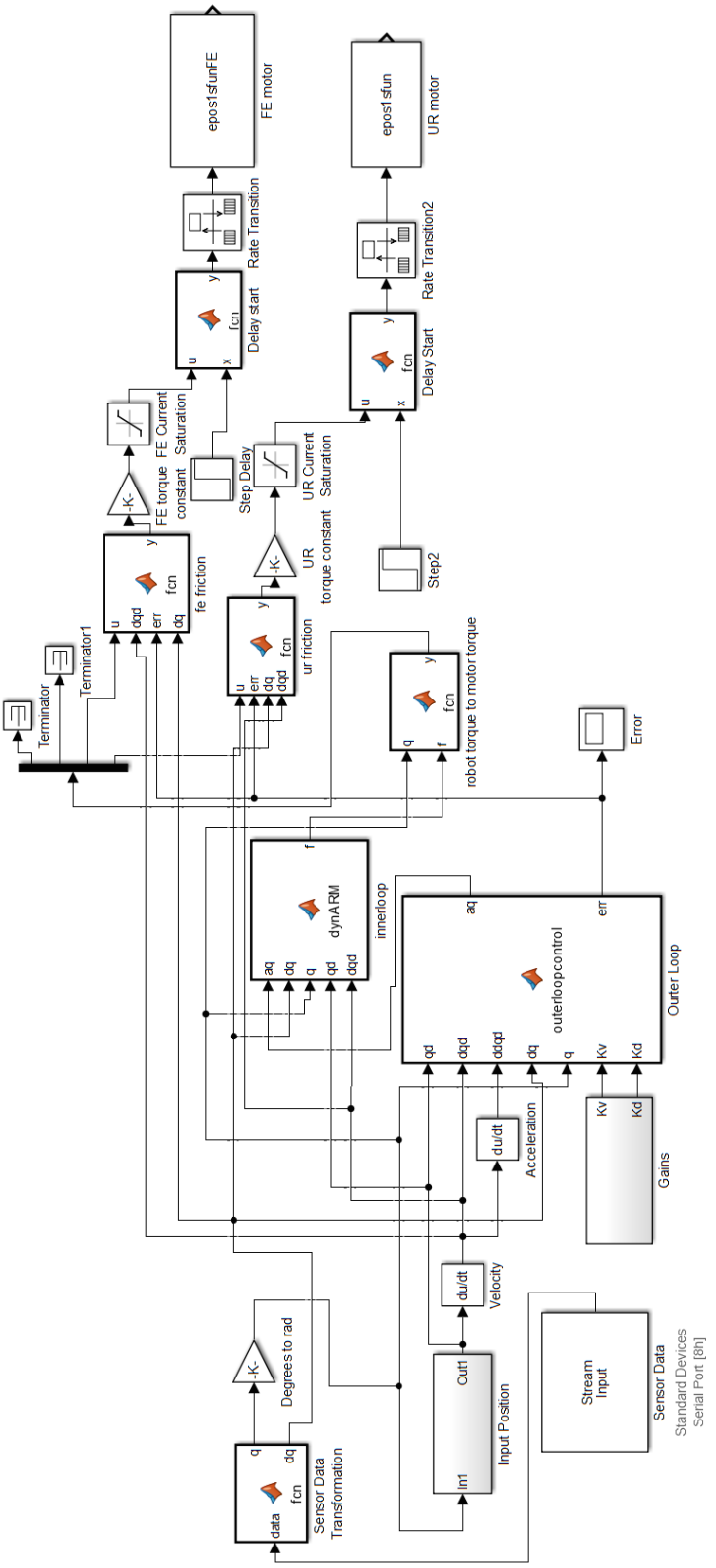

Figure 3.7: Inverse dynamics controller.

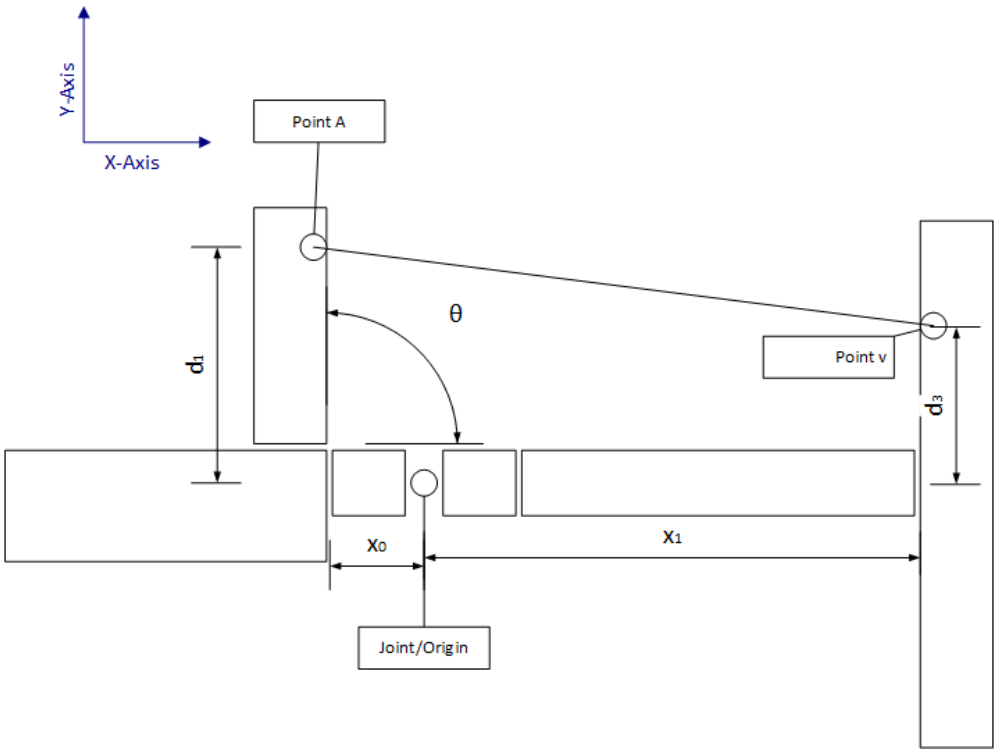

Figure 3.8: Joint torque to motor torque model.

$$\gamma = atan2(\Delta y, \Delta x) \tag{3.23}$$

$$f_x = \cos\theta - \gamma, f_y = \sin\theta - \gamma \tag{3.24}$$

$$\tau_{motor} = -\frac{P\tau_w}{f_x d_3 + f_y x_1} \tag{3.25}$$

where P is the radius of the pulley that is attached to the motor, τ_{motor} is the torque from the motor, τ_w is the torque required at the wrist, v_x and v_y are the x and y distances of point v from the origin, A_x and A_y are the x and y positions of point A from the origin, and γ is the angle of the vector from point v to point A.

The cables moving over the pulleys will be experiencing friction, therefore it should be considered in the controller. The frictional force in the device is modeled using the Stribeck curve, as follows:

$$f = f_c + (f_s + f_c)e^{-v/v_s} \tag{3.26}$$

where f_c is the Coulomb friction, f_s is the static friction, v_s is the Stribeck velocity threshold,

and v is the velocity of the cable. The Coulomb friction, static friction, and the Stribeck velocity threshold were determined experimentally.

3.5 Sensing System

The setup uses two Sparkfun 9 DOF inertial measurement units (IMU), which have a 3 DOF gyroscope, 3 DOF accelerometer, and 3 DOF magnetometer. The datasheet is available in Section B.2. The locations of the two sensors are at the back of the arm and on top of the hand close to the wrist joint as shown in Figures 3.9 and 3.10, respectively, and they are connected to an Arduino Uno microcontroller. The purpose of these sensors is to measure the angular positions and velocities of the 4 joints: elbow flexion–extension, forearm pronation–supination, wrist flexion–extension, and wrist ulnar–radial deviation.

The angles for Joints 1 and 2 do not require the magnetometer so a complementary filter was used to obtain those joints from the IMU on the arm. The complementary filter requires the angle to be calculated from the gyroscope and the accelerometer, which are then weighted individually and added together as shown by:

$$\theta_n = 0.95\theta_{gyro} + 0.05\theta_{accel} \tag{3.27}$$

where θ_{gyro} is the angle calculated from the gyroscope, and θ_{accel} is the angle calculated from the accelerometer. The gyroscope angles were calculated using the following equation:

$$\theta_{gyro} = \theta_{n-1} + \dot{\theta}_{gyro}\Delta t \tag{3.28}$$

where θ_{n-1} is the previous angle, Δt is the time between readings, and $\dot{\theta}_{gyro}$ is the angular velocity from the gyroscope. The accelerometer angles of Joints 1 (pitch) and 2 (roll) were calculated using the following equations:

$$q_1 = atan2(-a_x, \sqrt{a_y a_y + a_z a_z}) \tag{3.29}$$

$$q_2 = atan2(ay, az) \tag{3.30}$$

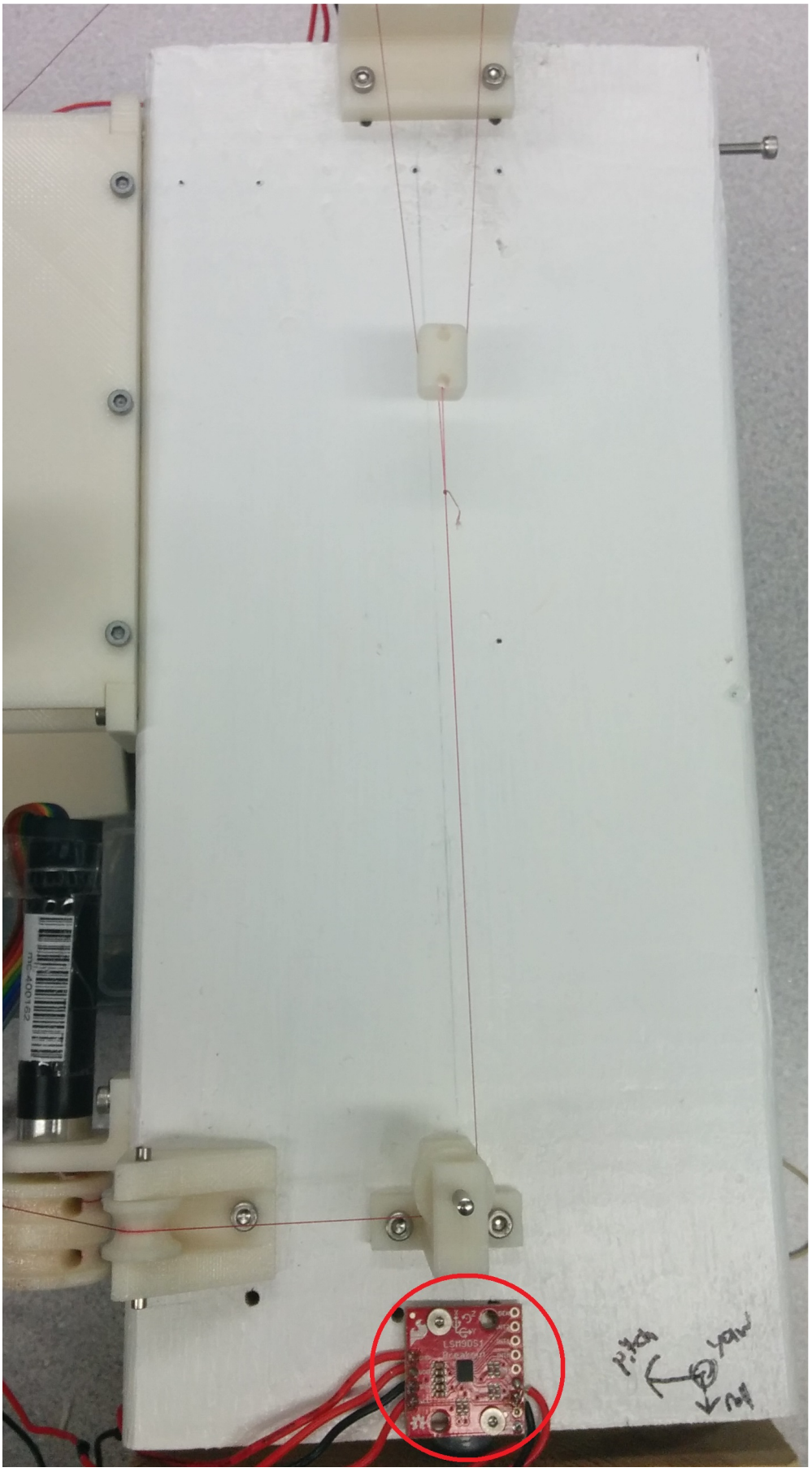

Figure 3.9: Location of IMU on the arm.

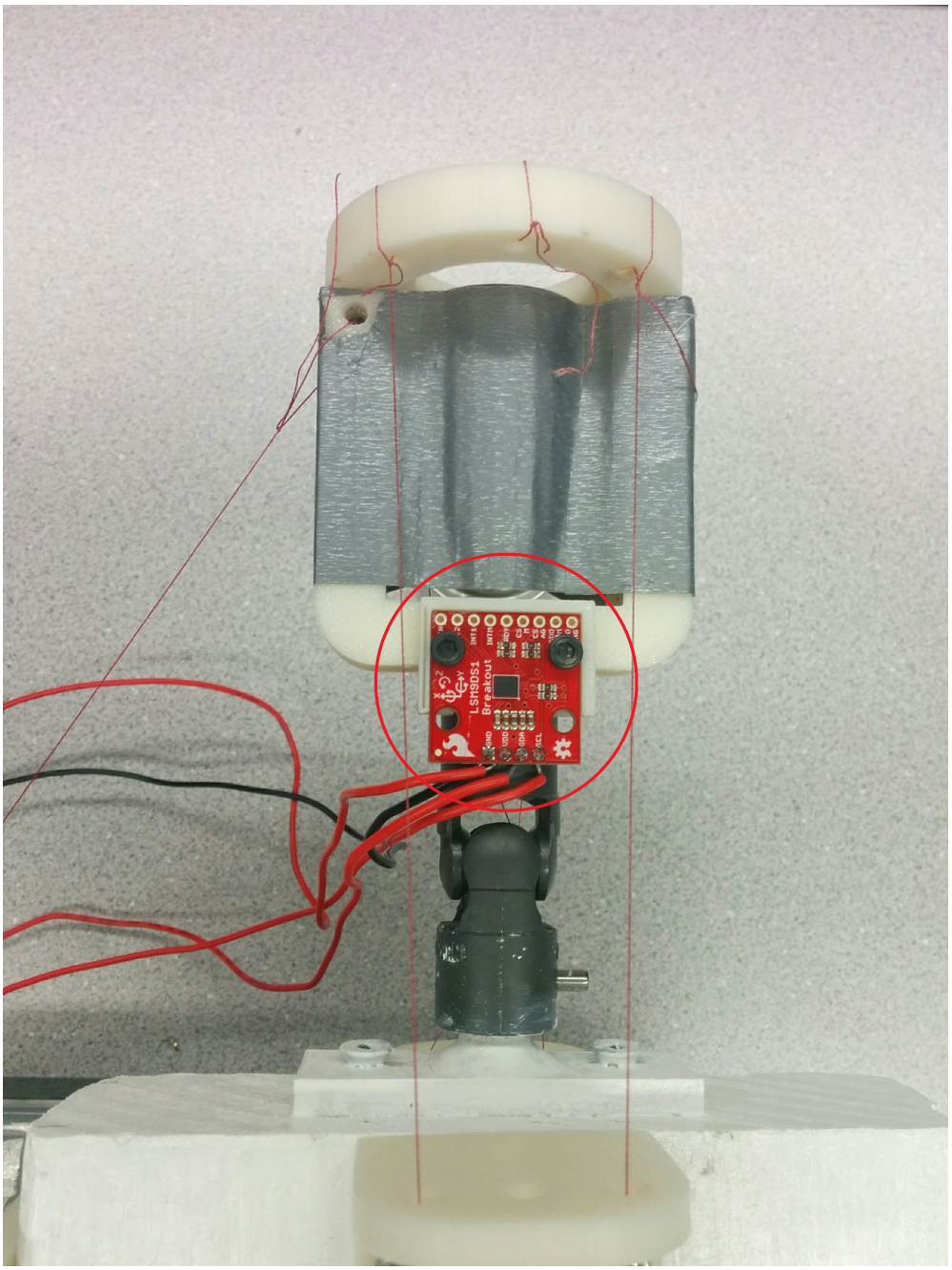

Figure 3.10: Location of IMU on the hand.

where a_x, a_y, and a_z are the acceleration forces from the accelerometer. The weights for the complimentary filter were arbitrarily chosen.

The angles of the flexion–extension and ulnar–radial deviation of the joints were obtained using a Madgwick filter [69, 70]. The Madgwick filter uses the gyroscope, accelerometer, and magnetometer readings to calculate the orientation in a fixed frame relative to the Earth. Kalman filters are often used to get the orientation from an IMU but they tend to be computationally heavy, which can be a problem for wearable devices. A Madgwick filter was selected to get the orientation of the hand. The Madgwick filter fuses together the orientation calculated from the gyroscope and the orientation calculated from the accelerometer and magnetometer. The orientation from the gyroscope is used to filter out the high frequency errors from the accelerometer and magnetometer orientation, and the accelerometer and magnetometer orientation is able to filter out the drift from the gyroscope orientation. The Madgwick filter is able to operate with a static RMS error of less than 0.8° and dynamic RMS error of less than 1.7°, which are similar to those obtained with the Kalman filter. The advantage that the Madgwick filter has over the Kalman filter is that it has a low computational load and is able to operate at a lower sampling frequency [69, 70].

The orientation from the Madgwick filter then needs to be transformed to be in the same frame as the robot. The transformation was completed using the following equations:

$$p = R_1^0 \cdot R_2^1 \cdot \hat{p} \tag{3.31}$$

$$R_1^0 = \begin{bmatrix} 1 & 0 & 0 \\ 0 & \cos\theta_2 & -\sin\theta_2 \\ 0 & \sin\theta_2 & \cos\theta_2 \end{bmatrix} \qquad R_2^1 = \begin{bmatrix} \cos\theta_1 & 0 & \sin\theta_1 \\ 0 & 1 & 0 \\ -\sin\theta_1 & 0 & \cos\theta_1 \end{bmatrix} \qquad \hat{p} = \begin{bmatrix} \hat{\theta_2} \\ \hat{\theta_3} \\ \hat{\theta_4} \end{bmatrix} \tag{3.32}$$

where $\hat{\theta}_2$, $\hat{\theta}_3$, and $\hat{\theta}_4$ are the roll, pitch, and yaw readings from the Madgwick filter respectively, and p is a vector containing the transformed orientation.

The IMU sensors communicate with an Arduino Uno microcontroller. The IMU on the arm communicates with the Arduino using the I2C communication protocol, and the IMU on the hand communicates with the Arduino using the SPI communication protocol. The IMUs are sampled at a frequency of 60 Hz and the data are filtered on the Arduino. The Arduino sends the filtered

data to the desktop computer through serial communication with a baud rate of 115200 baud.

3.6 Experimental Evaluation

A series of experiments were performed to determine the accuracy of the IMU sensing and of the dynamics equations of motion. The results of these experiments are presented in the following sections.

3.6.1 Accuracy of the IMU With a Madgwick Filter

The objective of this first experiment was to determine the accuracy of the IMU with the Madgwick filter and to calibrate the yaw reading of the IMU.

3.6.1.1 Methods

To determine the accuracy of the IMU with the Madgwick filter, the Aurora electromagnetic tracking system (Northern Digital Inc., Waterloo, ON) was used to compare readings with the IMU. Figure 3.11 shows the placement of the two 5-DOF sensors. Sensor A measures the pitch and yaw of the hand relative to Earth, and Sensor B measures the roll of the arm relative to Earth. The 5-DOF Aurora sensors have an accuracy of 0.2°. The pitch and yaw of the hand were recorded at 12 different positions using both the IMU and the Aurora while the arm was at rest in the pronation–supination axis. The arm was then rotated approximately 30 degrees in the pronation–supination direction and the pitch and yaw of the hand were recorded at another 9 positions. The arm was then rotated to 90 degrees and another 9 position of the pitch and the yaw of the hand were recorded. A total of 30 positions were recorded in each round. The same procedure was followed another 2 times for a total of 3 rounds of recordings and a total of 90 positions. The first set of data was used to calibrate the yaw readings from the IMU. The three rounds of collection were then repeated after calibrating the yaw of the IMU. This second set of data was used to determine the accuracy of the pitch and yaw of the IMU at the hand. Finally, eight positions of the forearm rotation were recorded from the IMU and the Aurora. This was also repeated three times. These data were then used to determine the accuracy of pronation–

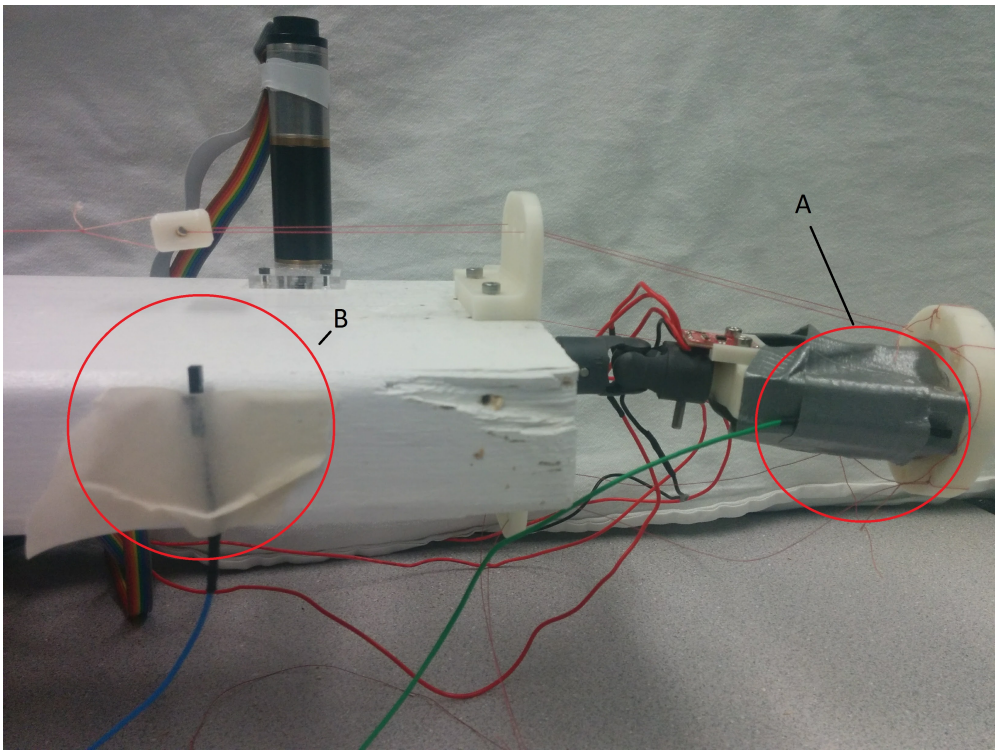

Figure 3.11: Placement of Aurora sensors. The Sensor at point A measures the pitch and yaw of the hand. The sensor at point B measures the roll of the forearm.

supination readings from the IMU on the forearm.

3.6.1.2 Results

This data from the IMU and the Aurora attached to the hand at 90 positions of the hand were plotted against each other as shown in Figure 3.12. Equation 3.33 represents the quadratic curve of best fit of the data from Figure 3.12, which was used to calibrate the IMU for yaw readings.

$$y = 0.0037x^2 - 2.4477x + 406.73 \tag{3.33}$$

After calibrating the yaw, the second set of data was used to assess the tracking accuracy. For this experiment, the readings from the Aurora were assumed to be the true position. The RMS difference between the IMU and the Aurora readings for the yaw and pitch of the hand is shown in Table 3.5, and the RMS difference between the IMU and the Aurora readings for the pronation–supination is shown in Table 3.6.

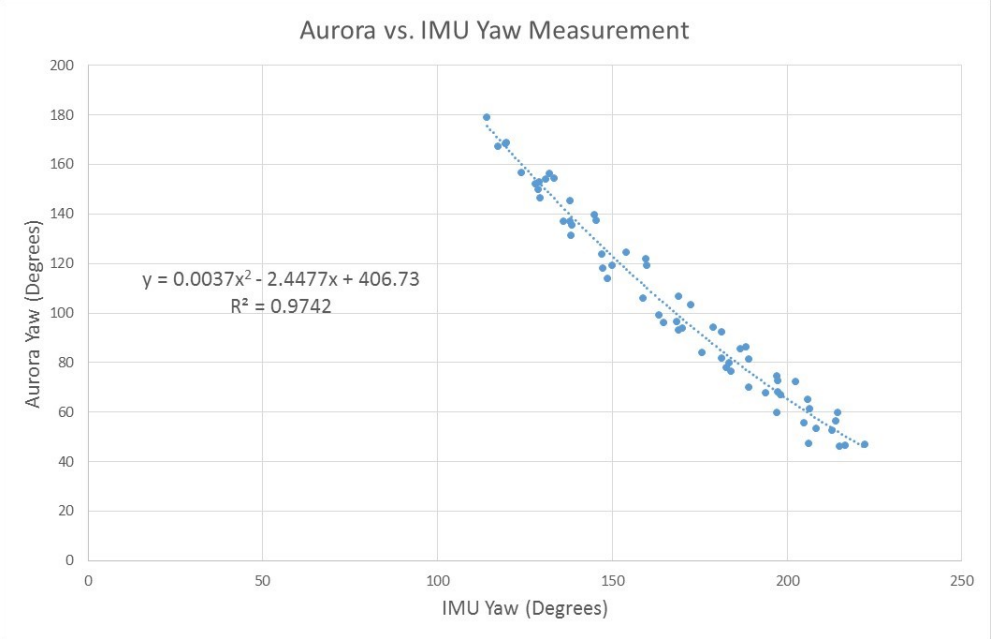

Figure 3.12: IMU calibration using the Aurora.

3.6.2 Evaluation of the Motor Setup with an Inverse Dynamics Controller

Once the IMU tracking error had been quantified, a second experiment was performed to assess the performance of the motor setup using an inverse dynamics controller. Gathering data on the performance of the motor setup means there will be a quantitative way to compare the performance of the DEA setup with the motor setup.

3.6.2.1 Methods

To examine the performance of the motor setup with an inverse dynamics controller, 3 trials for 6 different actions were performed with a the two different weighted hands in Table 3.3. The smaller weighted hand was tested to first see that the controller could control the system as required. The torque due to gravitational forces is less than the 5^{th} percentile in Table 3.2. The larger weighted hand is represents the same torque due to gravity as the 95^{th} percentile hand in Table 3.2. The actions were: flexion–extension by itself, ulnar–radial deviation by itself, flexion–extension with manual forearm pronation–supination movement, ulnar–radial deviation with manual forearm pronation–supination movement, flexion–extension and ulnar–radial deviation together, and flexion–extension with ulnar–radial deviation during manual forearm pronation–supination. The

Round	PS Rotation	Pitch RMS Error (degrees)	Yaw RMS Error (degrees)	Total RMS Pitch Error (degrees)	Total RMS Yaw Error (degrees)
1	0	1.77	5.18	2.40	5.22
	30	2.47	3.88		
	90	2.93	6.61		
2	0	1.63	2.76	2.31	2.84
	30	2.03	2.93		
	90	3.24	2.84		
3	0	2.13	4.37	2.19	3.91
	30	2.23	3.39		
	90	2.20	3.97		
			Total Average RMS Error (degrees)	2.30	3.99
			Error As a % of Max Range	4.9	8.9

FE: Flexion–Extension, UR: Ulnar–Radial Deviation, PS: Pronation–Supination

Table 3.5: RMS error between IMU and Aurora reading for pitch and yaw. The maximum error as a percentage of the maximum range is based on the maximum range used in Section 3.6.2.

Round	PS RMS Error (degrees)	Error As a % of Maximum Range
1	2.93	4.9
2	3.17	5.3
3	2.61	4.3
All Rounds	2.90	4.8

Table 3.6: RMS error between IMU and Aurora readings for forearm roll. The maximum error as a percentage of the maximum range is based on the maximum range used in Section 3.6.2.

three individual motions performed in the experiment are shown in Figure 3.13. When the flexion–extension motor was running, it was following the input signal described by Equation 3.34. When the ulnar–radial deviation motor was running, it was following the input signal in Equation 3.35.

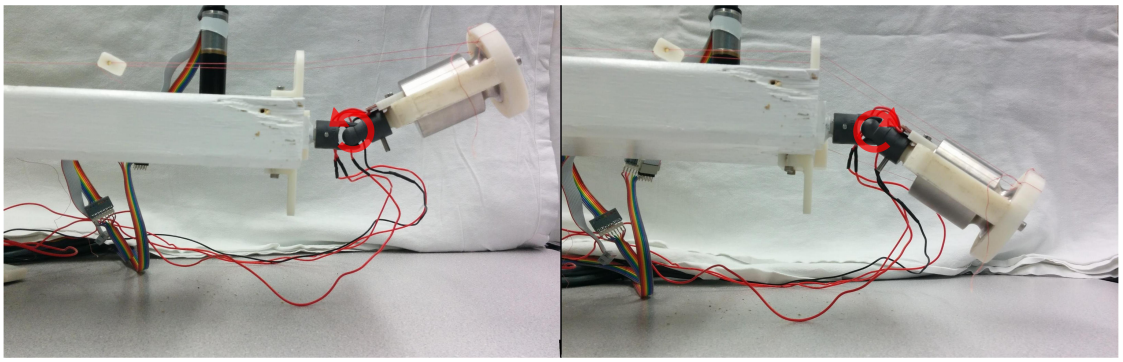

(a) Flexion–Extension.

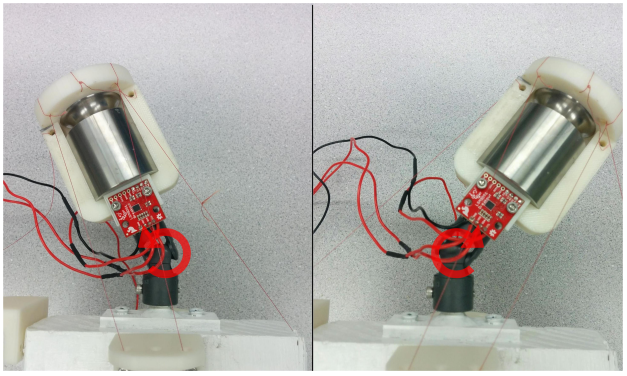

(b) Ulnar–Radial Deviation.

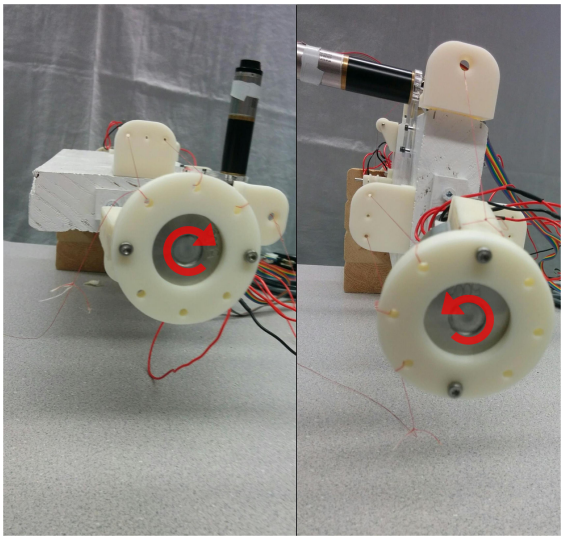

(c) Pronation–Supination.

Figure 3.13: Motor setup showing the various motions: FE, UR, and PS.

For joints that are not active, they were commanded the current position of that same joint.

$$u_3 = \frac{\pi}{8} \sin\left(\frac{\pi}{8} t\right) + \frac{\pi}{2} \tag{3.34}$$

$$u_4 = \frac{\pi}{8} \sin\left(\frac{\pi}{8} t\right) \tag{3.35}$$

The frequency of the input signal was chosen based on how fast the joints could move without the system becoming unstable. Higher frequencies caused the joints to sometimes move past the range of the u-joint, causing the system to become unstable. Smaller frequencies caused the system to perform similarly to this frequency.

3.6.2.2 Results

The orientation of the joints from the IMU was recorded during each of the actions and was then compared to the input signal to determine the error. Using the error gathered throughout the duration of the movement, the root mean square (RMS) error was calculated and the max error was found as shown in Tables 3.7 and 3.8. The results obtained during each of the motions are presented below.

Flexion–Extension

The flexion–extension action corresponds to the motion shown in Figure 3.13(a). The joint was able to follow the input position smoothly when using the 200 g weight and the 500 g weight as shown in Figures 3.14 and 3.15. Tables 3.7 and 3.8 show the root mean square of the errors for the 200 g weight and the 500 g weight, respectively. The average errors as a percentage of the maximum range for the motion is 3.91% when using the 200 g weight and 2.80% when using the 500 g weight.

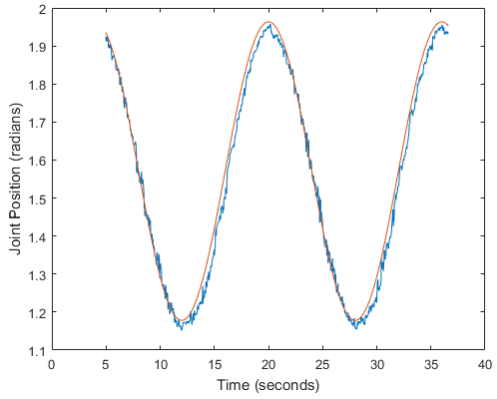

(a) Flexion–extension motion with 200g.

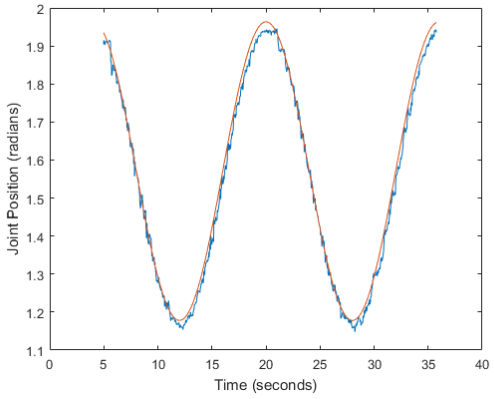

(b) Flexion–extension motion with 500g.

Figure 3.14: Results of the FE motion: comparison between input motion (*orange*) and output motion (*blue*).

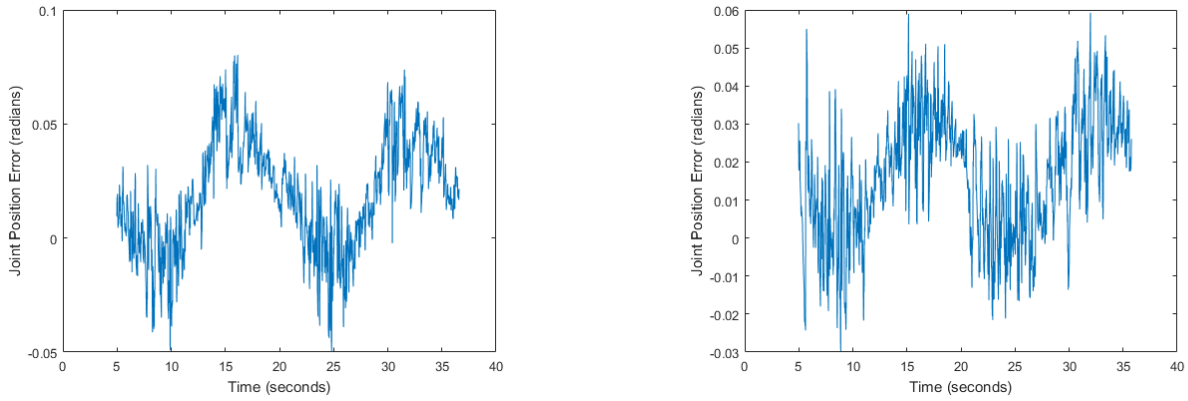

(a) Flexion–extension error with 200g.

(b) Flexion–extension error with 500g.

Figure 3.15: Results of the FE motion: error of the output motion.

Ulnar–Radial Deviation

The ulnar–radial deviation action is the motion shown in Figure 3.13(b). The joint was able to follow the input position smoothly when using the 200 g weight and the 500 g weight as shown in Figures 3.16 and 3.17. Tables 3.7 and 3.8 show the root mean square of the errors for the 200 g weight and the 500 g weight respectively. The average errors as a percentage of the maximum range for the motion is 1.84% when using the 200 g weight and 3.44% when using the 500 g weight.

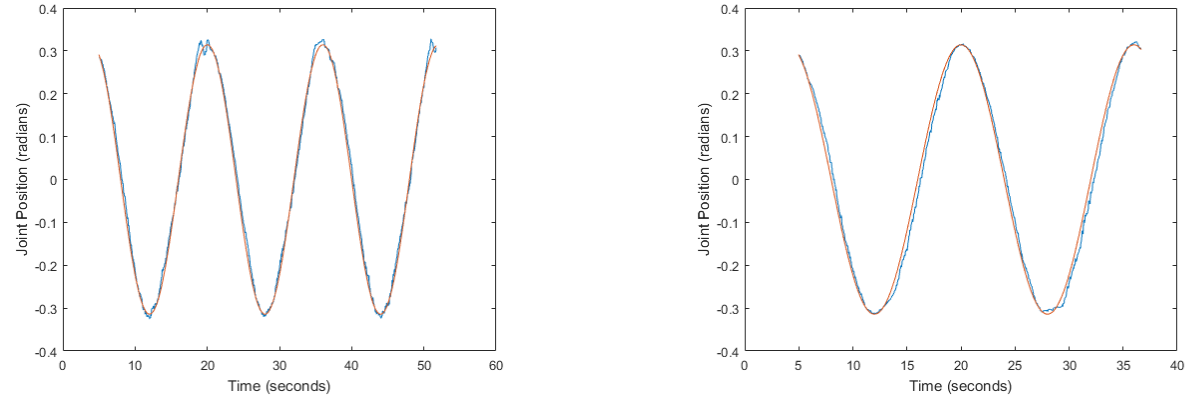

(a) Ulnar–radial deviation motion with 200g.

(b) Ulnar–radial deviation motion with 500g.

Figure 3.16: Results of the UR motion: comparison between input motion (*orange*) and output motion (*blue*).

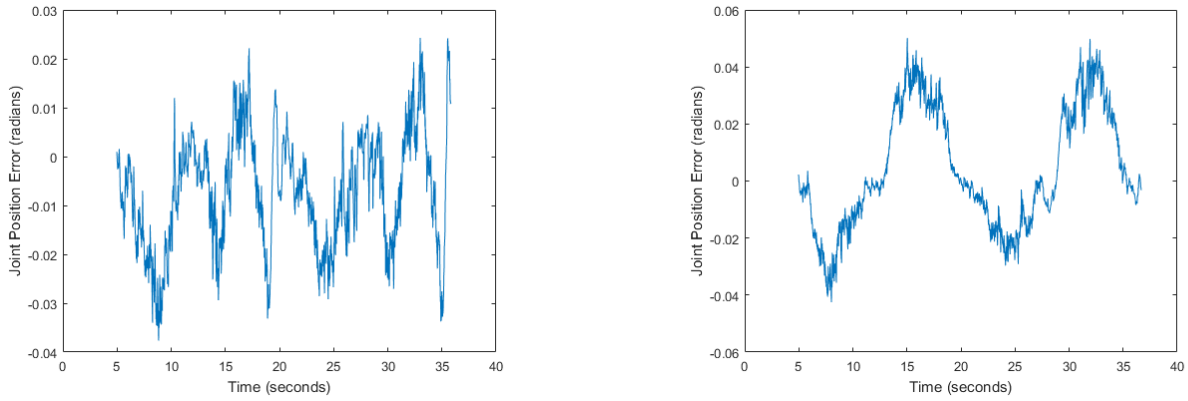

(a) Ulnar–radial deviation error with 200g.

(b) Ulnar–radial deviation error with 500g.

Figure 3.17: Results of the UR motion: error of the output motion.

Flexion–Extension During Pronation–Supination

The flexion–extension during pronation–supination action combines the 2 motions shown in Figures 3.13(a) and 3.13(c). The joint was able to follow the input position smoothly when using the 200 g weight and the 500 g weight as shown in Figures 3.18 and 3.19. Tables 3.7 and 3.8 show the root mean square of the errors for the 200 g weight and the 500 g weight respectively. The average errors as a percentage of the maximum range for the motion is 3.67% when using the 200 g weight and 2.96% when using the 500 g weight.

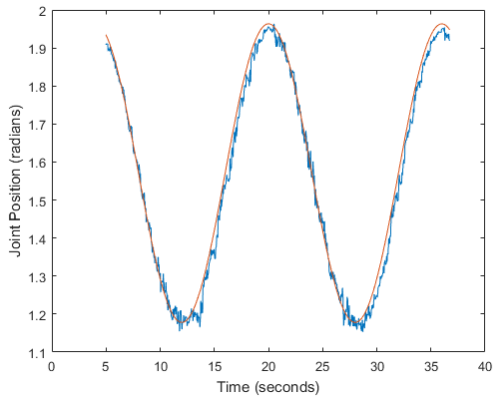

(a) Flexion–extension motion during flexion–extension, and pronation–supination with 200 g weight.

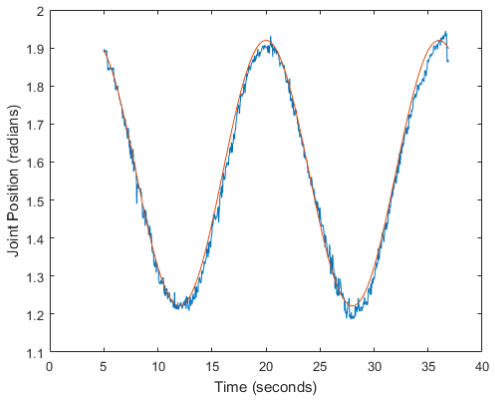

(b) Flexion–extension motion during flexion–extension, and pronation–supination with 500 g weight.

Figure 3.18: Results of the FE motion during FE+PS: comparison between input motion (*orange*) and output motion (*blue*).

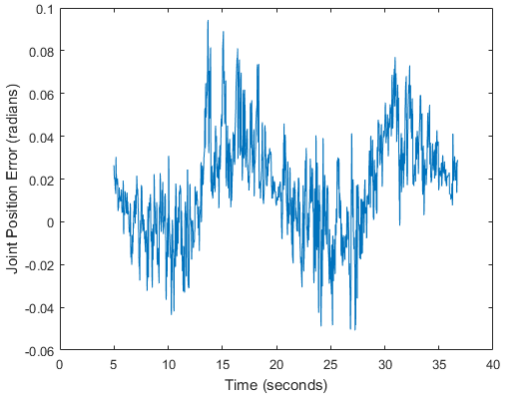

(a) Flexion–extension error during flexion–extension, and pronation–supination with 200 g weight.

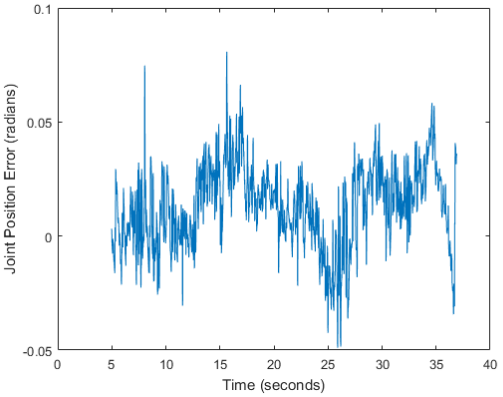

(b) Flexion–extension error during flexion–extension, and pronation–supination with 500 g weight.

Figure 3.19: Results of the FE motion during FE+PS: error of the output motion.

Ulnar–Radial Deviation During Pronation–Supination

The ulnar–radial deviation during pronation–supination action combines the 2 motions shown in Figures 3.13(a) and 3.13(b). The joint was able to follow the input position smoothly when using the 200 g weight and the 500 g weight as shown in Figures 3.20 and 3.21. Tables 3.7 and 3.8 show the root mean square of the errors for the 200 g weight and the 500 g weight respectively.

The average errors as a percentage of the maximum range for the motion is 2.89% when using the 200 g weight and 4.69% when using the 500 g weight.

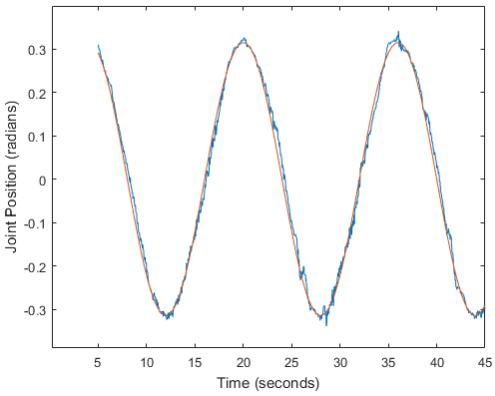

(a) Ulnar–radial deviation motion during ulnar–radial deviation, and pronation–supination with 200 g weight.

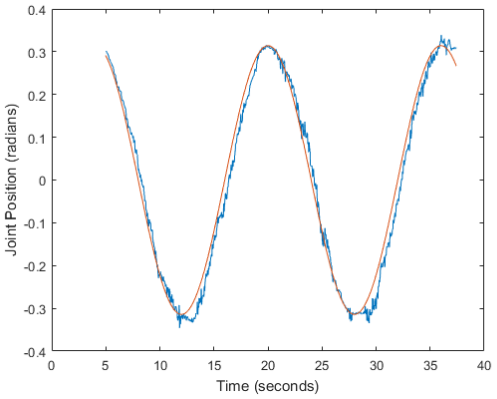

(b) Ulnar–radial deviation motion during ulnar–radial deviation, and pronation–supination with 500 g weight.

Figure 3.20: Results of the UR motion during UR+PS: comparison between input motion (*orange*) and output motion (*blue*).

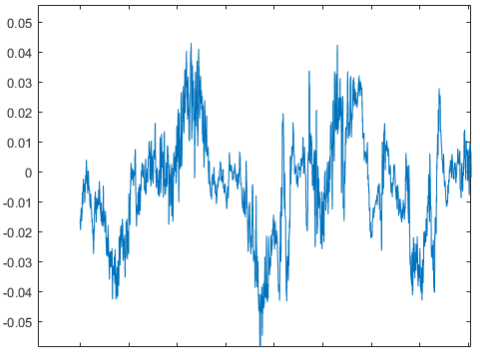

(a) Ulnar–radial deviation error during ulnar–radial deviation, and pronation–supination with 200 g weight.

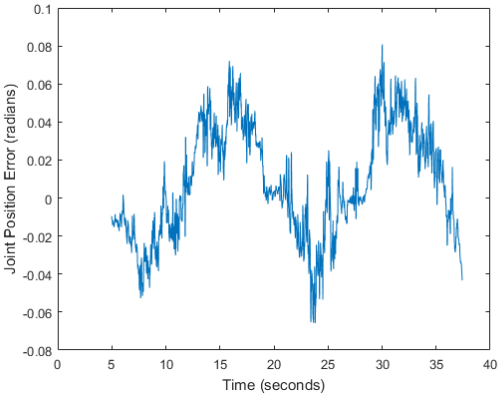

(b) Ulnar–radial deviation error during ulnar–radial deviation, and pronation–supination with 500 g weight.

Figure 3.21: Results of the UR motion during UR+PS: error of the output motion.

Flexion–Extension and Ulnar–Radial Deviation

The flexion–extension and ulnar–radial deviation action combines the 2 motions shown in Figures 3.13(a) and 3.13(b). The joints were able to follow the input positions smoothly when

using the 200 g weight and the 500 g weight as shown in Figures 3.22, 3.23, 3.24, and 3.25. Tables 3.7 and 3.8 show the root mean square of the errors for the 200 g weight and the 500 g weight respectively. The average errors as a percentage of the maximum range for the flexion–extension is 3.69% when using the 200 g weight and 3.83% when using the 500 g weight. The average errors as a percentage of the maximum range for ulnar–radial deviation is 3.53% when using the 200 g weight and 3.53% when using the 500 g weight.

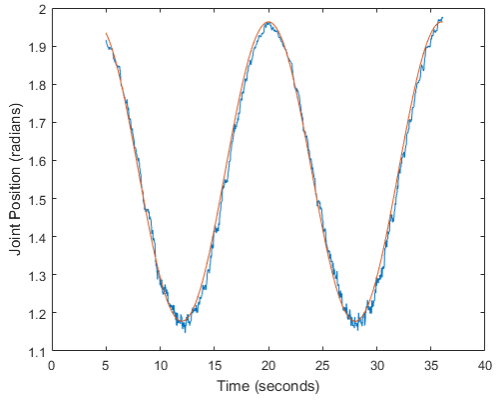

(a) Flexion–extension motion during flexion–extension, and ulnar–radial deviation with 200 g weight.

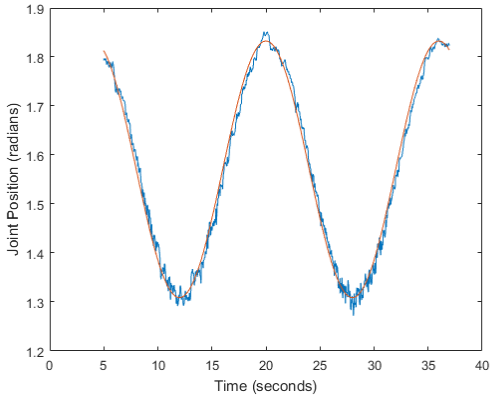

(b) Flexion–extension motion during flexion–extension, and ulnar–radial deviation with 500 g weight.

Figure 3.22: Results of the FE motion during FE+UR: comparison between input motion (*orange*) and output motion (*blue*).

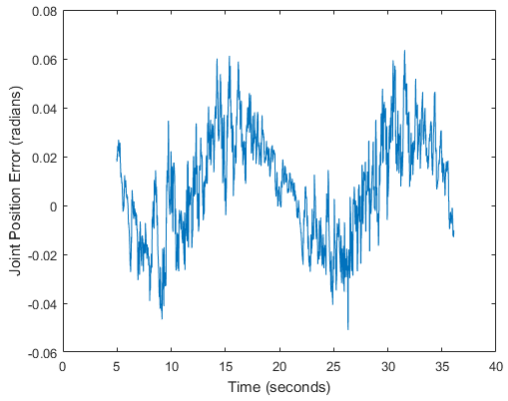

(a) Flexion–extension error during flexion–extension, and ulnar–radial deviation with 200 g weight.

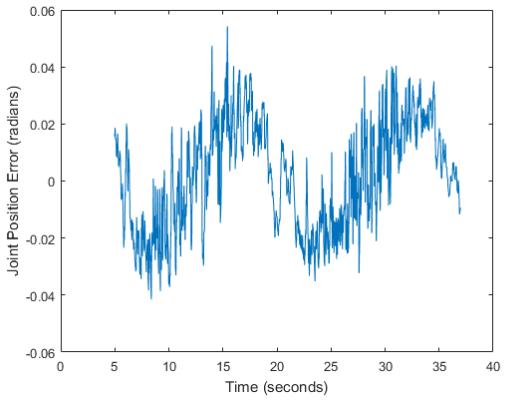

(b) Flexion–extension error during flexion–extension, and ulnar–radial deviation with 500 g weight.

Figure 3.23: Results of the FE motion during FE+UR: error of the output motion.

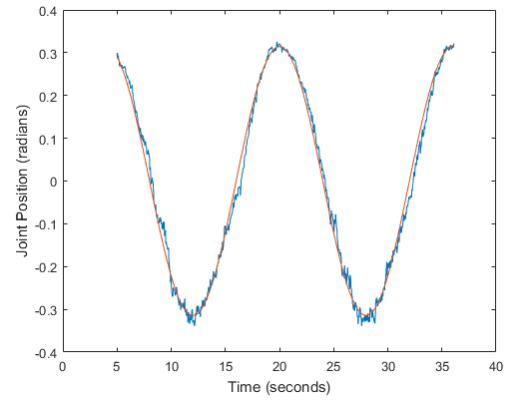

(a) Ulnar–radial deviation motion during flexion–extension, and ulnar–radial deviation with 200 g weight.

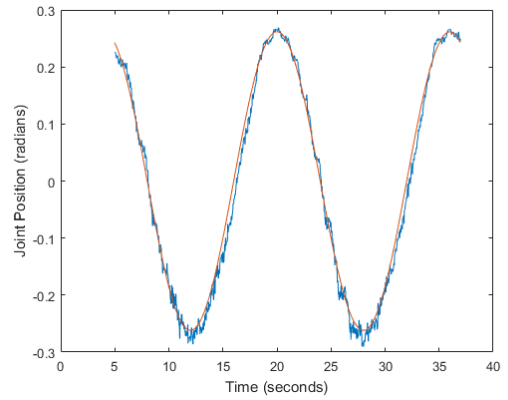

(b) Ulnar–radial deviation motion during flexion–extension, and ulnar–radial deviation with 500 g weight.

Figure 3.24: Results of the UR motion during FE+UR: comparison between input motion (*orange*) and output motion (*blue*).

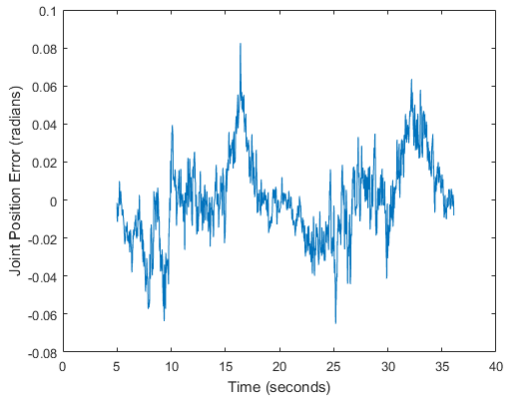

(a) Ulnar–radial deviation error during flexion–extension, and ulnar–radial deviation with 200 g weight.

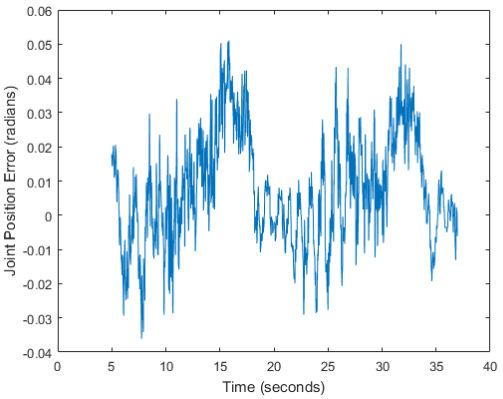

(b) Ulnar–radial deviation error during flexion–extension, and ulnar–radial deviation with 500 g weight.

Figure 3.25: Results of the UR motion during FE+UR: error of the output motion.

Flexion–Extension and Ulnar–Radial Deviation During Pronation–Supination

The flexion–extension and ulnar–radial deviation during pronation–supination action combines the 3 motions shown in Figures 3.13(a), 3.13(b), and 3.13(c). The joints were able to follow the input positions smoothly when using the 200 g weight and the 500 g weight as shown in Figures 3.26, 3.27, 3.28, and 3.29. Tables 3.7 and 3.8 show the root mean square of the errors for the 200 g weight and the 500 g weight respectively. The average errors as a percentage of the maximum range for the flexion–extension is 5.03% when using the 200 g weight and 5.10% when using the 500 g weight. The average errors as a percentage of the maximum range for ulnar–radial deviation is 5.83% when using the 200 g weight and 5.33% when using the 500 g weight.

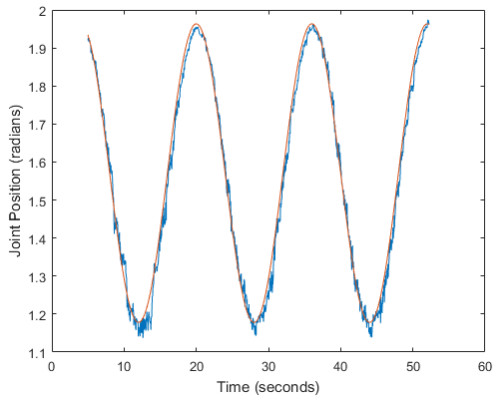

(a) Flexion–extension motion during flexion–extension, ulnar–radial deviation, and pronation–supination with 200 g weight.

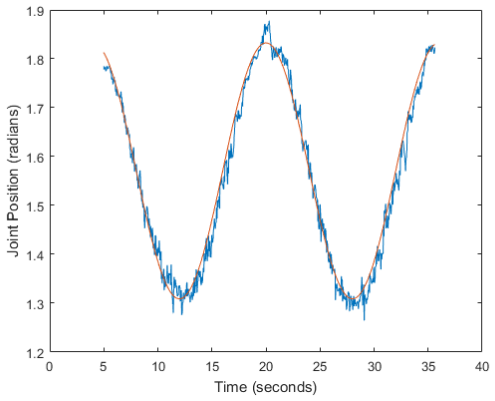

(b) Flexion–extension motion during flexion–extension, ulnar–radial deviation, and pronation–supination with 500 g weight.

Figure 3.26: Results of the FE motion during FE+UR+PS: comparison between input motion (*orange*) and output motion (*blue*).

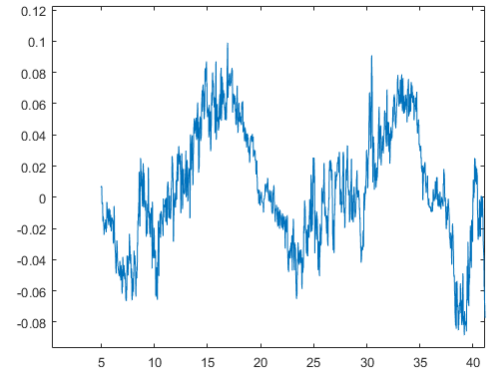

(a) Flexion–extension error during flexion–extension, ulnar–radial deviation, and pronation–supination with 200 g weight.

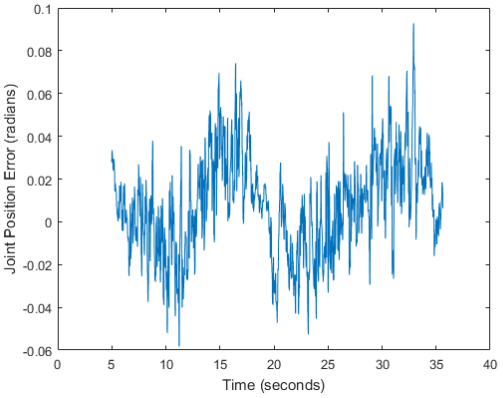

(b) Flexion–extension error during flexion–extension, ulnar–radial deviation, and pronation–supination with 500 g weight.

Figure 3.27: Results of the FE motion during FE+UR+PS: error of the output motion.

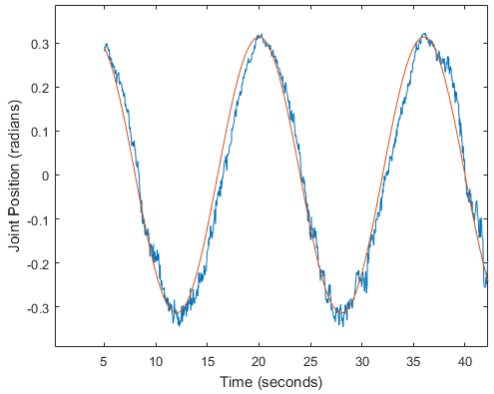

(a) Ulnar–radial deviation motion during flexion–extension, ulnar–radial deviation, and pronation–supination with 200 g weight.

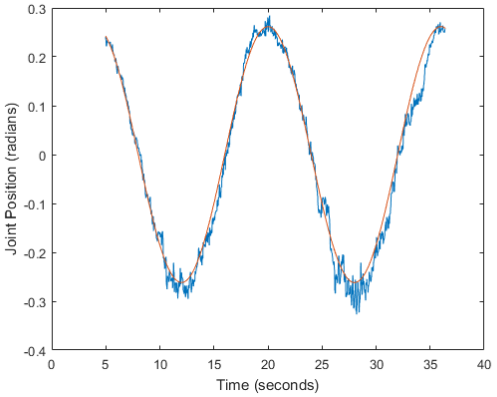

(b) Ulnar–radial deviation motion during flexion–extension, ulnar–radial deviation, and pronation–supination with 500 g weight.

Figure 3.28: Results of the UR motion during FE+UR+PS: comparison between input motion (*orange*) and output motion (*blue*).

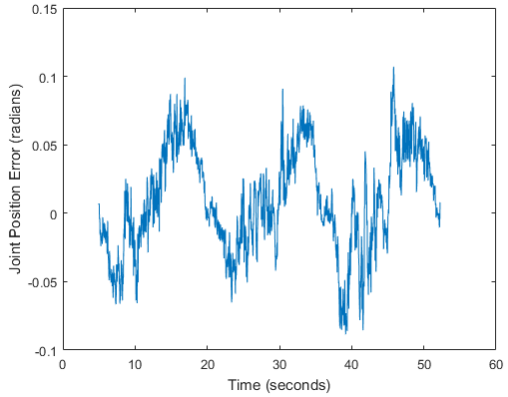

(a) Ulnar–radial deviation error during flexion–extension, ulnar–radial deviation, and pronation–supination with 200 g weight.

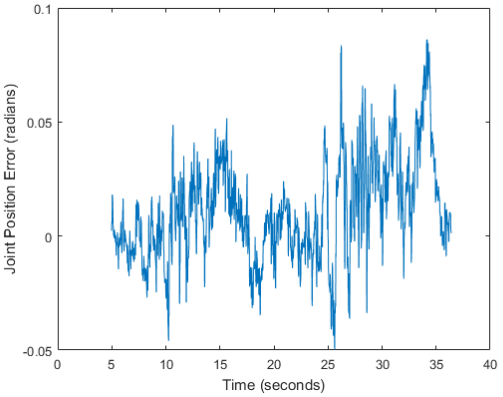

(b) Ulnar–radial deviation error during flexion–extension, ulnar–radial deviation, and pronation–supination with 500 g weight.

Figure 3.29: Results of the UR motion during FE+UR+PS: error of the output motion.

3.7 Discussion

In Section 3.6.2, the motor setup was tested with 6 different actions for two different hand weights. The error between the input position and IMU position was recorded and the RMS errors of each trial are shown in Tables 3.7 and 3.8. For all actions except wrist flexion–extension, wrist ulnar–

Motion	Round	RMS Error (degrees)	Max Error (degrees)	Average RMS Error (degrees/% of range)
FE	1	1.76	4.55	1.76/3.91%
	2	1.76	5.37	
	3	1.76	4.60	
UR	1	0.83	1.99	0.83/1.84%
	2	0.85	2.22	
	3	0.80	2.16	
FE+PS	1	1.52	6.40	1.65/3.67%
	2	1.68	5.41	
	3	1.76	5.21	
UR+PS	1	1.61	4.97	1.30/2.89%
	2	1.23	5.93	
	3	1.06	3.37	
FE error in FE+UR	1	1.35	3.45	1.33/3.69%
	2	1.32	4.07	
	3	1.33	3.64	
UR error in FE+UR	1	1.26	3.84	1.27/3.53%
	2	1.28	3.91	
	3	1.28	4.73	
FE error in FE+UR+PS	1	1.72	6.05	1.81/5.03%
	2	1.78	5.32	
	3	1.93	7.73	
UR error in FE+UR+PS	1	2.24	5.68	2.10/5.83%
	2	1.89	6.69	
	3	2.16	8.13	

Table 3.7: RMS and maximum errors of the motions with a 200 g weight

Motion	Round	RMS Error (degrees)	Max Error (degrees)	Average RMS Error (degrees/% of range)
FE	1	1.30	3.40	1.26/2.80%
	2	1.23	3.47	
	3	1.24	3.48	
UR	1	1.19	2.59	1.24/3.44%
	2	1.23	2.87	
	3	1.29	2.89	
FE+PS	1	1.40	3.68	1.33/2.96%
	2	1.31	3.69	
	3	1.30	4.63	
UR+PS	1	1.74	4.63	1.69/4.69%
	2	1.79	7.05	
	3	1.55	4.58	
FE error in FE+UR	1	1.10	3.11	1.15/3.83%
	2	1.17	3.11	
	3	1.17	3.00	
UR error in FE+UR	1	1.02	2.93	1.06/3.53%
	2	1.02	3.32	
	3	1.14	4.19	
FE error in FE+UR+PS	1	1.53	4.18	1.53/5.10%
	2	1.64	5.40	
	3	1.41	5.32	
UR error in FE+UR+PS	1	1.45	4.94	1.60/5.33%
	2	1.52	6.26	
	3	1.81	5.55	

Table 3.8: RMS and maximum errors of the motions with a 500 g weight

radial deviation, and forearm pronation–supination combined, the RMS error was less than 5% of the range of motion. It is expected that the action combining all three motions would have the highest error because it is experiencing more movement. It was also found that changing the mass of the hand and adjusting the properties in the controller had little effect on the performance of the system.

The setup used an inverse dynamics controller which requires the dynamics and kinematics of the arm to be known. In Section 3.3, the kinematics were determined using the DH convention and the dynamics were determined using an energy-based approach using the Euler-Lagrange equations. The results in Section 3.6.2 show that the inverse dynamics controller works for this application, which indicates that the kinematics and the dynamics of the arm are correct.

In Section 3.6.1, the error of the pitch, roll, and yaw of the IMU was found using the Aurora. The errors are shown in Tables 3.5 and 3.6. The error in the IMUs likely causes a majority of the error when using the inverse dynamics controller. When performing the actions in Section 3.6.2, the wrist flexion–extension action and the wrist ulnar–radial deviation action were done within the IMU's pitch direction, which had a lower error than the yaw direction. When combining multiple motions there is more movement in the yaw direction, which has a higher error causing the error of the controller to increase. While the motor setup did work, it might be better to consider other sensors to replace the IMUs in the future.

It should be noted that the cable attached at the top of the hand and the cable attached at the bottom of the hand for extension and flexion, respectively, do not move at the same rate when flexion or extension occurs. This is a problem because one motor is required to provide both those motions. During testing, the cable at the bottom of the hand was detached so that the motor could only provide extension force. The arm was only rotated to have the gravitational force in the flexion direction. This is a limitation of the current setup that will require a solution if this design is to be implemented in some form as a rehabilitation design.

3.8 Conclusion

Chapter 3 has shown the design and testing of a wrist rehabilitation setup that uses motors for actuation. This method of actuation was shown to work for the application. IMUs used to measure the joint position, were able to measure rotation angles within an error small enough to smoothly control the wrist. The dynamic model and kinematic model of an arm that includes the joints: elbow flexion–extension, forearm pronation–supination, wrist flexion–extension, and wrist ulnar–radial deviation was developed and tested. Its accuracy was confirmed based on the ability of the inverse dynamics controller to track a sinusoidal path. Although the device using motors was shown to work, it has the problem of being heavy and bulky, which is not ideal for a portable and wearable wrist rehabilitation device. A possible solution to this is explored in the following chapter.

Chapter 4

Dielectric Elastomer Actuator Development

In Chapter 3 it was found that a design using motors is able to provide flexion–extension and ulnar–radial deviation at the wrist. A large problem with the design is that it is too large and heavy for a wearable rehabilitation device. Dielectric elastomer actuators (DEAs) are a possible solution to that problem, and the focus of the work presented in this chapter.

To show that this type of actuator is competitive, the work density of DEAs was reviewed. The energy density of silicone films is 0.75 $\frac{J}{cm^3}$ [71]. A DEA attached to the hand similarly to the motor setup in the previous chapter would need to move 6.5 cm and provide a force of up to 35 N to move the hand 90°. If a DEA is made using rectangular strips of a silicone film with dimensions 16.5 cm × 5 cm × 40 μm, the number of strips required to theoretically provide the required work can be calculated with the following equations:

$$W_f = Fd = 35\ N \cdot 6.5\ cm = 2.2750\ J \tag{4.1}$$

$$V_n = \frac{W_f}{e_e} = \frac{2.2750\ J}{0.75\ \frac{J}{cm^3}} = 3.033\ cm^3 \tag{4.2}$$

$$N = \frac{V_n}{l_0 w_0 t_0} = \frac{3.033\ cm^3}{16.5\ cm \cdot 6.5\ cm \cdot 40\ \mu m} = 9.2 \tag{4.3}$$

where W_f is the work required, F is the force required to move the hand, d is the distance the DEA would need to move, V_n is volume of silicone required, e_e is the energy density of silicone, l_0, w_0, and t_0 are the length, width, and thickness of the strip of silicone respectively, and N is the number of strips required. From these equations, the DEA is theoretically capable of providing this motion with 10 strips of silicone film of the dimensions listed previously.

4.1 DEA Modelling

When trying to build a DEA, it is advantageous to be able to model the actuation of the DEA. The stresses in the DEA will be equal to the compressive stress from applying voltage to the electrodes, and stress from the forces applied in the plane of the dielectric film.

The effective compressive stress that results from applying voltage to the electrodes, also known as the Maxwell stress, is described by the following equation [59]:

$$p = \varepsilon_0 \varepsilon_r (V/d)^2 \tag{4.4}$$

where ε_0 is the permittivity of free space, ε_r is the dielectric constant of the dielectric film, V is the voltage applied, and d is the thickness of the film [59]. This model assumes that the electrostatic forces are applied perpendicular to the elastomer film. For small strains ($< 10\%$), linear elasticity and free boundary approximations can be used to find the change in thickness as follows:

$$s_z = -\frac{p}{Y} = -\frac{\varepsilon_0 \varepsilon_r (V/d)^2}{Y} \tag{4.5}$$

where Y is the Young's modulus of the elastomer film [48, 59]. Equation 4.5 can then be used to find the elastic energy density for small strains, given by the following equation [72]:

$$u_e = -\frac{1}{2} p s_z = \frac{1}{2} \frac{(\varepsilon_0 \varepsilon_r)^2 (V/d)^4}{Y}. \tag{4.6}$$

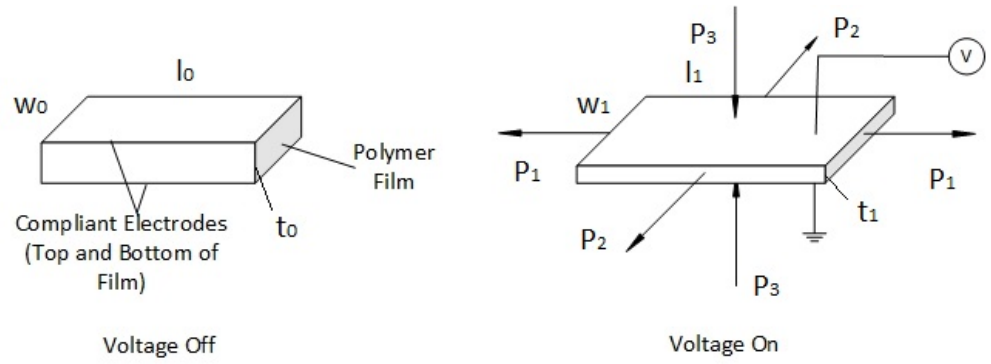

Figure 4.1: Working principle of a DEA.

Equations 4.5 and 4.6 are only acceptable for small strains and they assume linear elasticity. Nonlinear models have been developed that take more factors into account using hyperelasticity models.

There are multiple hyperelasticity models that can be used to describe the strain energy density of the dielectric film such as the Yeoh model [73], Ogden model [74], and Neo-Hookean model [75]. For a DEA such as the one shown in Figure 4.1, the dimensions of the length, width, and thickness are l_0, w_0, and t_0, respectively, when there are no forces applied to the film, and these change to l_1, w_1, and t_1 when a voltage V and mechanical forces P_1, P_2, and P_3 are applied. The dielectric film used in the DEA is considered to be an ideal dielectric elastomer, therefore it is assumed that the dielectric film is incompressible [76], hence:

$$\lambda_1 \lambda_2 \lambda_3 = 1 \tag{4.7}$$

where the stretch, λ_i, is described by

$$\lambda_1 = \frac{w_1}{w_0}, \tag{4.8}$$

$$\lambda_2 = \frac{l_1}{l_0}, \tag{4.9}$$

$$\lambda_3 = \frac{t_1}{t_0}. \tag{4.10}$$

It is also assumed that the permittivity of the film is a constant that is independent of the deformation of the film [65, 76].

The Ogden model describes the free energy density of the dielectric film W_s to be as follows [74]:

$$W_s = \sum_{i=1}^{N} \frac{\mu_i}{\alpha_i}(\lambda_1^{\alpha_i} + \lambda_2^{\alpha_i} + \lambda_3^{\alpha_i} - 3) \tag{4.11}$$

where μ_i and α_i are material parameters, and N is the order of the model. The material parameters must be determined experimentally [65, 77]. This version of the model is only suitable for incompressible materials.

The Yeoh strain energy density function is a form of the Reduced Polynomial model where the order N is set to 3. The Yeoh strain energy density function is described by the following equation [73, 77, 78]:

$$W_s = C_{10}(I_1 - 3) + C_{20}(I_1 - 3)^2 + C_{30}(I_1 - 3)^3 \tag{4.12}$$

where C_{10}, C_{20}, and C_{30} are material parameters, and I_1 is the left Cauchy–Green deformation tensor described by the following equation:

$$I_1 = \lambda_1^2 + \lambda_2^2 + \lambda_3^2. \tag{4.13}$$

Based on the equations, a general electromechanical model can be built using an energy-based approach. Constitutive equations for DEAs have been developed using an energy-based approach where the work done by the mechanical forces on the film and the work done by the power supplied is equal to the increase of the free energy of the dielectric film. Using the energy balance equation and assumptions for ideal dielectric elastomers, the following constitutive equations for DEAs have been developed [56, 65, 76]:

$$\sigma_1 - \sigma_3 = \frac{\lambda_1 \partial W_s(\lambda_1\lambda_2)}{\partial \lambda_1} - \varepsilon_0\varepsilon_r(\frac{V}{t_1})^2 \tag{4.14}$$

$$\sigma_2 - \sigma_3 = \frac{\lambda_2 \partial W_s(\lambda_1\lambda_2)}{\partial \lambda_2} - \varepsilon_0\varepsilon_r(\frac{V}{t_1})^2 \tag{4.15}$$

where σ_1 is the stress in the direction of P_1, σ_2 is the stress in the direction of P_2, and σ_3 is the stress in the direction of P_3. In order to develop an electromagnetic model, it is first necessary to construct and test DEAs that fit the application. The following section outlines the development

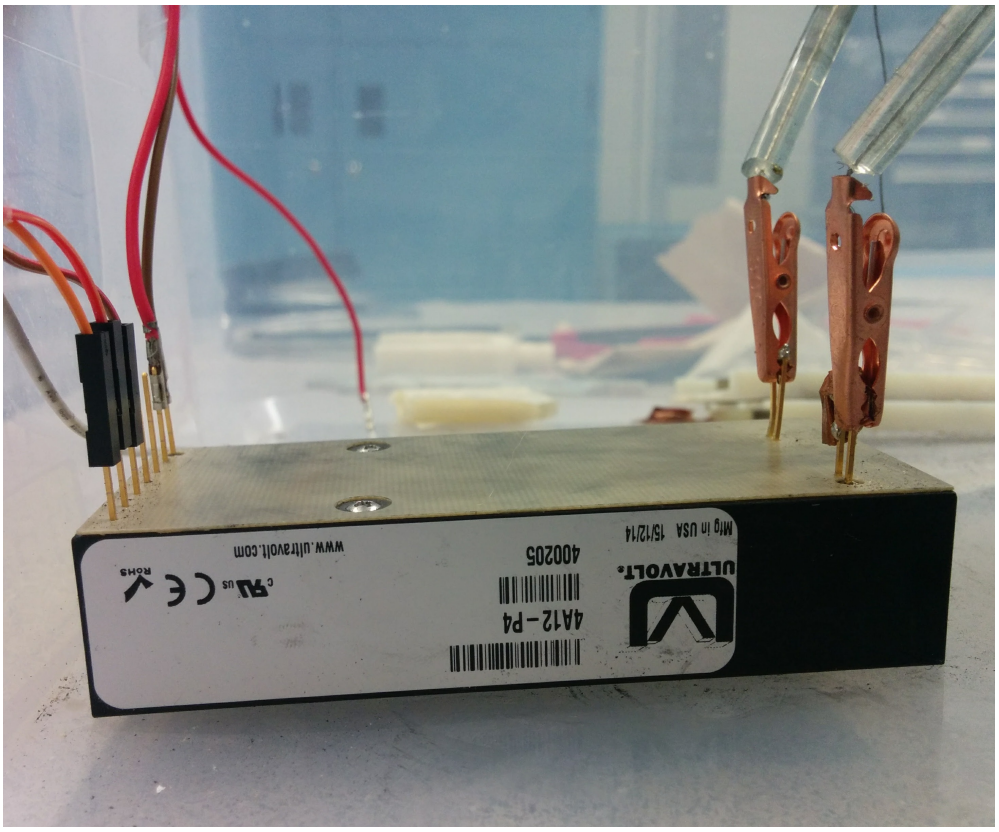

Figure 4.2: High voltage biasing supply.

of the setup that was developed to accomplish this goal.

4.2 Testing Setup

Since DEAs require the supply of high voltages, it was necessary to develop a setup that allowed supplying up to 3000 V of power in a controlled manner. The Ultravolt A-Series high voltage biasing supply was chosen, as shown in Figure 4.2. This supply is capable of supplying a voltage up to 4300 V and a current of 1 mA when connected to a DC power supply that is providing 12 V. The output voltage from the Ultravolt supply can be adjusted using a 10 kΩ digital potentiometer.

Since the DEA requires such a high voltage, there needs to be electrical insulation between the setup and the users to safely use the DEAs. This was done by using a 51 L Sterilite brand clear plastic bin to contain the DEA and high voltage supply. The bin is made of polyethylene and/or polypropylene, which both have high enough dielectric strength to prevent current from the high

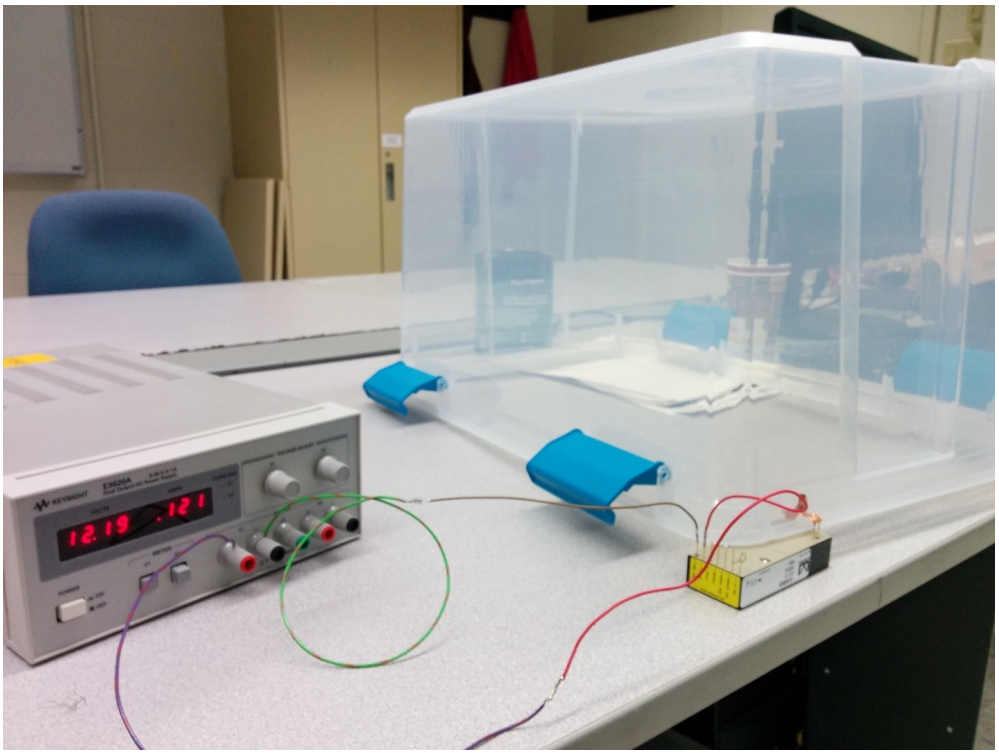

Figure 4.3: Testing an insulating box.

voltage supply from going through its walls. To test for safety, copper tape was attached to either side of one of the walls of the bin and 4300 V was supplied but no arcing between the two leads was noted, as shown in Figure 4.3.

The voltage across the DEA cannot be measured directly with the multimeter because the voltage is too high for the it. To get around this, a voltage divider was attached in parallel to the DEA as shown in Figure 4.4, where $R1 = 100\ M\Omega$ and $R2 = 200\ k\Omega$. The voltage can be measured across R2 then multiplied by 500 to get the voltage across the DEA. The voltage divider also adds a passive discharge path for the DEA.

4.3 Dielectric Elastomer Materials

Once the testing setup was developed, research was performed to determine how to construct a DEA. The first step consisted of identifying the materials that could be used for the DEAs. The results of the research are summarized in this section. The first step consisted of identifying the requirements of the dielectric film. These are as follows:

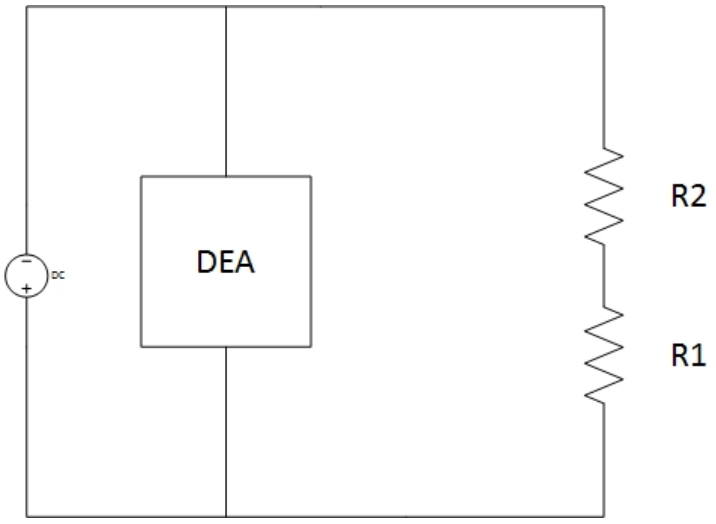

Figure 4.4: Circuit for measuring the voltage across the DEA.

- Needs to be a thin film with uniform thickness. The thinner the film, the lower the voltage requirements.
- Must have high dielectric breakdown strength.
- Must have high relative dielectric constant.
- Must be an incompressible film and show purely elastic behaviour.

The dielectric films most commonly used for dielectric elastomer actuators are silicone, acrylic, and polyurethanes. Acrylic elastomers (most commonly the VHB 4910) have a very high theoretical energy density and are capable of high strains. The VHB 4910 from 3M is the most commonly used acrylic elastomer for DEAs because it can be purchased in rolls, which makes it easy to fabricate the DEA. The downside to the VHB 4910 is that it has a high viscoelasticity, which reduces the response time and reliability of the DEA [62]. Polyurethanes have been looked at because they have a large force output as well as a higher dielectric constant that allows them to be operated at a lower electric field. The downside is that they tend to have lower strain. Silicone elastomers can operate at higher frequencies because of their lower viscoelasticity but they are not capable of generating a strain as high as acrylic elastomers [48].

To actuate the dielectric film, an electrode needs to be applied to both sides of the film. The requirements of these compliant electrodes are as follows:

- Must show negligible stiffness or else it will reduce the strain during actuation.
- They must be able to remain conductive during and after sustaining large deformations.
- They should also remain conductive after millions of cycles of large deformations [79].

While the chosen dielectric film has important requirements that effect the response of the actuator, it is important that the electrodes meet the listed requirements so they do not inhibit the actuator. These requirements mean that simply placing a conductive piece of metal on either side of the dielectric film would be ineffective. Instead, carbon based electrodes are most commonly used for DEAs because they have low impact on stiffness, are able to remain conductive at large strains, and are not difficult to apply [59, 79, 80].

Carbon-based electrodes can be divided into 3 main categories, as described below:

1. **Carbon powder electrodes** are loose particles of carbon on the dielectric film. The carbon powder electrodes do not add any stiffness to the film, which gives them a large advantage over the other electrodes. This is because the loose particles do not have a strong binding force to each other, which allows them to move freely as the dielectric film stretches. The disadvantages of using carbon powder electrodes is that they can have a shorter lifetime due to the carbon particles falling off, as well as not being able to fully cover the film at higher strains.

2. **Carbon grease electrodes** consist of a carbon powder dispersed in a viscous oil. Carbon grease electrodes have the advantages of being inexpensive and easy to apply making them very popular electrodes for DEAs. Unlike the carbon powder electrodes, they are able to maintain coverage of the film over a large area strain [64]. The disadvantages to using carbon grease are that they can have shorter lifetimes due to drying or diffusion [79] and it has a weak adhesion to the film which can cause the grease to be messy and possibly spread where it is unwanted.

3. **Conductive rubber** is an elastomer that has had carbon particles dispersed in it and is then cross-linked to the dielectric film [53, 79]. For this type of electrode, the electrode is

bound to the dielectric film; therefore, there is no risk of the carbon moving to other parts of the electrode or falling off. The main disadvantage of conductive rubber electrodes is that the stiffness of the electrode is not negligible because it is bound to the dielectric film.

The application of the electrode is also important in making an effective DEA. Ideally the method for applying the electrode should be able to apply the electrode precisely and such that the electrode layer has a uniform thickness.

One method of electrode application is by placing a shadow mask on the surface of the dielectric film then adding the electrode by either spraying or brushing it on. If a uniform thickness is not important then using a brush to apply the electrode is acceptable [59, 81, 82]. For a uniform thickness, spray coating can be used with the shadow mask to apply the electrode.

Another method for applying the electrode to the membrane is pad printing. Pad printing is done by etching the pattern for the electrode onto a steel plate. The etched area is filled with the electrode material and a stamp is pressed over it, then stamped onto the membrane, which leaves the electrode on the membrane when the stamp is removed. This method is usually done with carbon grease or with a conductive rubber that has been diluted. It can also be used with carbon powder as long as the powder can attach to the membrane of the film, such as with the VHB 4910 [79, 80, 83, 84].

For this thesis, the dielectric film chosen was a 40 μm thick silicone dielectric film that was purchased from Parker Hannifin. The silicone film was chosen because it does not require the same prestretch that the VHB 4910 would require to meet the desired thickness of the material, and it's lower viscoelasticity gives the DEA a better response time. The electrode chosen for this thesis is a carbon powder based electrode that is made into a conductive ink to be sprayed onto the film. The conductive ink was chosen because it can be easily fabricated and does not add any stiffness to the actuator. The carbon particles do start to fall off after some time but each DEA is only used soon after fabricating it so that does not affect the results. The preparation of the conductive ink and the method of fabricating the DEAs is described in the following section.

4.4 DEA Fabrication

As reviewed in the previous section, DEA fabrication requires creating an electrode, and applying the electrode to the dielectric film over the desired area. The material chosen for the dielectric film was a 40 μm thick silicone based dielectric film that was purchased from Parker Hannifin. Purchasing the film instead of fabricating it reduces the number of steps for fabricating the DEA, and some material properties such as the dielectric strength are already given. The electrode chosen for the DEAs is a graphite powder electrode mixed with isopropanol and isooctane so it can be sprayed onto the dielectric film. The process of the DEA fabrication involves first creating the conductive ink electrode, then attaching the dielectric film to a frame, and lastly the conductive ink is sprayed onto the dielectric film where it is left to dry overnight. The procedure is as follows:

1. In a 150 mL glass beaker, add 0.8 g of graphite powder (with average particle size of 5 μm) and 16 g of 2-propanol. Mix at 1500 rpm for 20 minutes with an overhead stirrer, such as the one in Figure 4.5.

2. Next add, 11 g of isooctane (2,2,4-trimethylpentane) to the beaker and mix at 1250 rpm for 30 minutes.

The conductive ink made by Rosset *et al.* [83] uses 16 g of isooctane instead of 11 g of isooctane. Different amounts of isooctane were empirically tested, and it was determined that 11 g of isooctane had the best result for spraying the electrode onto the film.

Figure 4.6 shows the 3D printed end pieces of the DEA, which are used for attaching the film to the arm. Each end of the film has 2 of the end pieces clamped onto the film and they are held together with 2 nuts and 2 screws. The third hole is used to attach the DEA to the arm. Figure 4.7 shows the 3D printed mask to cover the edges of the dielectric film when spraying the electrode onto it. The mask also serves as a frame during spraying by keeping the film stretched. The ends each have a slot for the end pieces and holes at the end that are large enough to fit the screw heads and nuts being used to clamp the end pieces together. The open area is a 4.2 cm by 14.6 cm area where the dielectric film will be sprayed by the electrode. There was a small wall added between the end piece slots and the open inside area so that the electrode would not go to the very edge of

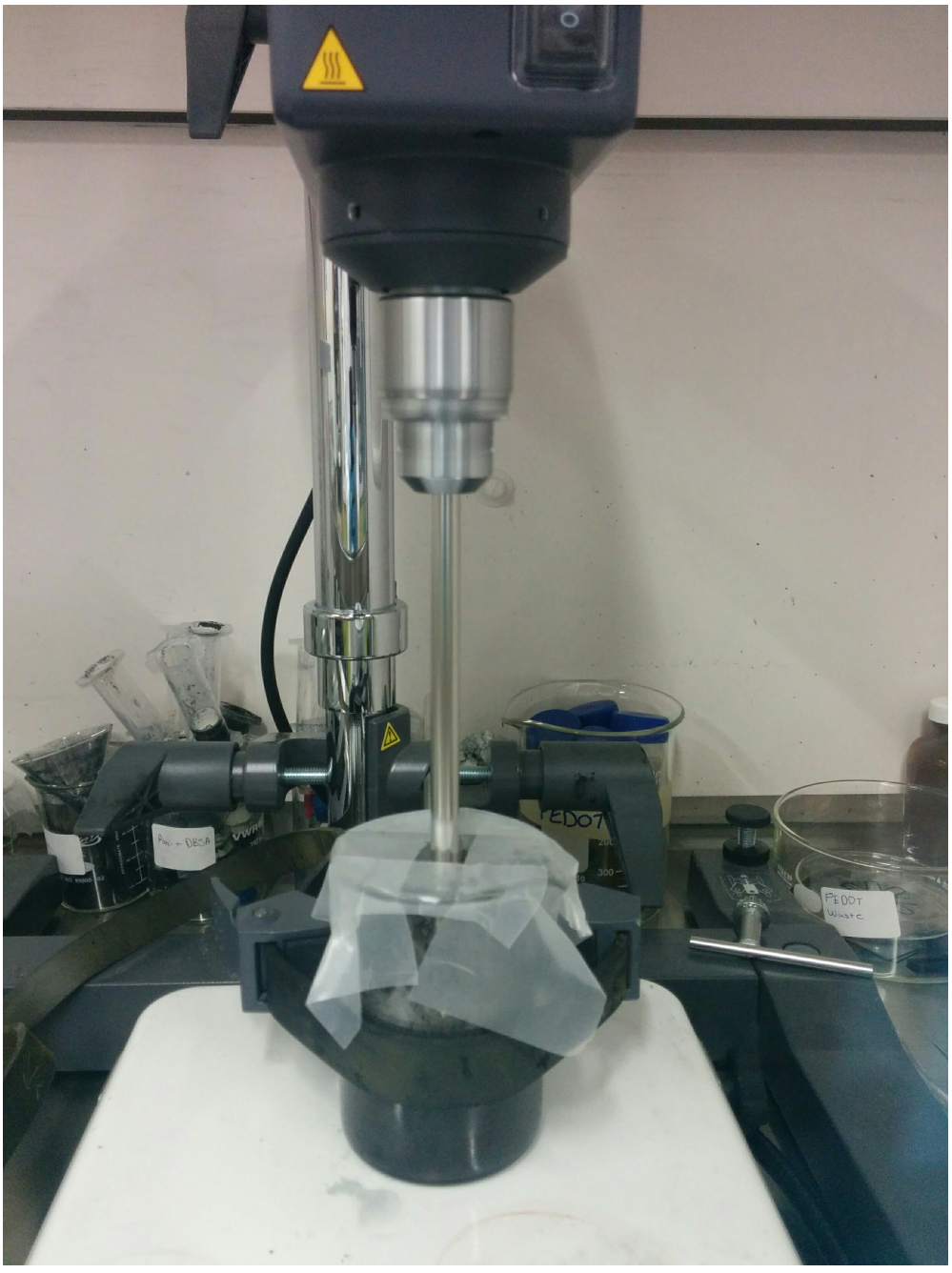

Figure 4.5: Overhead stirrer used to mix the electrode mixture.

the end piece. The part of the film that is at the edge of the end pieces could be slightly thinner from the clamping end pieces so adding a space between the end pieces and where the electrode goes on will help avoid dielectric breakdown.

Once the conductive ink had been prepared, it needed to be sprayed on to the dielectric film.

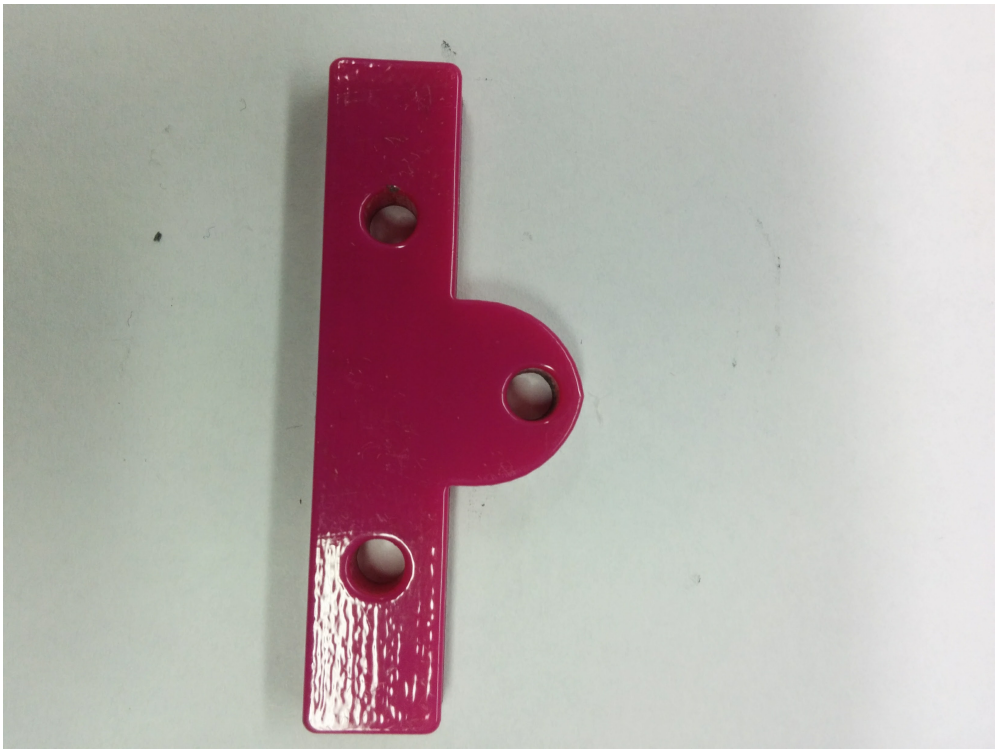

Figure 4.6: DEA end piece that is used to attach the DEA to the arm.

The process for preparing the dielectric film and spraying the electrode onto it is as follows:

1. A strip of film that is 52 mm by 165 mm is cut from the roll using a box cutter and a square tool to run the knife along. Originally, scissors were used to cut the strip but it was found that the cuts were not perfectly straight, which would likely affect the performance of the DEA. The end pieces were placed in the slots in the mask parts.

2. The protective layer on one side of the dielectric film was removed. The dielectric film was then placed on top of one of the masks with the end pieces in it. The protective layer on the other side of the dielectric film was then carefully removed.

3. The other mask with end pieces was placed on top of the film. The mask and end pieces were then screwed together as shown in Figure 4.8. The holes in the mask were not used because the dielectric film would have been touching the edge of the screws, which might have damaged the film. Attaching the screws at the side such as in Figure 4.8 worked perfectly for holding the masks together. Also, the screws on the distal end of the arm were changed

Figure 4.7: DEA mask for when the electrode is sprayed on the film.

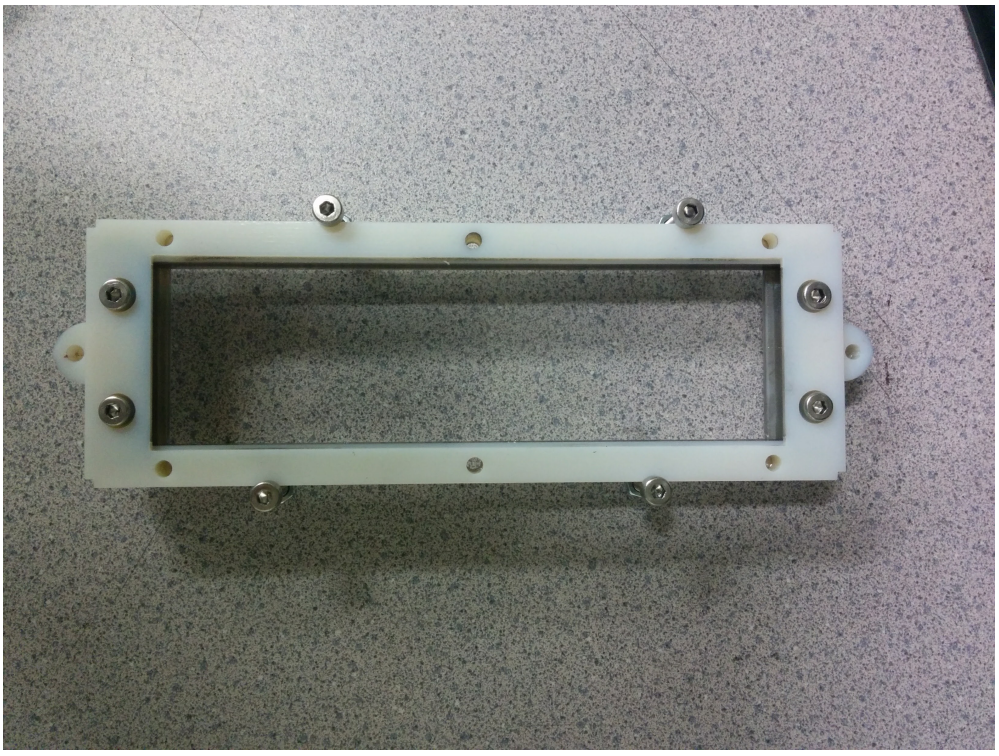

Figure 4.8: Dielectric film in the frame.

to plastic, so that that end would be lighter.

4. The conductive ink will be sprayed onto the film using an air brush. The conductive ink put in a small bottle with a lid that attaches to the air brush and an air supply was connected to the air brush. The dielectric film in between the mask was held inside a plastic bin inside a fumehood and the airbrush was used to spray the conductive ink on to the dielectric film. The air brush was held roughly 120 mm away from the film while spraying. The conductive ink was sprayed over the film until it was fully covered in the ink. Most of the dielectric film only had one pass of the conductive ink sprayed onto it. The DEA constructed is shown in Figure 4.9.

5. After both sides of the dielectric film were covered in the conductive ink, the DEA was left in the fumehood for 16 to 20 hours for the conductive ink to dry.

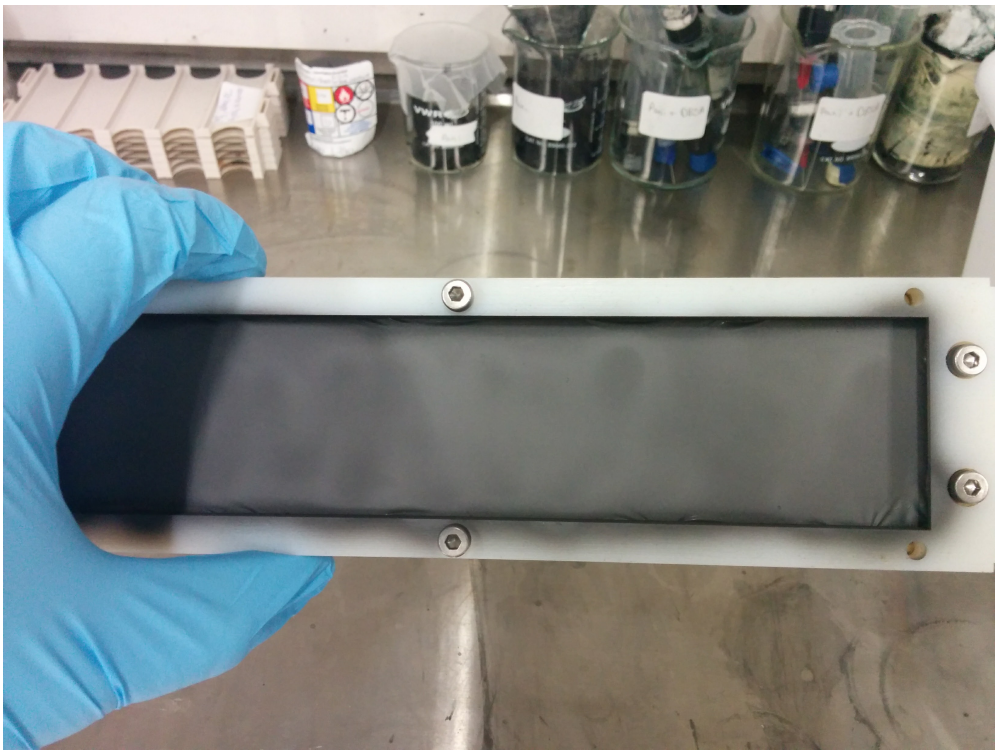

Figure 4.9: Electrode sprayed onto film in the frame.

4.5 Dielectric Elastomer Actuator Evaluation

An experiment was conducted to characterize dielectric elastomer actuators fabricated using the method shown in Section 4.4, so that their performance can be compared to the requirements of a wrist rehabilitation device and to the performance of a DC motor as presented in Chapter 3. The details are shown in the following sections.

4.5.1 Methods

The DEAs were fabricated as shown in Section 4.4 and were then tested within 48 hours. It has not been determined if there are any negative effects due to aging of the electrode, but it is possible that the graphite particles may detach from the film over time. To test the DEAs, both ends were attached onto the arm as shown in Figure 4.10 so that it would remain stretched when the frame was removed. The frame was then carefully removed from the DEA. Next, the weight was attached to the free end of the DEA with fishing line. The fishing line was routed over a metal pin and a weight was hung from the end of the arm as shown in Figure 4.11.

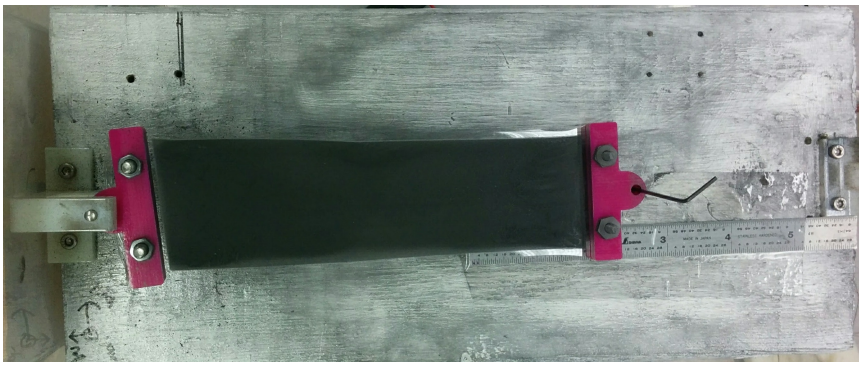

Figure 4.10: DEA when it is first attached to the arm and the frame is removed.

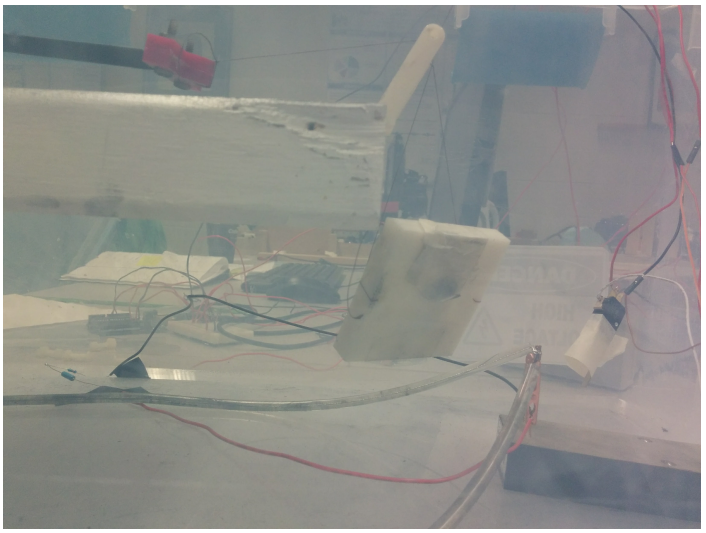

Figure 4.11: The weight that is attached to the DEA.

To characterize the DEA, it was necessary to measure the voltage across the DEA, the current from the power supply, the initial position of the DEA, and the actuated positions of the DEA at various voltage levels with different weights attached. The voltage across the DEA was measured using a multimeter with a voltage divider as explained in Section 4.2. The current from the power supply was recorded as displayed by the power supply.

In order to measure the DEA positions, a ruler was placed 2 cm below the DEA. As the DEA moved, video was recorded using an 8 megapixel digital camera with 1920×1080 resolution at 30 frames per second that was fixed to the lid of the box, approximately 17 cm above the DEA, pointing down towards the DEA. The video was then downloaded onto a computer and screenshots were taken using VLC Media Player before actuation and after the actuator settled.

For each screen shot, the distance traveled was measured using ImageJ (National Institute of Health, Bethesda, MD). The change in length of the DEA was determined through filming the actuation because other available sensors would have affected the performance of the DEA. The Aurora electromagnetic tracking system that was used in Section 3.6.1 was not used because there is a risk of damage from the high voltage. This high voltage may have affected the readings. There will be some error due to parallax, which should be considered when reviewing the results.

Once the DEA was mounted and the weight attached to the free end, the rod holding the free end was removed and the DEA was slowly stretched to a resting position with the weight pulling on it. The lid was placed on the box, the recording would start, and then the power was turned on starting at 1000 V. Once the DEA settled, the power was turned off and the filming was stopped. Once the DEA was fully discharged, the lid was removed and the DEA was moved back to its starting position. This process was repeated, incrementing the voltage by 200 V up to 2200 V. Once 2200 V was reached, the DEA was moved back to the position with the rod holding the free end in place and the weight was increased by 10 g with a starting weight of 45 g. The process of recording from 1000 V to 2200 V was then repeated. The weight would then be increased by another 10 g and this would be repeated until the DEA was stretched too far to move on the arm, or until it broke. This process was used for the first 5 DEAs. Starting at DEA number 6 for the remainder of the DEAs, the DEA would start at 1000 V and go up to 2000 V in increments of 200 V without discharging. The maximum voltage was decreased because 2200 V was getting too close to the breakdown voltage, which was causing the DEAs to break. The results of the trial are presented in the following section.

4.5.2 Results

To measure the movement in ImageJ, an initial measurement of pixels per inch needed to be determined. This was accomplished by loading the screenshot of the starting position and drawing a line that was 1 inch along the ruler, as shown in Figure 4.12. Next, a line is drawn along the left side of the ruler from the edge of the DEA end piece to the 4 inch marking on the ruler. This measurement was used to calculate the 0 V position. The screenshot after 1000 V was supplied is then loaded into ImageJ. The line from the previous screenshot would then be on the new

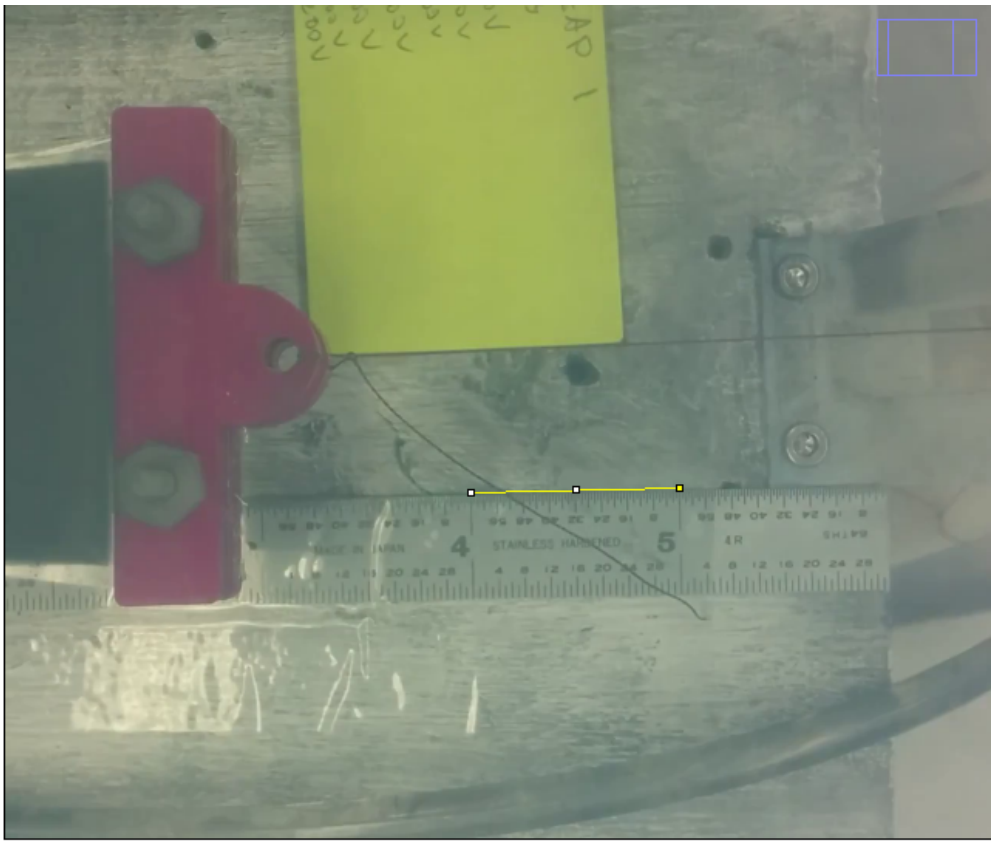

Figure 4.12: Procedure for determining the scale for pixels to inches in ImageJ.

screenshot. Assuming that the camera did not move at all during recording, the end of the line that was on the edge of the DEA end piece in the starting position screenshot would mark the starting position on the 1000 V screenshot. The end of the line that was at the 4 inch line before was then moved to where the DEA end piece was in the 1000 V screenshot as shown in Figure 4.13. The length of the line was then used with the previously measured scale to calculate the distance the DEA moved in inches. This process was repeated for each voltage. The strain was calculated from this using the distance between the end pieces while the film is unstretched as the original length.

The change in length and the voltage was measured for each DEA, and the strain and stress in the DEAs were calculated and recorded. Only four of the DEAs, out of twelve, performed as required. The other eight DEAs failed during actuation with the 45 g mass. The strain values for the DEAs that failed are shown in Table 4.1. Unavailable values indicate that the DEA failed

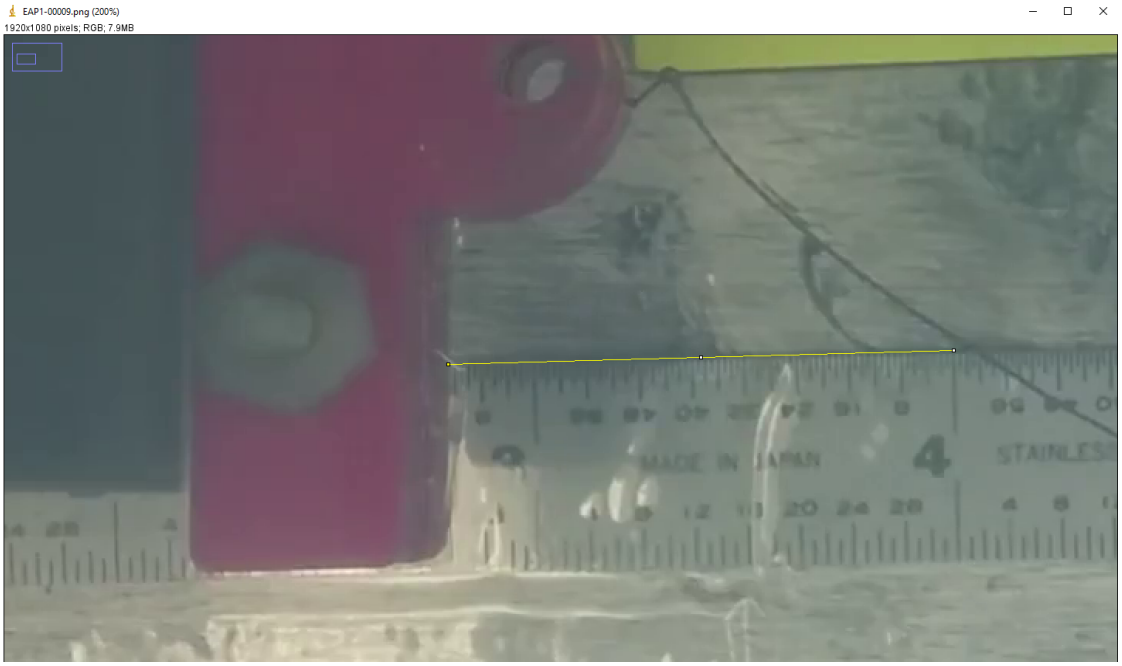

(a) ImageJ measurement start point.

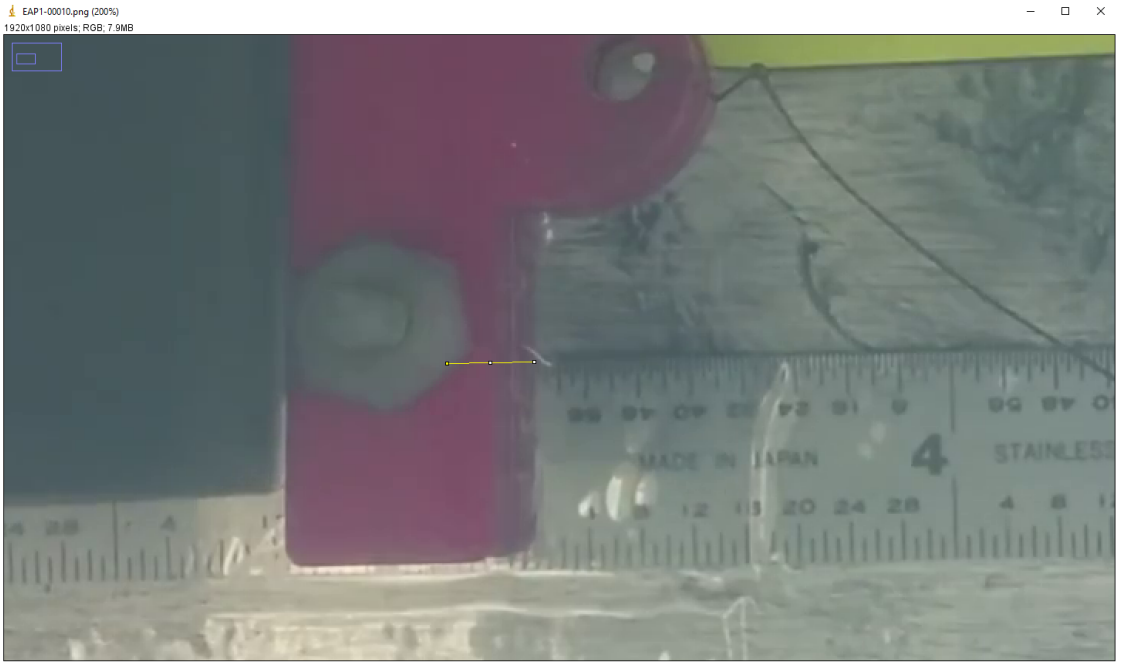

(b) ImageJ measurement end point.

Figure 4.13: Measuring positions with ImageJ.

Voltage (V)	DEA #2	DEA #3	DEA #4	DEA #5	DEA #7	DEA #8	DEA #10	DEA #12
0	0.36	0.36	0.39	0.38	0.36	0.36	0.36	—
1000	0.38	0.36	0.40	0.39	0.37	0.37	0.36	—
1200	0.38	0.39	0.41	0.40	0.39	0.39	0.37	—
1400	0.40	0.40	0.42	0.41	—	0.41	0.39	—
1600	0.41	0.41	0.45	0.44	—	0.42	0.39	—
1800	0.43	0.45	0.47	—	—	0.45	0.41	—
2000	0.52	—	—	—	—	—	—	—
2200	—	—	—	—	—	—	—	—

Table 4.1: Strain values for DEA's that did not perform as required at 45 g. Unavailable values indicate that the DEA broke before data could be gathered at that voltage.

	DEA #1	DEA #6	DEA #9	DEA #11
l_0	117.1 mm	130.6 mm	130.0 mm	116.6 mm

Table 4.2: Unstretched lengths of each working DEA.

before data could be recorded at that voltage.

Each DEA had a different unstretched length due to variations when fabricating the DEAs. The starting length for each DEA that performed as required is displayed in Table 4.2.

DEA #1

DEA #1 was actuated from 1000 V to 2200 V in increments of 200 V. It was actuated with a mass of 45 g up to 95 g hanging from the edge. The data for 95 g was not included in the analysis, as the DEA was being stretched too close to the end of the arm at 95 g, which affected

Commanded Voltage (V)	45 g		55 g		65 g		75 g		85 g	
	Strain	Stress (MPa)	Strain	Stress (MPa)	Strain	Stress (MPa)	Strain	Stress (MPa)	Strain	Stress (MPa)
0	0.57	0.34	0.70	0.45	0.82	0.56	0.97	0.71	1.07	0.84
1000	0.59	0.34	0.72	0.45	0.84	0.57	0.97	0.71	1.10	0.86
1200	0.60	0.34	0.72	0.45	0.83	0.57	0.98	0.71	1.11	0.86
1400	0.61	0.34	0.74	0.45	0.86	0.58	0.99	0.71	1.12	0.86
1600	0.62	0.35	0.78	0.47	0.89	0.59	1.00	0.72	1.13	0.87
1800	0.65	0.35	0.79	0.47	0.93	0.60	1.05	0.74	1.13	0.87
2000	0.67	0.36	0.82	0.48	0.94	0.60	1.07	0.74	1.13	0.87
2200	0.73	0.37	0.84	0.48	0.96	0.61	1.09	0.75	1.16	0.88

Table 4.3: Stress and strain values of DEA 1.

Commanded Voltage (V)	45 g		55 g		65 g		75 g	
	Strain	Stress (MPa)	Strain	Stress (MPa)	Strain	Stress (MPa)	Strain	Stress (MPa)
0	0.56	0.33	0.69	0.44	0.87	0.58	0.92	0.69
1000	0.57	0.34	0.72	0.45	0.88	0.58	0.93	0.69
1200	0.58	0.34	0.73	0.45	0.89	0.59	0.95	0.70
1400	0.60	0.34	0.76	0.46	0.91	0.59	0.96	0.70
1600	0.63	0.35	0.78	0.47	0.93	0.60	0.98	0.71
1800	0.66	0.35	0.80	0.47	0.96	0.61	1.00	0.72
2000	0.69	0.36	0.83	0.48	0.97	0.61	1.01	0.72
2200	0.73	0.37	—	—	—	—	—	—

Table 4.4: Stress and strain values of DEA 6.

Commanded Voltage (V)	45 g		55 g		65 g		75 g	
	Strain	Stress (MPa)	Strain	Stress (MPa)	Strain	Stress (MPa)	Strain	Stress (MPa)
0	0.56	0.33	0.71	0.45	0.85	0.57	0.99	0.71
1000	0.57	0.34	0.71	0.45	0.87	0.58	0.99	0.71
1200	0.58	0.34	0.72	0.45	0.88	0.58	1.02	0.73
1400	0.60	0.34	0.74	0.46	0.89	0.59	1.03	0.73
1600	0.61	0.34	0.76	0.46	0.93	0.60	1.03	0.73
1800	0.65	0.35	0.78	0.47	0.94	0.60	1.04	0.73
2000	0.66	0.35	0.81	0.47	0.95	0.61	1.05	0.74

Table 4.5: Stress and strain values of DEA 9.

Commanded Voltage (V)	45 g		55 g		75 g		85 g		95 g	
	Strain	Stress (MPa)	Strain	Stress (MPa)	Strain	Stress (MPa)	Strain	Stress (MPa)	Strain	Stress (MPa)
0	0.56	0.33	0.73	0.45	0.97	0.71	1.15	0.88	1.26	1.03
1000	0.58	0.34	0.74	0.46	1.00	0.72	1.16	0.88	1.26	1.03
1200	0.59	0.34	0.75	0.46	1.00	0.72	1.17	0.88	1.27	1.03
1400	0.60	0.34	0.75	0.46	1.04	0.73	1.19	0.89	1.29	1.04
1600	0.63	0.35	0.77	0.46	1.06	0.74	1.20	0.89	1.31	1.05
1800	0.67	0.36	0.79	0.47	1.09	0.75	1.21	0.90	1.32	1.06
2000	0.69	0.36	0.82	0.48	1.10	0.75	1.23	0.91	1.33	1.06

Table 4.6: Stress and strain values of DEA 11.

	45 g	55 g	65 g	75 g	85 g	95 g
	Increase in strain	Increase in strain	Increase in strain	Increase in strain	Increase in strain	Increase in strain
DEA #1	0.10	0.12	0.11	0.10	0.06	–
DEA #6	0.13	0.13	0.10	0.09	–	–
DEA #9	0.09	0.09	0.10	0.06	–	–
DEA #11	0.13	0.09	–	0.12	0.07	0.07

Table 4.7: Increase in strain from 0 V to 2000 V for each DEA at each mass.

	45 g	55 g	65 g	75 g	85 g	95 g
	Increase in stress (kPa)	Increase in stress (kPa)	Increase in stress (kPa)	Increase in stress (kPa)	Increase in stress (kPa)	Increase in stress (kPa)
DEA #1	22	32	36	36	24	–
DEA #6	29	36	32	34	–	–
DEA #9	21	26	31	22	–	–
DEA #11	28	23	–	46	30	33

Table 4.8: Increase in stress from 0 V to 2000 V for each DEA at each mass.

the measurements. The strain and stress for each mass and voltage were recorded and are shown in Table 4.3. Figure 4.14 shows the plot of voltage vs. strain for DEA 1.

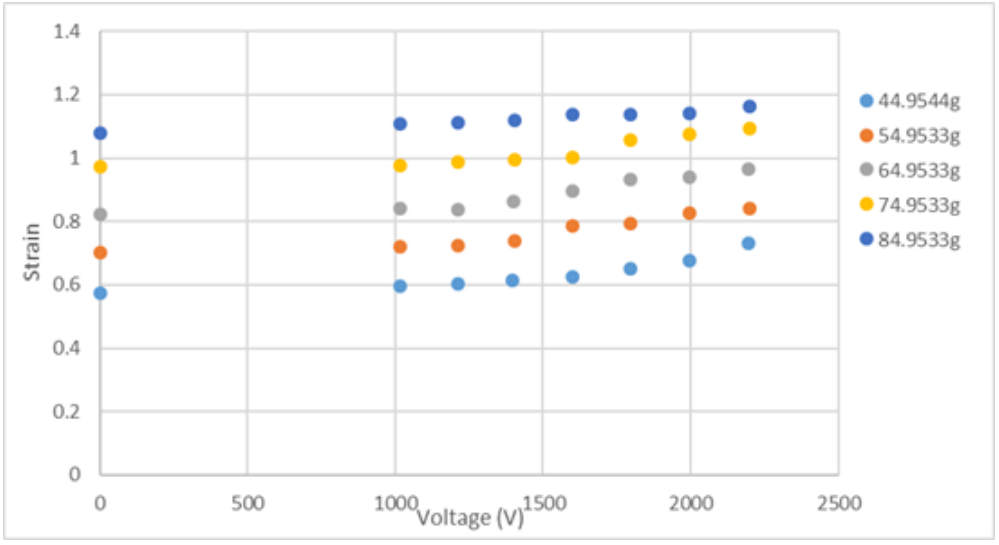

Figure 4.14: Voltage vs. strain for DEA 1.

DEA #6

DEA #6 was actuated from 1000 V to 2000 V in increments of 200 V. It was actuated with a mass of 45 g up to 75 g hanging from the edge. At 85 g the DEA was stretched too close to the edge of the arm. The strain and stress for each mass and voltage were recorded and are shown in Table 4.4. Figure 4.15 shows the plot of voltage vs. strain for DEA 6.

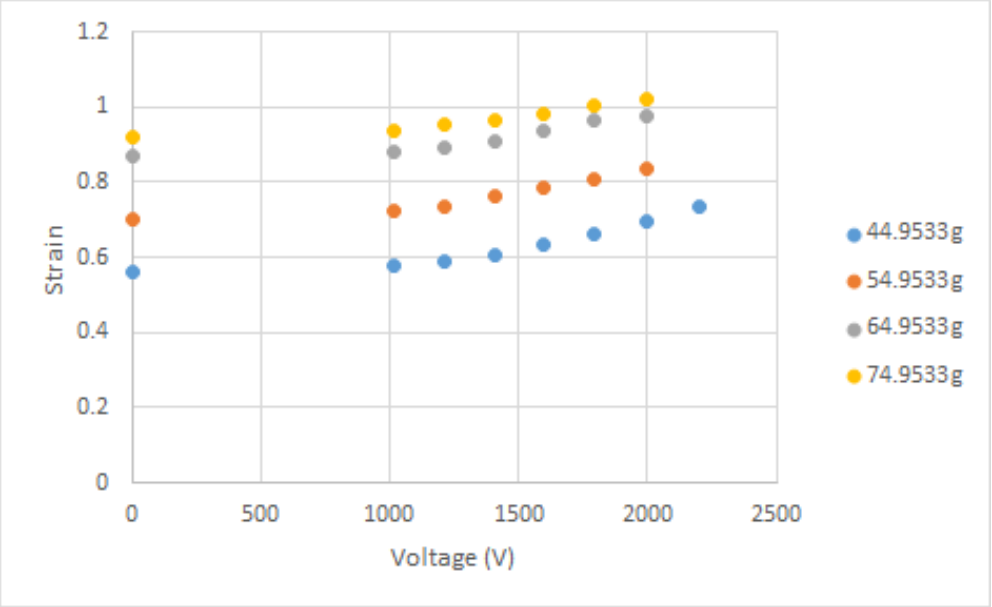

Figure 4.15: Voltage vs. strain for DEA 6.

DEA #9

DEA #9 was actuated from 1000 V to 2000 V in increments of 200 V. It was actuated with a mass of 45 g up to 75 g hanging from the edge. At 85 g the DEA was stretched too close to the edge of the arm. The strain and stress for each mass and voltage were recorded and are shown in Table 4.5. Figure 4.16 shows the plot of voltage vs. strain for DEA 9.

DEA #11

DEA #11 was actuated from 1000 V to 2000 V in increments of 200 V. It was actuated with a mass of 45 g up to 95 g hanging from the edge. The recording at 65 g had no movement from 1200 V to 2000 V, and therefore, that recording was removed from the analysis. The strain and stress for each mass and voltage were recorded and are shown in Table 4.6. Figure 4.17 shows the plot of voltage vs. strain for DEA #11.

The increase in strain and stress for DEA #1, DEA #6, DEA #9, and DEA #11 at each mass

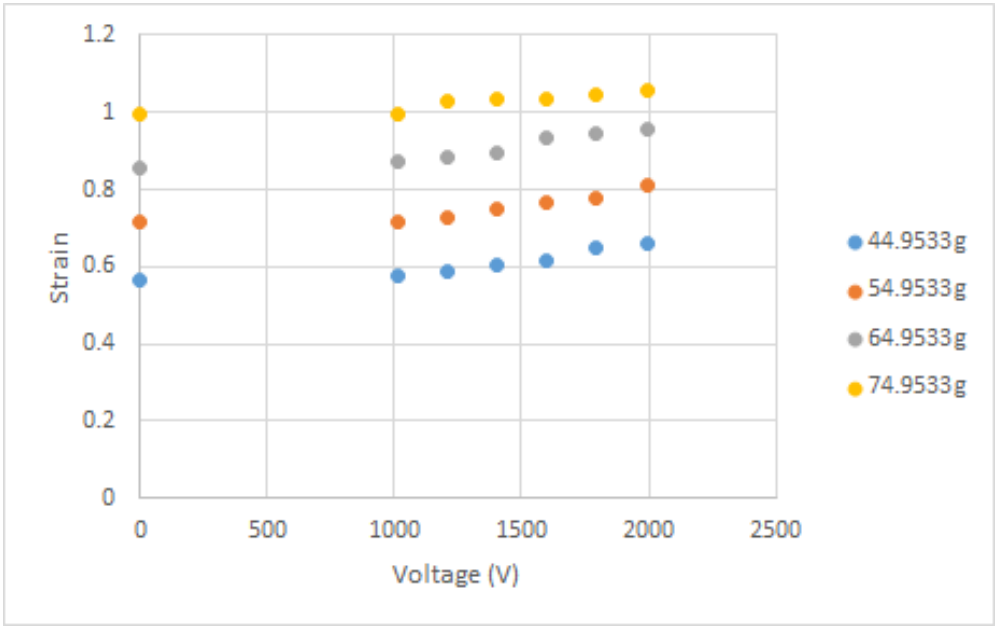

Figure 4.16: Voltage vs. strain for DEA 9.

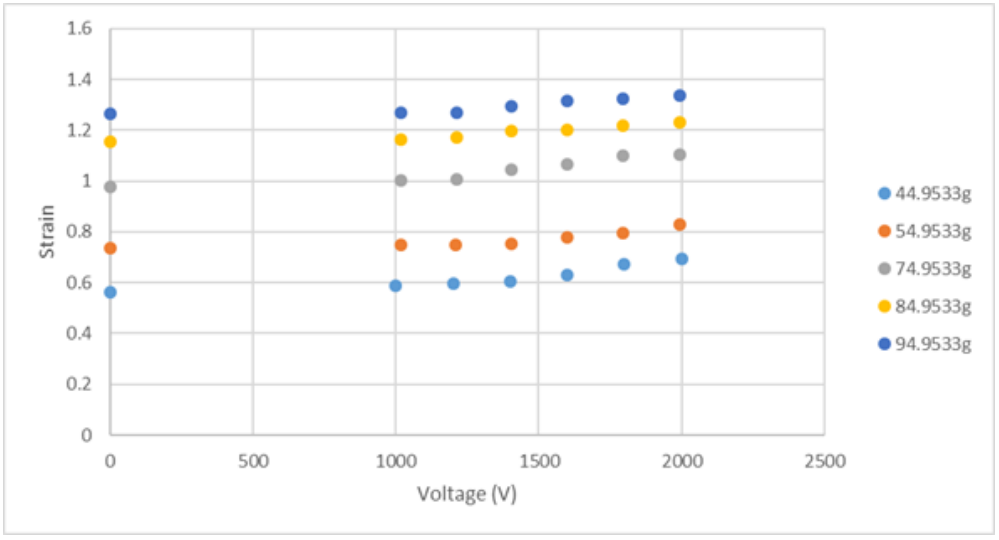

Figure 4.17: Voltage vs. strain for DEA 11.

when supplying 0 V to 2000 V were shown in Tables 4.7 and 4.8.

The strain in the width direction is affected by the strain in the length direction and the voltage. To analyze this relationship, Figure 4.18 shows the strain in the length direction against the stretch ratio in the width direction for DEA #9 with 0 V. Figure 4.19 plots the voltage against the stretch ratio in the width direction for DEA #9 with a 65 g weight. The DEA and weight

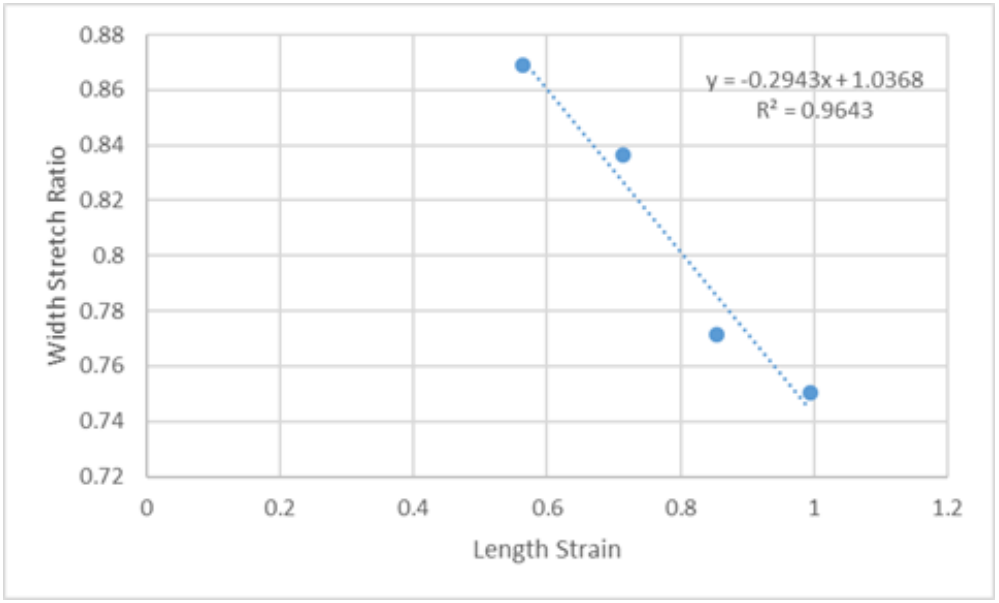

Figure 4.18: Strain in the length direction vs. the stretch ratio in the width direction with 45 g to 75 g and 0 V applied from DEA 9. The equation is used when relating λ_1 with λ_2.

was chosen arbitrarily. The width stretch ratio for both scenarios was measured using ImageJ. A line of best fit was plotted along with the data points and the corresponding equations were determined. These can later be used to relate the width stretch ratio with the strain in the length direction and the voltage applied.

4.5.3 Discussion

In this experiment, 8 out of the 12 DEAs broke during testing at 45 g. The cause of failure was not apparent for all cases, except for one of the failing DEAs. DEA #10 failed due to dielectric breakdown as shown in Figure 4.20. Dielectric breakdown occurs when the electric field exceeds the dielectric strength of the dielectric film, which causes a conductive path to form between the electrodes and the discharge will burn through the dielectric film creating a small hole similar to the one shown in Figure 4.21. The dielectric film likely has impurities at some locations, which means that dielectric breakdown can happen at those locations with an electric field that is lower than the dielectric strength. All of the DEAs that broke, except for DEA #10, tore along the width of the DEA. The cause of failure for those DEAs was not evident but it was likely due to dielectric breakdown creating a hole in the dielectric film and the tension from the weight causing

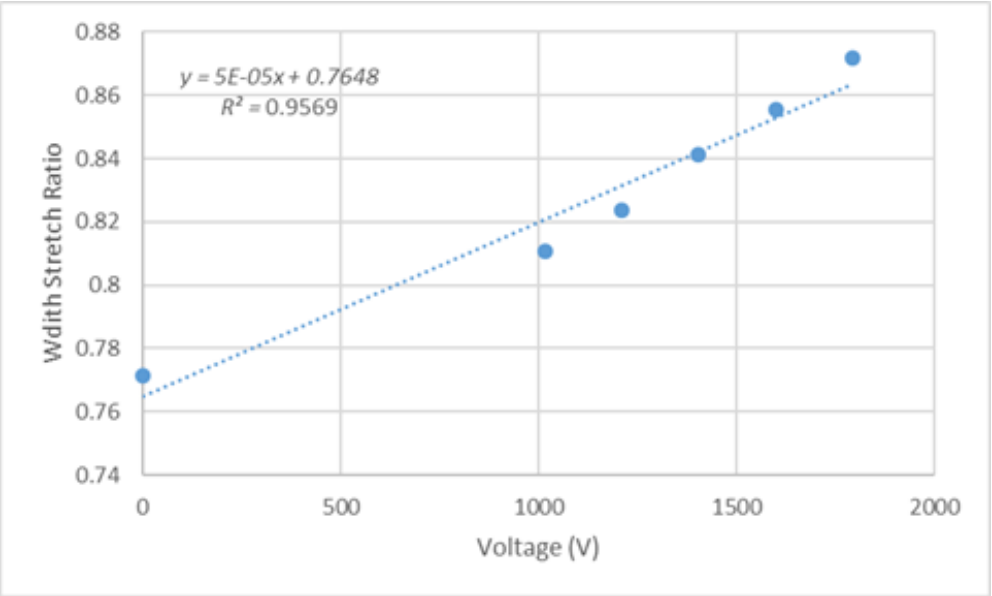

Figure 4.19: Voltage vs. the stretch ratio in the width direction with a 65 g weight for DEA 9. The equation is used when relating λ_1 with λ_2.

the film to tear across it. Dielectric breakdown being the most likely cause of failure for the DEAs was one of the reasons that the maximum voltage applied during the experiment was reduced from 2200 V to 2000 V.

The other reason that the max voltage was reduced to 2000 V was because there was wrinkling in the film at 2200 V as shown in Figure 4.22. When a DEA is actuated, the Maxwell stress reduces the tension in the width direction. Once the force from the Maxwell stress overcomes the tension in the film, it causes it to wrinkle, which can lead to failure. One possible improvement for future DEAs would be to find a way to keep the sides of the films held stretched out at a fixed width. This would increase the amount of voltage applied before wrinkling occurs, and it would also simplify modeling of the DEA if the width was kept constant.

The DEAs that performed as required behaved similarly during actuation, as shown in Figures 4.14–4.17. Based on these results, it is now possible to compare the performance of the DEAs to that of the DC motors for a wrist rehabilitation exoskeleton based on the force and stroke of the actuators.

The DEAs only actuated with a load of up to 0.931 N, because the DEA was stretched all the way across the arm at higher loads. The dielectric films has a tensile strength of 6 MPa and the

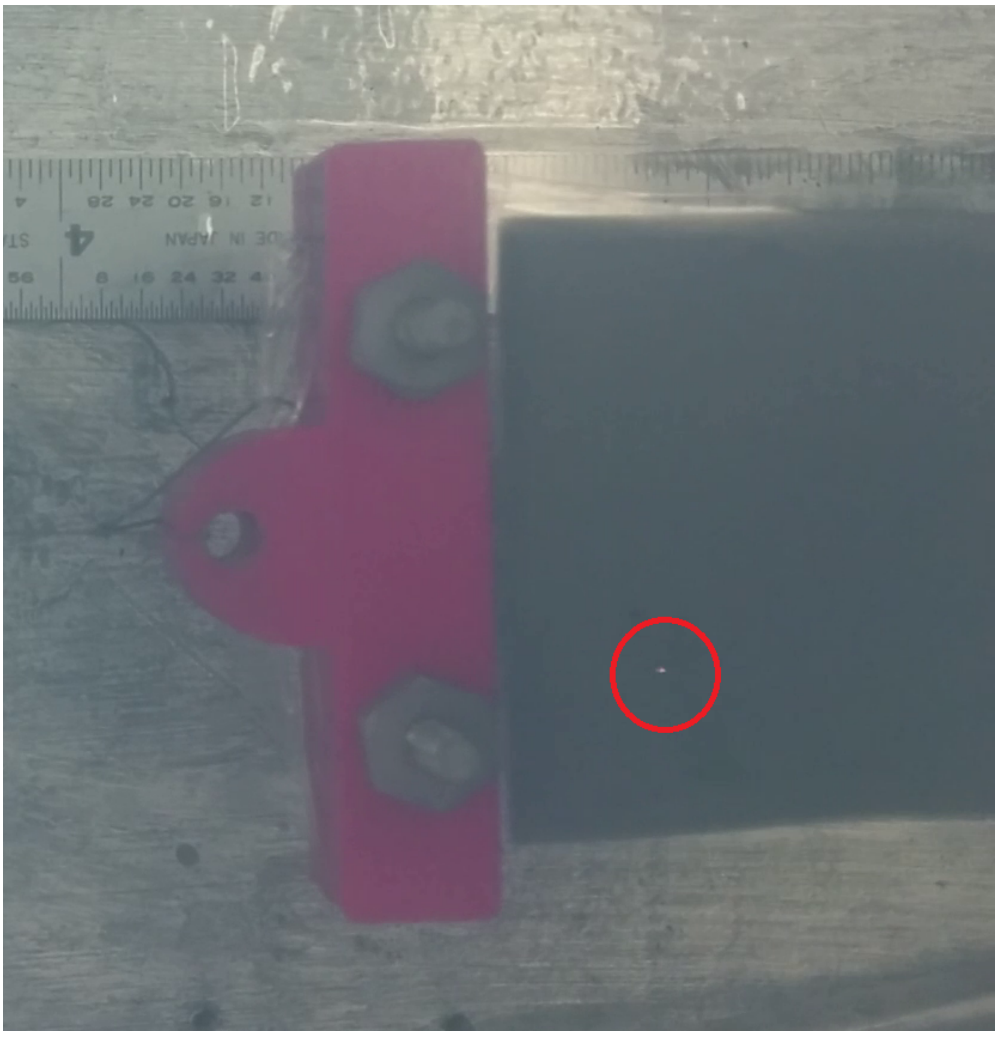

Figure 4.20: Dielectric breakdown of DEA #10. The red circle shows the point of electric breakdown while it is occurring.

highest stress recorded in the film was 1.066 MPa in DEA #11 at 2000 V, so in theory it should still be capable of applying higher loads. If the DEA is attached to the hand in the same way the DC motors are attached in Chapter 3, they would need to provide 9.7 N of force. This means that at least 11 DEAs would need to be layered in order to provide the required force, assuming that attaching the DEAs in parallel increases the force linearly.

The stroke of the DEA was measured by the strain in the DEA and ranged from 6.01–13.73% increase in strain during actuation. The highest increase in strain was from DEA #6, which was equal to a stroke of 17.93 mm. If the DEA were attached to the hand in the same way that the DC motor was attached in Chapter 3, this would result in a range of 45° for flexion–extension.

Figure 4.21: Result of dielectric breakdown in a DEA. The red circle shows the damage from dielectric breakdown.

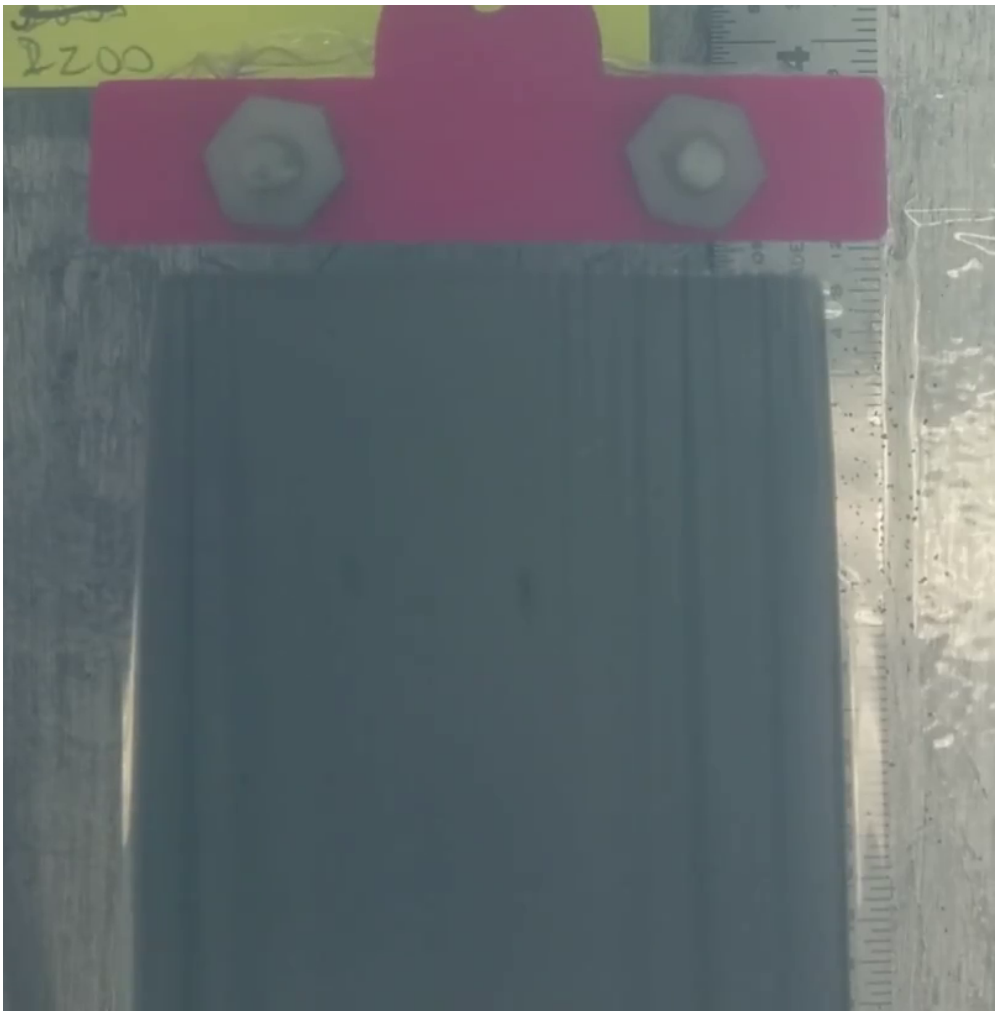

Figure 4.22: Loss of tension in the DEA.

The range of the motion of the motors in Chapter 3 was only 90° for flexion–extension but that was due to the test setup, not due to the motors.

An advantage that the DEAs have over the DC motor is that the DC motor has a mass of 185 g, and one DEA has a mass of 20.86 g, but the film and electrode only account for 0.1 g. Increasing the number of layers of the film and electrode can be done with the mass of the system only increasing a small amount.

One DEA, as designed in this chapter, is not capable of providing the force and range of motion for a wrist rehabilitation exoskeleton, but increasing the number of DEAs might be able to achieve the required force and range of motion. The DEAs may be capable of actuating joints with smaller requirements, such as the fingers, or those that allow a larger DEA surface area, such as a posture

correction device placed on the back of the user. It is also likely that the actuation performance of the DEAs could be improved by adjusting the configuration of the DEA, or using a different dielectric film. For future optimization of DEA design, it was desired to obtain a mathematical relationship between the variables involved in actuation. This characterization is presented in the following section.

4.6 DEA Characterization

Working from the data gathered in Section 4.5, it was possible to model the actuation of the DEAs using the equations described in Section 4.1. A third order Ogden model was chosen to describe the strain energy density because the material parameters can be determined from just experimental data and is a commonly used model for DEAs [65]. Equation 4.15 is used for describing the electromechanical model of the DEAs, where

$$\sigma_3 = 0, \tag{4.16}$$

$$\sigma_2 = \frac{P_2}{w_1 t_1}, \tag{4.17}$$

and Equations 4.7, 4.8, and 4.10 can be subbed into equation 4.17 to get

$$\sigma_2 = \frac{\lambda_2 P_2}{w_0 t_0}. \tag{4.18}$$

$$\frac{\partial W_s}{\partial \lambda_2} = \sum_{i=1}^{3} \frac{\mu_i}{\alpha_i}(\alpha_i \lambda_2^{\alpha_i - 1} - \frac{\alpha_i}{\lambda_1 \lambda_2^2 (\lambda_1 \lambda_2)^{\alpha_i - 1}}) \tag{4.19}$$

$$\frac{\lambda_2 P_2}{w_0 t_0} + \beta \eta \epsilon_0 \epsilon_r (\frac{\lambda_1 \lambda_2 V}{t_0})^2 = \frac{\lambda_2 \partial W_s(\lambda_1 \lambda_2)}{\partial \lambda_2}, \tag{4.20}$$

where β is the percentage of the area of the film that is covered by the electrode, and η is the efficiency of the actuator. Equation 4.15 assumes that the electrode is covering the total area of the film, whereas the DEAs developed in this chapter only have the electrode covering 79% of the film's area. The difference is significant enough that it needs to be included in the model. When

deriving Equation 4.15, the length and width of the electrode is implemented as a percentage of the length and width of the film. This results in the Maxwell stress term in Equation 4.15 changing linearly with the percentage of the area of the film covered in the electrode.

The actuator was only found to have an efficiency of approximately 70%, therefore it is included in the model shown by the variable η. The efficiency was determined using the equation:

$$\eta = \frac{w_m}{w_e} \tag{4.21}$$

where w_m is the generated mechanical work per unit of volume, and w_e is the electric charging work per unit of volume. The mechanical work per unit of volume is solved by the equation:

$$w_m = \frac{\int_{x_0}^{x_1} P_2 dx}{l_0 w_0 t_0} \tag{4.22}$$

where x_0 is the length of the DEA before voltage is applied and x_1 is the length of the DEA when voltage is applied to the DEA. The electric charging work per unit of volume is described by the equation:

$$w_e = \frac{1}{2}\frac{C}{A_e}\frac{V^2}{t_0} \tag{4.23}$$

where C is the capacitance of the DEA, and A_e is the area of the electrode [61]. Using the above equations with values recorded from the experiment, the efficiency of the DEA was determined to be approximately 70%.

To implement Equation 4.20, the material parameters μ_1, μ_2, μ_3, α_1, α_2, and α_3 needed to be determined. This was done using the `fmincon` function in MATLAB with the stress, strain, and voltage values from DEA #11, because it had data from a wider range of weights. The function uses Equation 4.20 with the strain and voltage from the DEA #11 experiment to solve for the stress in the P_2 direction of the film and finds the material parameters that produce the smallest error between the calculated stress and the measured stress. Running the `fmincon` function in MATLAB gave the material parameters in Table 4.9. These material parameters gave a RMS error of 9.88 kPa, which is 2.93% of the minimum stress experienced by DEA #11. The strain vs. voltage calculated from the model was plotted together with the strain vs. voltage data points

Material Parameters	Value
μ_1	61.36 kPa
μ_2	1.20 MPa
μ_3	1.20 MPa
α_1	3.312
α_2	0.2682
α_3	-0.1631
η	70 %

Table 4.9: Ogden material parameters and determined from the mathematical optimization and efficiency of the actuator.

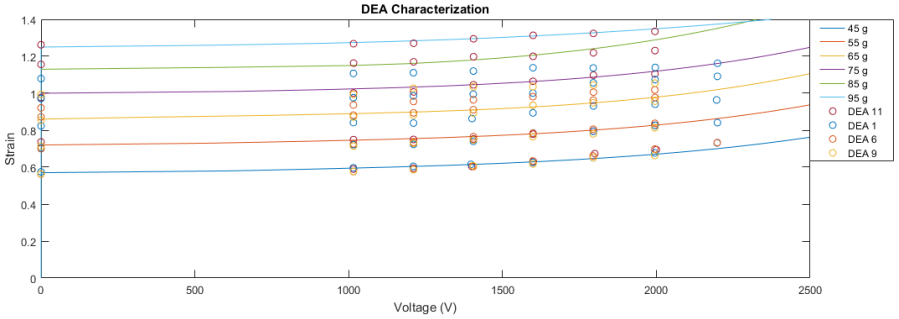

Figure 4.23: Strain vs. voltage that resulted from the Ogden model (solid lines) and the recorded data points (circles) from DEAs #1, #6, #9, and #11.

that were recorded from the working DEAs, as shown in Figure 4.23. The model using the parameters in Table 4.9 works well for describing DEA #11 for all the masses. The other 3 DEAs are close to the model for the lower masses but show an increase in error as the mass increases. This indicates that each DEA may need to be calibrated when first developed, but that the Ogden model, and the method outlined above, provides a solid foundation for this calibration to take place.

4.7 Conclusion

Chapter 4 showed the fabrication, testing, modeling, and analysis of dielectric elastomer actuators for a wearable wrist rehabilitation exoskeleton. The DEAs that were created were only tested with a hanging mass of up to 95 g, which equates to a force of 0.932 N. Based on the results from the experiment in Section 4.5, one DEA, as designed in this chapter, is not fully capable of providing

actuation for a wrist rehabilitation exoskeleton. The mass of 1 DEA is 20.9 g, but nearly all the mass is due to the parts used to attach it to the arm. The force can be increased by adding additional layers of the silicone film and electrode with only a small increase to the mass of the actuator. For future analysis, the characterization process for DEAs was developed and presented herein. This will allow optimizing the design of future DEAs for other applications.

Chapter 5

Conclusions and Future Work

The work presented in this thesis was aimed at comparing the performance between DC motors and dielectric actuators for actuating a wearable wrist exoskeleton for rehabilitation. A literature review was performed to show that the state of the art wrist rehabilitation exoskeletons are too heavy and too bulky to be portable. Nearly all of the devices that have been presented in the literature use DC motors for actuation, which do not have a high power to weight ratio. Smart material actuators—more specifically DEAs— are a possible alternative to DC motors for actuation in a wearable wrist exoskeleton, in order to reduce weight and size.

A simple model of the forearm, wrist, and hand was designed to be used for testing DC motors and DEAs. DC motors were tested with the arm for assisting with wrist flexion–extension and ulnar–radial deviation. The kinematics and dynamics for the arm, which included elbow flexion–extension, forearm pronation–supination, wrist flexion–extension, and wrist ulnar–radial deviation, were found. Using the kinematics and dynamics of the arm, an inverse dynamics controller was designed. A sensing system using two 9 DOF IMUs was developed to be used with the DC motors. The accuracy of the IMUs was tested using the Aurora electromagnetic tracking system. The sensing system had an average RMS error of 2.23° for the pitch of the wrist, 3.99° for the yaw of the wrist, and 2.90° for the pronation–supination of the arm. The motor setup was tested with two differently weighted hands by having it control flexion–extension by itself, ulnar–radial deviation by itself, flexion–extension with manual forearm pronation–supination movement, ulnar–radial deviation with manual forearm pronation–supination movement, flexion–

extension and ulnar–radial deviation together, and flexion–extension with ulnar–radial deviation during manual forearm pronation–supination. The average RMS error for flexion–extension in all motions ranged from 1.06° to 1.81° and the average RMS error for ulnar–radial deviation ranged from 0.83° to 2.10°.

Dielectric elastomer actuators were then designed to determine if these would be a suitable actuator for a wearable wrist exoskeleton. A conductive ink electrode was created and was sprayed onto a dielectric film with an air brush to build the DEA. The DEAs were tested on the model arm, with a weight hanging over the edge of the arm, to determine the capabilities of the actuator. Four out of the 12 DEAs were able to perform as required. The remaining 8 DEAs failed during testing with the 45 g weight. The largest increase in strain was 13% from DEA #6 and DEA #11 at 2000 V. The DEAs were tested with a load up to 0.931 N, because the DEA was stretched too far across the arm at higher loads to continue testing. The highest stress in the film was 1.066 MPa and the film has a tensile strength of 6 MPa so theoretically it should be capable of higher loads. Using the data from the experiment, an electromechanical model was developed for the DEAs and was optimized for DEA #11. The model fit the data from DEA #11 but did not fit as well to the data from the other DEAs.

The DEAs developed in this thesis were not capable of providing the force and range of motion required for a wearable wrist exoskeleton, whereas the DC motors were able to actuate the wrist joints with an inverse dynamics controller. There is still room for improvement with DEAs and while the DEAs were not successful in this thesis, better configurations for DEAs or other areas of rehabilitation can still be considered.

5.1 Contributions

The contributions of the work presented in this thesis can be summarized as follows:

1. The kinematic model and dynamic model of the arm from the elbow joint to the wrist joint were created. The models were found to be accurate by successfully using the models in an inverse dynamics controller that actuated the wrist joint. The controller was used with DC motors being attached to the arm to mimic an exoskeleton on the arm. The system was

commanded to track a sinusoidal input for flexion–extension by itself, ulnar–radial deviation by itself, flexion–extension with manual forearm pronation–supination movement, ulnar–radial deviation with manual forearm pronation–supination movement, flexion–extension and ulnar–radial deviation together, and flexion–extension with ulnar–radial deviation during manual forearm pronation–supination.

2. A sensing system using two IMUs was used to determine the positions of the four joints in the models. The system was first calibrated using the Aurora electromagnetic tracking system as a reference. Then the accuracy of this sensing system was measured by using the Aurora. The sensing system had an average RMS error of 2.23° for the pitch of the wrist, 3.99° for the yaw of the wrist, and 2.90° for the pronation–supination of the arm.

3. A method for fabricating the DEAs using a silicone film that was purchased, and a graphite mixture for the electrode was developed. The graphite mixture was based off of work done by Rosset *et al.* [83], but small modifications to the procedure. A mask and end pieces were designed in SolidWorks and 3D printed for holding the film stretched and covering the edges of the film while spraying the electrode mixture onto the film using an air brush.

4. Uniaxial actuation testing was performed with the DEAs to characterize the actuator. The results of the testing were then used to compare the DEAs with DC motors for use in a wearable wrist exoskeleton in order to determine what is needed in the future to develop a DEA-based exoskeleton.

5. An electromechanical model to relate the strain of the DEA with voltage was developed, and optimized to be used for DEA #11 and compared the model to the behavior of the other DEAs.

5.2 Future Work

While an initial comparison of DC motors with DEAs for actuating a wearable wrist exoskeleton showed that DEAs will not be able to provide the same force and range of motion that a motor

can, further work can still to be done to adapt DEA designs to rehabilitation exoskeletons. Some possible modifications are presented below.

1. The DEA design used for this thesis was a simple actuator configuration for DEAs. More complex configurations for DEAs such as the bow-tie configuration should be explored to try and improve the range of motion and/or the force. Designing a novel DEA configuration to be used for a wearable wrist exoskeleton could also be explored.

2. The model that was fitted to the recorded data needs to be improved. The testing only had the DEA stretch to the length of the arm but it can have higher strain. More testing with the DEAs should be done to get data at higher weights so the model can describe the DEA for a higher range of strains.

3. Although the DEAs did not meet the actuation requirements for a wearable wrist exoskeleton, there are other areas of rehabilitation that it may be suitable for. The DEAs might be better suited for a rehabilitation device that is assisting with a smaller body part such as the fingers, or they could be used for a back posture correction device because there is a larger area, which allows for more and larger DEAs.

4. If the DEAs do get used for a device on the body, some method for isolating the high voltage from the user will need to be found. Although the current used with the DEAs was very low, the high voltage could be dangerous and hurt patients if the device is not properly isolated. There should also be some research to determine if having a high voltage right next to the body for prolonged periods would have negative effects on the body.

The purpose of this thesis was to determine another actuator to be used for a wearable wrist exoskeleton that would reduce the size and weight of the device. This was accomplished by first evaluating DC motors for a wrist rehabilitation exoskeleton to determine what is required from DEAs. DEAs were then developed and tested to characterize the DEA, and an electromechanical model was fitted to the results. Continued work in this direction could lead to lighter exoskeletons for the wrist, and possibly for exoskeletons actuating other joints.

References

[1] D. C. Boone and S. P. Azen, "Normal range of motion of joints in male subjects.," *The Journal of bone and joint surgery. American volume*, vol. 61, pp. 756–759, 1979.

[2] J. T. McConville, C. E. Clauser, T. D. Churchill, J. Cuzzi, and I. Kaleps, "Anthropometric relationships of body and body segment moments of inertia," tech. rep., ANTHROPOLOGY RESEARCH PROJECT INC YELLOW SPRINGS OH, 1980.

[3] A. S. Book, "Vol. 1: Anthropometry for designers," *NASA Reference Publication*, vol. 1024, 1978.

[4] D. Mozaffarian *et al.*, *Heart Disease and Stroke Statistics–2015 Update: A Report From the American Heart Association*, vol. 131. 2014. Available from: `http://circ.ahajournals.org/cgi/doi/10.1161/CIR.0000000000000152`.

[5] H. Krueger, J. Koot, R. E. Hall, C. O'Callaghan, M. Bayley, and D. Corbett, "Prevalence of Individuals Experiencing the Effects of Stroke in Canada: Trends and Projections," *Stroke; a journal of cerebral circulation*, vol. 46, no. 8, pp. 2226–2231, 2015.

[6] M. Babaiasl, S. H. Mahdioun, P. Jaryani, and M. Yazdani, "A review of technological and clinical aspects of robot-aided rehabilitation of upper-extremity after stroke," *Disability and Rehabilitation: Assistive Technology*, vol. 00, no. 00, pp. 1–18, 2015. Available from: `http://dx.doi.org/10.3109/17483107.2014.1002539`.

[7] M. E. Sandel, "Stroke, disability, and unconscious bias: interrelationships and overdetermination in medical decisions.," *Topics in stroke rehabilitation*, vol. 18, no. 1, pp. 70–73, 1994.

[8] A. U. Pehlivan, S. Lee, and M. K. O'Malley, "Mechanical design of RiceWrist-S: A forearm-wrist exoskeleton for stroke and spinal cord injury rehabilitation," *Proceedings of the IEEE RAS and EMBS International Conference on Biomedical Robotics and Biomechatronics*, pp. 1573–1578, 2012. Available from: `http://ieeexplore.ieee.org/xpls/abs{\_}all.jsp?arnumber=6290912`.

[9] P. Maciejasz, J. Eschweiler, K. Gerlach-Hahn, A. Jansen-Troy, and S. Leonhardt, "A survey on robotic devices for upper limb rehabilitation.," *Journal of neuroengineering and rehabilitation*, vol. 11, p. 3, 2014. Available from: `http://www.jneuroengrehab.com/content/11/1/3`.

[10] J. Patton, "Efforts of Engineers," vol. 15, no. 6, pp. 521–541, 2009.

[11] W. H. Chang and Y.-H. Kim, "Robot-Assisted Therapy in Stroke Rehabilitation.," *Journal of stroke*, vol. 15, no. 3, pp. 174–81, 2013.

[12] M. Pekna, M. Pekny, and M. Nilsson, "Modulation of neural plasticity as a basis for stroke rehabilitation," *Stroke*, vol. 43, no. 10, pp. 2819–2828, 2012.

[13] G. E. Gresham, W. B. Stason, and P. W. Duncan, *Post-stroke rehabilitation*, vol. 95. Diane Publishing, 1997.

[14] J. H. Cauraugh and J. J. Summers, "Neural plasticity and bilateral movements: A rehabilitation approach for chronic stroke.," *Progress in neurobiology*, vol. 75, pp. 309–20, apr 2005. Available from: `http://www.sciencedirect.com/science/article/pii/S0301008205000341`.

[15] E. Lundström, A. Terént, and J. Borg, "Prevalence of disabling spasticity 1 year after first-ever stroke," *European Journal of Neurology*, vol. 15, no. 6, pp. 533–539, 2008.

[16] M. A. Dimyan and L. G. Cohen, "HHS Public Access," vol. 7, no. 2, pp. 76–85, 2016.

[17] P. W. Duncan, R. Zorowitz, B. Bates, J. Y. Choi, J. J. Glasberg, G. D. Graham, R. C. Katz, K. Lamberty, and D. Reker, *Management of Adult Stroke Rehabilitation Care: a clinical practice guideline.*, vol. 36. 2005.

[18] H. Feys, W. De Weerdt, G. Verbeke, G. C. Steck, C. Capiau, C. Kiekens, E. Dejaeger, G. Van Hoydonck, G. Vermeersch, and P. Cras, "Early and Repetitive Stimulation of the Arm Can Substantially Improve the Long-Term Outcome after Stroke: A 5-Year Follow-up Study of a Randomized Trial," *Stroke*, vol. 35, no. 4, pp. 924–929, 2004.

[19] B. H. Dobkin, "Strategies for stroke rehabilitation," *Lancet Neurology*, vol. 3, no. 9, pp. 528–536, 2004.

[20] G. Kwakkel, R. Van Peppen, R. C. Wagenaar, S. W. Dauphinee, C. Richards, A. Ashburn, K. Miller, N. Lincoln, C. Partridge, I. Wellwood, and P. Langhorne, "Effects of augmented exercise therapy time after stroke: A meta-analysis," *Stroke*, vol. 35, no. 11, pp. 2529–2536, 2004.

[21] S. Lindsay, M.P., Gubitz, G., Bayley, M., and Phillips, "Summary of Stroke Best Practice Recommendations," *Canadian Best Practice Recommendations for Stroke Care*, vol. 4, pp. 1–81, 2013.

[22] R. Hall and F. Khan, "Stroke Report Cards and Progress Reports: Setting the Bar Higher," Tech. Rep. June, INSTITUTE FOR CLINICAL EVALUATIVE SCIENCES, Toronto, 2017.

[23] G. Andrikopoulos, G. Nikolakopoulos, and S. Manesis, "Design and development of an exoskeletal wrist prototype via pneumatic artificial muscles," *Meccanica*, vol. 50, no. 11, pp. 2709–2730, 2015.

[24] J. H. Beekhuis, A. J. Westerveld, H. Van Der Kooij, and A. H. a. Stienen, "Design of a self-aligning 3-DOF actuated exoskeleton for diagnosis and training of wrist and forearm after stroke," *IEEE International Conference on Rehabilitation Robotics*, 2013.

[25] B.-C. Tsai, W.-W. Wang, L.-C. Hsu, L.-C. Fu, and J.-S. Lai, "An articulated rehabilitation robot for upper limb physiotherapy and training," in *Intelligent Robots and Systems (IROS), 2010 IEEE/RSJ International Conference on*, pp. 1470–1475, IEEE, 2010.

[26] T. G. Sugar, J. He, E. J. Koeneman, J. B. Koeneman, R. Herman, H. Huang, R. S. Schultz, D. E. Herring, J. Wanberg, S. Balasubramanian, P. Swenson, and J. a. Ward, "Design and control of RUPERT: A device for robotic upper extremity repetitive therapy," *IEEE Transactions on Neural Systems and Rehabilitation Engineering*, vol. 15, no. 1, pp. 336–346, 2007.

[27] J. A. Martinez, P. Ng, S. Lu, M. S. Campagna, and O. Celik, "Design of wrist gimbal: A forearm and wrist exoskeleton for stroke rehabilitation," in *Rehabilitation Robotics (ICORR), 2013 IEEE International Conference on*, pp. 1–6, IEEE, 2013.

[28] T. Noda, T. Teramae, B. Ugurlu, and J. Morimoto, "Development of an Upper Limb Exoskeleton Powered via Pneumatic Electric Hybrid Actuators with Bowden Cable," no. Iros, pp. 3573–3578, 2014.

[29] A. U. Pehlivan, F. Sergi, and M. K. OMalley, "A Subject-Adaptive Controller for Wrist Robotic Rehabilitation," 2014.

[30] A. U. Pehlivan, F. Sergi, A. Erwin, N. Yozbatiran, G. Francisco, and M. K. O'Malley, "Design and validation of the RiceWrist-S exoskeleton for robotic rehabilitation after incomplete spinal cord injury," *Robotica*, no. 2014, pp. 1415–1431, 2014.

[31] H. S. Lo and S. Q. Xie, "Exoskeleton robots for upper-limb rehabilitation: State of the art and future prospects," *Medical Engineering and Physics*, vol. 34, no. 3, pp. 261–268, 2012. Available from: `http://dx.doi.org/10.1016/j.medengphy.2011.10.004`.

[32] J. Rosen, M. B. Fuchs, and M. Arcan, "Performances of hill-type and neural network muscle modelstoward a myosignal-based exoskeleton," *Computers and Biomedical Research*, vol. 32, no. 5, pp. 415–439, 1999.

[33] X. Cui, W. Chen, S. K. Agrawa, and J. Wang, "A novel customized cable-driven robot for 3-dof wrist and forearm motion training," in *Intelligent Robots and Systems (IROS 2014), 2014 IEEE/RSJ International Conference on*, pp. 3579–3584, IEEE, 2014.

[34] R. Gopura and K. Kiguchi, "Development of an exoskeleton robot for human wrist and forearm motion assist," in *Industrial and Information Systems, 2007. ICIIS 2007. International Conference on*, pp. 535–540, IEEE, 2007.

[35] H. M. Kim, T. Hong, and G. Kim, "Design of a wrist rotation rehabilitation robot," in *Cyber Technology in Automation, Control, and Intelligent Systems (CYBER), 2014 IEEE 4th Annual International Conference on*, pp. 240–245, IEEE, 2014.

[36] M. H. Rahman, M. Rahman, O. L. Cristobal, M. Saad, J.-P. Kenné, and P. S. Archambault, "Development of a whole arm wearable robotic exoskeleton for rehabilitation and to assist upper limb movements," *Robotica*, vol. 33, no. 01, pp. 19–39, 2015.

[37] I. Yamamoto, N. Inagawa, K. Hachisuka, F. Oda, and Y. Nakanishi, "Development of compact rehabilitation robot for a wrist using biological signal," in *Complex Medical Engineering (CME), 2012 ICME International Conference on*, pp. 557–560, IEEE, 2012.

[38] A. U. Pehlivan, F. Sergi, and M. K. OMalley, "A Subject-Adaptive Controller for Wrist Robotic Rehabilitation," 2014.

[39] S. Pittaccio, L. Garavaglia, S. Viscuso, E. Beretta, and S. Strazzer, "Implementation, testing and pilot clinical evaluation of superelastic splints that decrease joint stiffness," *Annals of Biomedical Engineering*, vol. 41, no. 9, pp. 2003–2017, 2013. Available from: `http://www.ncbi.nlm.nih.gov/pubmed/23793385`.

[40] F. Carpi, G. Frediani, C. A. Gerboni, J. Gemignani, and D. D. Rossi, "Towards variable stifness dynamic hand splints based on dielecric elastomer transducers," no. June, pp. 258749–258749, 2011.

[41] F. Carpi, G. Frediani, C. Gerboni, J. Gemignani, and D. De Rossi, "Enabling variable-stiffness hand rehabilitation orthoses with dielectric elastomer transducers," *Medical Engineering and Physics*, vol. 36, no. 2, pp. 205–211, 2014. Available from: `http://dx.doi.org/10.1016/j.medengphy.2013.10.015`.

[42] J. Nikitczuk, B. Weinberg, and C. Mavroidis, "Rehabilitative knee orthosis driven by electro-rheological fluid based actuators," *Proceedings - IEEE International Conference on Robotics and Automation*, vol. 2005, no. April, pp. 2283–2289, 2005.

[43] J. A. French, C. G. Rose, and M. K. OMalley, "System characterization of mahi exo-ii: A robotic exoskeleton for upper extremity rehabilitation," in *ASME 2014 Dynamic Systems and Control Conference*, pp. V003T43A006–V003T43A006, American Society of Mechanical Engineers, 2014.

[44] A. U. Pehlivan, O. Celik, and M. K. O'Malley, "Mechanical design of a distal arm exoskeleton for stroke and spinal cord injury rehabilitation," in *Rehabilitation Robotics (ICORR), 2011 IEEE International Conference on*, pp. 1–5, IEEE, 2011.

[45] J. Hope and A. McDaid, "Development of Wearable Wrist and Forearm Exoskeleton with Shape Memory Alloy Actuators," *Journal of Intelligent and Robotic Systems: Theory and Applications*, vol. 86, no. 3-4, pp. 397–417, 2017.

[46] K. Park, H. S. Park, S. H. Yoon, B. J. Dan, B. R. Jo, and W. S. Chang, "Development of 2-DOF robotic exoskeleton for upper limb rehabilitation after stroke," *Proceedings - IEEE International Workshop on Robot and Human Interactive Communication*, pp. 366–367, 2013.

[47] K. K. Xiang, P. C. J. Hua, H. A. Rahman, Y. C. Fai, A. L. T. Narayanan, and E. S. L. Ming, "Development of reconfigurable rehabilitation robot for post-stroke forearm and wrist training," *Jurnal Teknologi*, vol. 72, no. 2, 2015.

[48] P. Brochu and Q. Pei, "Advances in dielectric elastomers for actuators and artificial muscles," *Macromolecular Rapid Communications*, vol. 31, no. 1, pp. 10–36, 2010.

[49] F. Carpi, R. Kornbluh, P. Sommer-Larsen, and G. Alici, "Electroactive polymer actuators as artificial muscles: are they ready for bioinspired applications?," *Bioinspiration & Biomimetics*, vol. 6, no. 4, p. 045006, 2011.

[50] K. Jung, K. J. Kim, and H. R. Choi, "A self-sensing dielectric elastomer actuator," *Sensors and Actuators A: Physical*, vol. 143, no. 2, pp. 343–351, 2008. Available from: `http://linkinghub.elsevier.com/retrieve/pii/S092442470700814X`.

[51] K. J. Kim and S. Tadokoro, "Electroactive polymers for robotic applications," *Artificial Muscles and Sensors (291 p.), Springer: London, United Kingdom*, 2007.

[52] J. D. Madden, N. A. Vandesteeg, P. A. Anquetil, P. G. Madden, A. Takshi, R. Z. Pytel, S. R. Lafontaine, P. A. Wieringa, and I. W. Hunter, "Artificial muscle technology: physical principles and naval prospects," *Oceanic Engineering, IEEE Journal of*, vol. 29, no. 3, pp. 706–728, 2004.

[53] P. Lochmatter, G. Kovacs, P. Ermanni, and E. Mazza, "Development of a shell-like electro active polymer (EAP) actuator," *EMPA Activities*, no. 2007, p. 30, 2007.

[54] D. Tepel, C. Graf, and J. Maas, "Modeling of mechanical properties of stack actuators based on electroactive polymers," *Proc. SPIE 8687*, vol. 8687, p. 86871C, 2013. Available from: `http://proceedings.spiedigitallibrary.org/proceeding.aspx?doi=10.1117/12.2010104`.

[55] F. Carpi, C. Salaris, and D. Rossi, "Folded dielectric elastomer actuators," *Smart Materials and Structures*, vol. 16, no. 2, pp. S300–S305, 2007. Available from: `http://www.iop.org/EJ/article/0964-1726/16/2/S15/sms7{\_}2{\_}S15.pdf`.

[56] J. S. Plante and S. Dubowsky, "Large-scale failure modes of dielectric elastomer actuators," *International Journal of Solids and Structures*, vol. 43, no. 25-26, pp. 7727–7751, 2006.

[57] M. Awadalla and B. Anees, "Developing Spring-Roll Dielectric Elastomer Actuator System Based on Optimal Design Parameters," vol. 8, no. 5, pp. 46–56, 2011.

[58] G.-k. Lau, H.-t. Lim, J.-Y. Teo, and Y.-w. Chin, "Lightweight mechanical amplifiers for rolled dielectric elastomer actuators and their integration with bio-inspired wing flappers," *Smart Materials and Structures*, vol. 23, p. 025021, 2014. Available from: `http://iopscience.iop.org/0964-1726/23/2/025021/article/`.

[59] R. E. Pelrine, R. D. Kornbluh, and J. P. Joseph, "Electrostriction of polymer dielectrics with compliant electrodes as a means of actuation," *Sensors and Actuators A: Physical*, vol. 64, no. 1, pp. 77–85, 1998.

[60] M. Henke and G. Gerlach, "On the development of planar actuators for variable stiffness devices," *Proc. SPIE 8687, Smart Structures and Materials 2013: Electroactive Polymer Actuators and Devices (EAPAD)*, vol. 8687, pp. 868727–1 to 868727–14, 2013. Available from: `http://proceedings.spiedigitallibrary.org/proceeding.aspx?doi=10.1117/12.2010668`.

[61] F. Carpi, P. Chiarelli, A. Mazzoldi, and D. De Rossi, "Electromechanical characterisation of dielectric elastomer planar actuators: Comparative evaluation of different electrode materials and different counterloads," *Sensors and Actuators, A: Physical*, vol. 107, no. 1, pp. 85–95, 2003.

[62] J. Shintake, "Functional Soft Robotic Actuators Based on Dielectric Elastomers," vol. 6855, p. 149, 2016.

[63] R. Kornbluh, R. Pelrine, Q. Pei, R. Heydt, S. Stanford, S. Oh, and J. Eckerle, "Electroelastomers: Applications of dielectric elastomer transducers for actuation, generation, and smart structures," *Proceeding of SPIE Vol. 4698*, vol. 4698, pp. 254–270, 2002. Available from: `http://spiedigitallibrary.org/proceeding.aspx?articleid=883273`.

[64] P. Lotz, M. Matysek, and H. F. Schlaak, "Fabrication and application of miniaturized dielectric elastomer stack actuators," *IEEE/ASME Transactions on Mechatronics*, vol. 16, no. 1, pp. 58–66, 2011.

[65] G.-Y. Gu, J. Zhu, L.-M. Zhu, and X. Zhu, "A survey on dielectric elastomer actuators for soft robots," *Bioinspiration & Biomimetics*, vol. 12, no. 1, p. 011003, 2017.

[66] C. E. Clauser, "Weight, Volume, and Center of Mass of Segements of Human Body," *National Technical Information Service*, 1969.

[67] J. Denavit and R. Hartenberg, "A kinematic notation for lower-pair mechanisms based on matrices," *ASME J. Applied Mechanics*, vol. 2, pp. 215–221, 1955.

[68] M. W. Spong, *Robot Dynamics and Control*. New York, NY, USA: John Wiley & Sons, Inc., 1st ed., 1989.

[69] S. O. H. Madgwick, A. J. L. Harrison, and R. Vaidyanathan, "Estimation of IMU and MARG orientation using a gradient descent algorithm," *IEEE International Conference on Rehabilitation Robotics*, 2011.

[70] S. O. H. Madgwick, A. J. L. Harrison, and R. Vaidyanathan, "Estimation of IMU and MARG orientation using a gradient descent algorithm," *IEEE International Conference on Rehabilitation Robotics*, p. 32, 2011. Available from: `http://sharenet-wii-motion-trac.googlecode.com/files/An{\_}efficient{\_}orientation{\_}filter{\_}for{\_}inertial{\_}and{\_}inertialmagnetic{\_}sensor{\_}arrays.pdf`.

[71] R. Pelrine, P. Sommer-Larsen, R. D. Kornbluh, R. Heydt, G. Kofod, Q. Pei, and P. Gravesen, "Applications of Dielectric Elastomer Actuators," *Proc. SPIE 4329, Smart Structures and Materials 2001: Electroactive Polymer Actuators and Devices,*, vol. 4329, pp. 335–349, 2001. Available from: `http://proceedings.spiedigitallibrary.org/proceeding.aspx?articleid=1279395`.

[72] R. Pelrine, R. Kornbluh, Q. Pei, and J. Joseph, "High-speed electrically actuated elastomers with strain greater than 100%," *Science*, vol. 287, no. 5454, pp. 836–839, 2000.

[73] O. Yeoh, "Characterization of elastic properties of carbon-black-filled rubber vulcanizates," *Rubber chemistry and technology*, vol. 63, no. 5, pp. 792–805, 1990.

[74] R. W. Ogden, "Large deformation isotropic elasticity-on the correlation of theory and experiment for incompressible rubberlike solids," in *Proceedings of the Royal Society of London A: Mathematical, Physical and Engineering Sciences*, vol. 326, pp. 565–584, The Royal Society, 1972.

[75] L. R. G. Treloar, *The physics of rubber elasticity*. Oxford University Press, USA, 1975.

[76] Z. Suo, "Theory of dielectric elastomers," *Acta Mechanica Solida Sinica*, vol. 23, no. 6, pp. 549–578, 2010. Available from: http://dx.doi.org/10.1016/S0894-9166(11)60004-9.

[77] A. Ali, M. H. Fouladi, and B. Sahari, "A Review of Constitutive Models for Rubber-Like Materials," *American Journal of Engineering and Applied Sciences*, vol. 3, no. 1, pp. 232–239, 2010. Available from: http://psasir.upm.edu.my/11779/1/AReviewofConstitutiveModelsforRubber.pdf{\%}5Cnhttp://www.thescipub.com/abstract/10.3844/ajeassp.2010.232.239.

[78] M. Wissler and E. Mazza, "Modeling and simulation of dielectric elastomer actuators," *Smart Materials and Structures*, vol. 14, pp. 1396–1402, 2005.

[79] S. Rosset and H. R. Shea, "Flexible and stretchable electrodes for dielectric elastomer actuators," *Applied Physics A: Materials Science and Processing*, vol. 110, no. 2, pp. 281–307, 2013.

[80] S. Rosset and H. R. Shea, "Towards fast, reliable, and manufacturable DEAs: miniaturized motor and Rupert the rolling robot," *Electroactive Polymer Actuators and Devices (EAPAD)*, vol. 9430, p. 943009, 2015. Available from: http://proceedings.spiedigitallibrary.org/proceeding.aspx?doi=10.1117/12.2085279.

[81] G. Kofod, P. Sommer-Larsen, R. Kornbluh, and R. Pelrine, "Actuation Response of Polyacrylate Dielectric Elastomers," *Journal of Intelligent Materials Systems and Structures*, vol. 14, no. 12, pp. 787–793, 2003.

[82] I. a. Anderson, E. P. Calius, T. Gisby, T. Hale, T. McKay, B. O'Brien, and S. Walbran, "A dielectric elastomer actuator thin membrane rotary motor," *Electroactive Polymer Actuators and Devices (EAPAD)*, vol. 7287, no. 1, pp. 72871H–72871H–10, 2009. Available from: http://proceedings.spiedigitallibrary.org/proceeding.aspx?articleid=1337223.

[83] S. Rosset, O. a. Araromi, S. Schlatter, and H. R. Shea, "Fabrication Process of Silicone-based Dielectric Elastomer Actuators," *Journal of Visualized Experiments*, no. 108, pp. 1–13, 2016. Available from: http://www.jove.com/video/53423/fabrication-process-of-silicone-based-dielectric-elastomer-actuators.

[84] O. A. Araromi, I. Gavrilovich, J. Shintake, S. Rosset, M. Richard, V. Gass, and H. R. Shea, "Rollable multisegment dielectric elastomer minimum energy structures for a deployable microsatellite gripper," *IEEE/ASME Transactions on Mechatronics*, vol. 20, no. 1, pp. 438–446, 2015.

Appendix A

Code Used

A.1 Matlab

A.1.1 Kinematics and Dynamics of the Arm

MATLAB code to calculate the kinematics and dynamics of the arm

```
syms q1 q2 q3 q4 d cm md m I1xx I1yy I1zz I2xx I2yy I2zz dq1 dq2 dq3 dq4
%joint 1 is angle from elbow to wrist parallel to the ground. joint 2 is
%qd1 is derivative of q1
%
q1=pi/3; q2=2*pi/3; q3=pi/4; q4=1;
%q1=0; q2=pi/3; q3=0; q4=0;
dq1=0.2; dq2=-0.2; dq3=0.1; dq4=0.25;
dq=[dq1; dq2; dq3; dq4];
q=[q1;q2;q3;q4];


%the forearm rotation. joint 3 is wrist flexion extension. Joint 4 is wrist
%radial ulnar deviation
c1=cos(q1); c2=cos(q2); c3=cos(q3); c4=cos(q4);
s1=sin(q1); s2=sin(q2); s3=sin(q3); s4=sin(q4);

 d=0.3; cm=0.06; md=0.8; m=0.4;
g=9.81;
cm2=cm*cm;
%Iarm=[(1/3)*md*d^2 0 0; 0 (1/3)*md*d^2 0; 0 0 0.5*md*0.03^2]; %rough value
%Ihand=[0.002804064 0 0; 0 0.000142025 0; 0 0 0.002818129];
I1xx=(1/3)*md*d^2; I1yy=(1/3)*md*d^2; I1zz=0.5*md*0.03^2;
I2xx=0.002804064; I2yy=0.000142025; I2zz=0.002818129;
Iarm=diag([I1xx; I1yy; I1zz]);
Ihand=diag([I2xx; I2yy; I2zz]);



T01=transfrmmtx(0, 0, 90, q1);
T12=transfrmmtx(0, d, -90, q2);
T23=transfrmmtx(0, 0, 90, q3);
T34=transfrmmtx(cm, 0, 0, q4);

T02=T01*T12;
T03=T02*T23;
T04=T03*T34;
%T14=T12*T23*T34;



R1=T01(1:3,1:3);
R2=T02(1:3,1:3);
R3=T03(1:3,1:3);
R4=T04(1:3,1:3);

%R14=T14(1:3,1:3);

z0=[0;0;1];
z1=T01(1:3,3);
z2=T02(1:3,3);
z3=T03(1:3,3);
O0=[0;0;0];
O1=T01(1:3,4);
O2=T02(1:3,4);
O3=T03(1:3,4);
O4=T04(1:3,4);
```

```
%not needed right now
Jv1=cross(z0, O4);
Jv2=cross(z1, O4-O1);
Jv3=cross(z2, O4-O2);
Jv4=cross(z3,O4-O3);
Jv=[Jv1 Jv2 Jv3 Jv4];
Jw=[z0 z1 z2 z3];
JJ=[Jv; Jw];

%dynamics part
%Jvv1=0;
Jvv2=[cross(z0,O2)/2 cross(z1, O2)/2 [0;0;0] [0;0;0]]; %I divided the first
column by 2 so it would be the distance to center of mass
%Jvv3=[cross(z0, O3) cross(z1,O3) cross(z2,O3-O2) [0;0;0]];
Jvv4=[cross(z0, O4) cross(z1,O4-O1) cross(z2, O4-O2) cross(z3,O4-O3)]; %end
effector location is chosen at the center of mass of the hand

Kv=md*(Jvv2.'*Jvv2)+m*(Jvv4.'*Jvv4); %I'm assuming that m1 and m3 would be 0
because there is no link between 1 and 2, and 3 and 4


Jww1=[0 0 0 0; 0 0 0 0; 1 0 0 0];
Jww2=[z0 z1 [0;0;0] [0;0;0]];
Jww3=[z0 z1 z2 [0;0;0]];
Jww4=[z0 z1 z2 z3];

Kw=Jww2.'*R2*Iarm*R2.'*Jww2+Jww4.'*R4*Ihand*R4.'*Jww4; %no I for joints 1 and


M=Kw+Kv;


P2=md*g*0.5*d*s1;
% P4=m*g*(d*c1+cm*c4*(c1*sin(-q3+pi/2)-s1*c2*cos(-q3+pi/2))-cm*s1*s2*s4);
%P4=m*g*(d*sin(q1) + cm*cos(q4)*(sin(q1)*sin(q3) + cos(q1)*cos(q2)*cos(q3)) -
cm*cos(q1)*sin(q2)*sin(q4));
P4=m*g*(d*sin(q1) - cm*cos(q4)*(sin(q1)*sin(q3) - cos(q1)*cos(q2)*cos(q3)) -
cm*cos(q1)*sin(q2)*sin(q4));
P=P2+P4;
GG1=gradient(P,q1);
GG2=gradient(P,q2);
GG3=gradient(P,q3);
GG4=gradient(P,q4);
GG=[GG1; GG2; GG3; GG4];


D(1, 1, 1)=-2*d*d*m*c1*s1-
0.5*d*d*md*c1*s1+d*d*m*sin(2*q1)+0.25*d*d*md*sin(2*q1)-
2*cm2*m*c1*s1*s3*s3*c4*c4-
2*cm2*m*c1*s1*s2*s2*s4*s4+cm2*m*sin(2*q1)*s3*s3*c4*c4+cm2*m*sin(2*q1)*s2*s2*s
4*s4-2*cm2*m*c1*s1*c2*c2*c3*c3*c4*c4+cm2*m*sin(2*q1)*c2*c2*c3*c3*c3*c4*c4-
4*cm*d*m*c1*s1*s3*c4+2*cm*d*m*sin(2*q1)*s3*c4-
4*cm2*m*c1*s1*c2*s2*c3*c4*s4+2*cm2*m*sin(2*q1)*c2*s2*c3*c4*s4;
D(1, 1, 2)=-2*I1zz*c2*s2+I1xx*sin(2*q2)-2*I2yy*c2*s2*c4*c4-
2*I2xx*c2*s2*s4*s4+I2zz*sin(2*q2)*s3*s3+I2xx*sin(2*q2)*c3*c3*c4*c4+I2yy*sin(2
```

```
*q2)*c3*c3*s4*s4+cm2*m*c1*c1*sin(2*q2)*s4*s4+cm2*m*s1*s1*sin(2*q2)*s4*s4-
2*cm2*m*c1*c1*c2*s2*c3*c3*c4*c4-2*cm2*m*s1*s1*c2*s2*c3*c3*c4*c4-
2*I2xx*cos(2*q2)*c3*c4*s4+2*I2yy*cos(2*q2)*c3*c4*s4+2*cm2*m*c1*c1*cos(2*q2)*c
3*c4*s4+2*cm2*m*s1*s1*cos(2*q2)*c3*c4*s4;
D(1, 1, 3)=I2zz*s2*s2*sin(2*q3)-2*I2xx*s2*s2*c3*s3*c4*c4-
2*I2yy*s2*s2*s3*c3*s4*s4+cm2*m*c1*c1*sin(2*q3)*c4*c4+cm2*m*s1*s1*sin(2*q3)*c4
*c4-2*cm2*m*c1*c1*c2*c2*c3*s3*c4*c4-
2*cm2*m*s1*s1*c2*c2*c3*s3*c4*c4+2*cm*d*m*c1*c1*c3*c4+2*cm*d*m*s1*s1*c3*c4+2*I
2xx*c2*s2*s3*c4*s4-2*I2yy*c2*s2*s3*c4*s4-2*cm2*c1*c1*c2*s2*s3*c4*s4-
2*cm2*m*s1*s1*s2*c2*s3*s4*c4;
D(1, 1, 4)=-2*I2yy*c2*c2*c4*s4+I2xx*c2*c2*sin(2*q4)-
2*I2xx*s2*s2*c3*c3*c4*s4+I2yy*s2*s2*c3*c3*sin(2*q4)-
2*cm2*m*c1*c1*s3*s3*c4*s4+cm2*m*c1*c1*s2*s2*sin(2*q4)-
2*cm2*m*s1*s1*s3*s3*c4*s4+cm2*m*s1*s1*s2*s2*sin(2*q4)-
2*cm2*m*c1*c1*c2*c2*c3*c3*c4*s4-2*cm2*m*s1*s1*c2*c2*c3*c3*c4*s4-
2*cm*d*m*c1*c1*s3*s4-2*cm*d*m*s1*s1*s3*s4-
2*I2xx*c2*s2*c3*cos(2*q4)+2*I2yy*c2*s2*c3*cos(2*q4)+2*cm2*m*c1*c1*c2*s2*c3*co
s(2*q4)+2*cm2*m*s1*s1*c2*s2*c3*cos(2*q4);

D(1,2,1)=0;
D(1,2,2)=I2yy*c2*c3*s3-I2zz*c2*c3*s3+I2xx*s2*s3*s4*c4-I2yy*s2*s3*s4*c4-
cm*d*m*s2*s4+I2xx*c2*c3*s3*c4*c4-I2yy*c2*c3*s3*c4*c4-cm2*m*s2*s3*s4*c4-
cm*d*m*c2*c3*c4-cm2*m*c2*c3*s3*c4*c4;
D(1,2,3)=I2yy*s2*cos(2*q3)-I2zz*s2*cos(2*q3)-
I2xx*c2*c3*c4*s4+I2yy*c2*c3*c4*s4+I2xx*s2*cos(2*q3)*c4*c4-
I2yy*s2*cos(2*q3)*c4*c4+cm2*m*c2*c3*c4*s4+cm*d*m*s2*s3*c4-
cm2*m*s2*cos(2*q3)*c4*c4;
D(1,2,4)=-I2xx*c2*s3*cos(2*q4)+I2yy*c2*s3*cos(2*q4)+cm*d*m*c2*c4-
2*I2xx*s2*c3*s3*s4*c4+2*I2yy*s2*s3*c3*s4*c4+cm2*m*c2*s3*cos(2*q4)+cm*d*m*s2*c
3*s4+2*cm2*m*s2*s3*c3*c4*s4;

D(1,3,1)=0;
D(1,3,2)=-
I2xx*s2*c4*c4+I2xx*s2+I2yy*s2*c4*c4+cm2*m*s2*c4*c4+I2xx*c2*c3*c4*s4-
I2yy*c2*c3*c4*s4-cm2*m*c2*c3*c4*s4+cm*d*m*s2*s3*c4;
D(1,3,3)=-I2xx*s2*s3*s4*c4+I2yy*s2*s3*s4*c4+cm2*m*s2*s3*s4*c4-
cm*d*m*c2*c3*c4;
D(1,3,4)=-
2*I2xx*c2*c4*s4+2*I2yy*c2*c4*s4+2*cm2*m*c2*c4*s4+I2xx*s2*c3*cos(2*q4)-
I2yy*s2*c3*cos(2*q4)-cm2*m*s2*c3*cos(2*q4)+cm*d*m*c2*s3*s4;

D(1,4,1)=0;
D(1,4,2)=I2zz*c2*s3+cm2*m*c2*s3+cm*d*m*c2*c4+cm*d*m*s2*c3*s4;
D(1,4,3)=I2zz*s2*c3+cm2*m*s2*c3+cm*d*m*c2*s3*s4;
D(1,4,4)=-cm*d*m*s2*s4-cm*d*m*c2*c3*c4;

D(2,1,1)=0;
D(2,1,2)=-I2yy*c2*c3*s3-I2zz*c2*c3*s3+I2xx*s2*s3*s4*c4-I2yy*s2*s3*s4*c4-
cm*d*m*s2*s4+I2xx*c2*c3*s3*c4*c4-I2yy*c2*c3*s3*c4*c4-cm2*m*s2*s3*s4*c4-
cm*d*m*c2*c3*c4-cm2*m*c2*c3*s3*c4*c4;
D(2,1,3)=I2yy*s2*cos(2*q3)-I2zz*s2*cos(2*q3)-
I2xx*c2*c3*c4*s4+I2yy*c2*c3*c4*s4+I2xx*s2*cos(2*q3)*c4*c4-
I2yy*s2*cos(2*q3)*c4*c4+cm2*m*c2*c3*c4*s4+cm*d*m*s2*s3*c4-
cm2*m*s2*cos(2*q3)*c4*c4;
```

```
D(2,1,4)=-I2xx*c2*s3*cos(2*q4)+I2yy*c2*s3*cos(2*q4)+cm*d*m*c2*c4-
2*I2xx*s2*c3*s3*c4*s4+2*I2yy*s2*c3*s3*c4*s4+cm2*m*c2*s3*cos(2*q4)+cm*d*m*s2*c
3*s4+2*cm2*m*s2*s3*c3*s4*c4;

D(2,2,1)=0;
D(2,2,2)=0;
D(2,2,3)=0.5*I2xx*sin(2*q3)+0.5*I2yy*sin(2*q3)-I2zz*sin(2*q3)-
0.5*cm2*m*sin(2*q3)+0.5*I2xx*sin(2*q3)*cos(2*q4);
D(2,2,4)=-
0.5*I2xx*sin(2*q4)+0.5*I2yy*sin(2*q4)+0.5*cm2*m*sin(2*q4)+0.5*I2xx*cos(2*q3)*
sin(2*q4)-0.5*I2yy*cos(2*q3)*sin(2*q4)-0.5*cm2*m*cos(2*q3)*sin(2*q4);

D(2,3,1)=0;
D(2,3,2)=0;
D(2,3,3)=-c3*c4*s4*(m*cm2-I2xx+I2yy);
D(2,3,4)=-s3*(cos(2*q4))*(m*cm2-I2xx+I2yy);

D(2,4,1)=0; D(2,4,2)=0; D(2,4,4)=0;
D(2,4,3)=s3*(m*cm2+I2zz);

D(3,1,1)=cm2*m*(-sin(2*q1)*c2*c3*c3*c4*c4+2*s1*c1*c2*s3*s3*c4*c4-
sin(2*q1)*c2*s3*s3*c4*c4+2*c1*s1*c2*c3*c3*c4*c4+2*c1*s1*s2*c3*c4*s4-
sin(2*q1)*s2*c3*c4*s4)+cm*d*m*(2*c1*s1*c2*s3*c4-sin(2*q1)*c2*s3*c4);
D(3,1,2)=I2xx*c2*c3*c4*s4+I2xx*s2*s4*s4+I2yy*s2*c4*c4-
I2yy*c2*c3*c4*s4+cm2*m*(s1*s1*s2*c3*c3*c4*c4+c1*c1*s2*s3*s3*c4*c4+s1*s1*s2*s3
*s3*c4*c4+c1*c1*s2*c3*c3*c4*c4-c1*c1*c2*c3*c4*s4-
s1*s1*c2*c3*c4*s4)+cm*d*m*(c1*c1*s2*s3*c4+s1*s1*s2*s3*c4);
D(3,1,3)=-I2xx*s2*s3*c4*s4+I2yy*s2*s3*s4*c4+cm2*m*(2*s1*s1*c2*c3*s3*c4*c4-
c1*c1*c2*sin(2*q3)*c4*c4-
s1*s1*c2*sin(2*q3)*c4*c4+2*c1*c1*c2*c3*s3*c4*c4+c1*c1*s2*s3*c4*s4+s1*s1*s2*s3
*c4*s4)+cm*d*m*(-c1*c1*c2*c3*c4-s1*s1*c2*c3*c4);
D(3,1,4)=I2xx*s2*c3*cos(2*q4)-I2xx*c2*sin(2*q4)+2*I2yy*c2*c4*s4-
I2yy*s2*c3*cos(2*q4)+cm2*m*(2*s1*s1*c2*c3*c3*c4*s4+2*c1*c1*c2*s3*s3*c4*s4+2*s
1*s1*c2*s3*s3*c4*s4+2*c1*c1*c2*c3*c3*c4*s4-c1*c1*s2*c3*cos(2*q4)-
s1*s1*s2*c3*cos(2*q4))+cm*d*m*(c1*c1*c2*s3*s4+s1*s1*c2*s3*s4);

D(3,2,1)=0; D(3,2,2)=0;
D(3,2,3)=-c3*c4*s4*(m*cm2-I2xx+I2yy);
D(3,2,4)=-(cos(2*q4))*s3*(m*cm2-I2xx+I2yy);

D(3,3,1)=0; D(3,3,2)=0; D(3,3,3)=0;
D(3,3,4)=2*c4*s4*(I2xx-I2yy-cm2*m);

D(3,4,1)=0; D(3,4,2)=0; D(3,4,3)=0; D(3,4,4)=0;

D(4,1,1)=0;
D(4,1,2)=I2zz*c2*s3+cm2*m*c2*s3+cm*d*m*c4*c2+cm*d*m*s2*c3*s4;
D(4,1,3)=I2zz*s2*c3+cm2*m*s2*c3+cm*d*m*c2*s3*s4;
D(4,1,4)=-cm*d*m*s2*s4-cm*d*m*c2*c3*c4;

D(4,2,1)=0; D(4,2,2)=0; D(4,2,4)=0;
D(4,2,3)=s3*(m*cm2+I2zz);

D(4,3,1)=0; D(4,3,2)=0; D(4,3,3)=0; D(4,3,4)=0;
```

```
D(4,4,1)=0; D(4,4,2)=0; D(4,4,3)=0; D(4,4,4)=0;


for i=1:4
    for j=1:4
        for k=1:4
            c(i,j,k)=0.5*(gradient(M(k,j),q(i))+gradient(M(k,i),q(j))-
gradient(M(i,j),q(k)));
        end
    end
end
C=sym(diag([0;0;0;0]));
for k=1:4
    for j=1:4
        C(k,j)=c(1, j,k)*dq(1)+c(2, j,k)*dq(2)+c(3, j,k)*dq(3)+c(4,
j,k)*dq(4);
    end
end
```

Inertia matrix terms

D(1,1)=I_{2xx}(c_2s_4 + c_3c_4s_2)^2 + I_{2yy}(c_2c_4 - c_3s_2s_4)^2 + (d^2md)/4 + I_{1zz}c_2^2 - m(c_m^2c_2^2 - c_m^2 - d^2 - c_m^2c_2^2c_4^2 + c_m^2c_3^2c_4^2 - c_m^2c_2^2c_3^2c_4^2 + 2c_mdc_4s_3 + 2c_m^2c_2c_3c_4s_2s_4) + I_{1xx}s_2^2 + I_{2zz}s_2^2s_3^2
D(1,2)=I_{2zz}c_3s_2s_3 - I_{2yy}c_3s_2s_3 - I_{2xx}c_2c_4s_3s_4 + I_{2yy}c_2c_4s_3s_4 - c_mdmc_2s_4 - I_{2xx}c_3c_4^2s_2s_3 + I_{2yy}c_3c_4^2s_2s_3 + c_m^2mc_2c_4s_3s_4 - c_mdmc_3c_4s_2 + c_m^2mc_3c_4^2s_2s_3
D(1,3)=I_{2xx}c_2 - I_{2xx}c_2c_4^2 + I_{2yy}c_2c_4^2 + c_m^2mc_2c_4^2 + I_{2xx}c_3c_4s_2s_4 - I_{2yy}c_3c_4s_2s_4 - c_m^2mc_3c_4s_2s_4 - c_mdmc_2c_4s_3
D(1,4)=I_{2zz}s_2s_3 + c_m^2ms_2s_3 - c_mdmc_4s_2 - c_mdmc_2c_3s_4
D(2,1)=I_{2zz}c_3s_2s_3 - I_{2yy}c_3s_2s_3 - I_{2xx}c_2c_4s_3s_4 + I_{2yy}c_2c_4s_3s_4 - c_mdmc_2s_4 - I_{2xx}c_3c_4^2s_2s_3 + I_{2yy}c_3c_4^2s_2s_3 + c_m^2mc_2c_4s_3s_4 - c_mdmc_3c_4s_2 + c_m^2mc_3c_4^2s_2s_3
D(2,2)=I_{2xx}/4 + I_{1yy} + I_{2yy}/4 + I_{2zz}/2 + (3c_m^2m)/4 - (I_{2xx}cos(2q3))/4 + (I_{2xx}cos(2q4))/4 - (I_{2yy}cos(2q3))/4 - (I_{2yy}cos(2q4))/4 + (I_{2zz}cos(2q3))/2 - (I_{2xx}cos(2q3)cos(2q4))/4 + (I_{2yy}cos(2q3)cos(2q4))/4 + (c_m^2mcos(2q3))/4 - (c_m^2mcos(2q4))/4 + (c_m^2mcos(2q3)cos(2q4))/4
D(2,3)=c_4s_3s_4(mc_m^2 - I_{2xx} + I_{2yy})
D(2,4)=c_3(mc_m^2 + I_{2zz})
D(3,1)=I_{2yy}c_4(c_2c_4 - c_3s_2s_4) + I_{2xx}s_4(c_2s_4 + c_3c_4s_2) - c_mmc_4(dc_2s_3 - c_mc_2c_4 + c_mc_3s_2s_4)
D(3,2)=c_4s_3s_4(mc_m^2 - I_{2xx} + I_{2yy})
D(3,3)=I_{2yy} + c_m^2m + I_{2xx}s_4^2 - I_{2yy}s_4^2 - c_m^2ms_4^2
D(3,4)=0$\\
D(4,1)=I_{2zz}s_2s_3 + c_m^2ms_2s_3 - c_mdmc_4s_2 - c_mdmc_2c_3s_4
D(4,2)=c_3(mc_m^2 + I_{2zz})
D(4,3)=0$
D(4,4)=mc_m^2 + I_{2zz}

Coriolis and centrifugal terms

```
C(1,1)=dq4*(cm*m*(d*sin(q3)*sin(q4) + cm*cos(q2)*cos(q3)*sin(q2) -
cm*cos(q2)^2*cos(q4)*sin(q4) + cm*cos(q3)^2*cos(q4)*sin(q4) -
2*cm*cos(q2)*cos(q3)*cos(q4)^2*sin(q2) -
cm*cos(q2)^2*cos(q3)^2*cos(q4)*sin(q4)) + I2xx*(cos(q2)*sin(q4) +
cos(q3)*cos(q4)*sin(q2))*(cos(q2)*cos(q4) - cos(q3)*sin(q2)*sin(q4)) -
I2yy*(cos(q2)*sin(q4) + cos(q3)*cos(q4)*sin(q2))*(cos(q2)*cos(q4) -
cos(q3)*sin(q2)*sin(q4))) - dq3*(cm*m*cos(q4)*(d*cos(q3) -
cm*cos(q3)*cos(q4)*sin(q3) - cm*cos(q2)*sin(q2)*sin(q3)*sin(q4) +
cm*cos(q2)^2*cos(q3)*cos(q4)*sin(q3)) - I2zz*cos(q3)*sin(q2)^2*sin(q3) +
I2xx*cos(q4)*sin(q2)*sin(q3)*(cos(q2)*sin(q4) + cos(q3)*cos(q4)*sin(q2)) -
I2yy*sin(q2)*sin(q3)*sin(q4)*(cos(q2)*cos(q4) - cos(q3)*sin(q2)*sin(q4))) -
dq2*((I1zz*sin(2*q2))/2 - (I1xx*sin(2*q2))/2 + I2xx*(cos(q2)*sin(q4) +
cos(q3)*cos(q4)*sin(q2))*(sin(q2)*sin(q4) - cos(q2)*cos(q3)*cos(q4)) +
I2yy*(cos(q4)*sin(q2) + cos(q2)*cos(q3)*sin(q4))*(cos(q2)*cos(q4) -
cos(q3)*sin(q2)*sin(q4)) + cm^2*m*(cos(q2)*cos(q4)^2*sin(q2) -
cos(q2)*sin(q2) - cos(q3)*cos(q4)*sin(q4) +
2*cos(q2)^2*cos(q3)*cos(q4)*sin(q4) + cos(q2)*cos(q3)^2*cos(q4)^2*sin(q2)) -
I2zz*cos(q2)*sin(q2)*sin(q3)^2);
C(2,1)=(I2xx*dq1*sin(2*q2))/8 - (I1xx*dq1*sin(2*q2))/2 +
(I2yy*dq1*sin(2*q2))/8 + (I1zz*dq1*sin(2*q2))/2 - (I2zz*dq1*sin(2*q2))/4 +
(I2xx*dq3*sin(q2))/4 + (I2yy*dq3*sin(q2))/4 - (I2xx*dq3*cos(2*q3)*sin(q2))/4
- (I2xx*dq3*cos(2*q4)*sin(q2))/4 - (I2yy*dq3*cos(2*q3)*sin(q2))/4 +
(I2yy*dq3*cos(2*q4)*sin(q2))/4 + (I2zz*dq3*cos(2*q3)*sin(q2))/2 -
(cm^2*dq1*m*sin(2*q2))/8 - (I2xx*dq1*cos(2*q3)*sin(2*q2))/8 -
(3*I2xx*dq1*cos(2*q4)*sin(2*q2))/8 - (I2yy*dq1*cos(2*q3)*sin(2*q2))/8 +
(3*I2yy*dq1*cos(2*q4)*sin(2*q2))/8 + (I2zz*dq1*cos(2*q3)*sin(2*q2))/4 -
(I2zz*dq4*cos(q2)*sin(q3))/2 + (cm^2*dq3*m*sin(q2))/4 +
(cm^2*dq3*m*cos(2*q3)*sin(q2))/4 + (cm^2*dq3*m*cos(2*q4)*sin(q2))/4 -
(I2xx*dq1*cos(2*q2)*sin(2*q4)*cos(q3))/2 -
(I2xx*dq3*cos(2*q3)*cos(2*q4)*sin(q2))/4 +
(I2yy*dq1*cos(2*q2)*sin(2*q4)*cos(q3))/2 +
(I2yy*dq3*cos(2*q3)*cos(2*q4)*sin(q2))/4 + (cm^2*dq1*m*cos(2*q3)*sin(2*q2))/8
+ (3*cm^2*dq1*m*cos(2*q4)*sin(2*q2))/8 +
(I2xx*dq4*sin(2*q3)*sin(2*q4)*sin(q2))/4 -
(I2yy*dq4*sin(2*q3)*sin(2*q4)*sin(q2))/4 - (cm^2*dq4*m*cos(q2)*sin(q3))/2 -
(I2xx*dq1*cos(2*q3)*cos(2*q4)*sin(2*q2))/8 +
(I2yy*dq1*cos(2*q3)*cos(2*q4)*sin(2*q2))/8 -
(I2xx*dq3*sin(2*q4)*cos(q2)*cos(q3))/2 -
(I2xx*dq4*cos(2*q4)*cos(q2)*sin(q3))/2 +
(I2yy*dq3*sin(2*q4)*cos(q2)*cos(q3))/2 +
(I2yy*dq4*cos(2*q4)*cos(q2)*sin(q3))/2 +
(cm^2*dq1*m*cos(2*q2)*sin(2*q4)*cos(q3))/2 +
(cm^2*dq3*m*cos(2*q3)*cos(2*q4)*sin(q2))/4 -
(cm^2*dq4*m*sin(2*q3)*sin(2*q4)*sin(q2))/4 +
(cm^2*dq1*m*cos(2*q3)*cos(2*q4)*sin(2*q2))/8 +
(cm^2*dq3*m*sin(2*q4)*cos(q2)*cos(q3))/2 +
(cm^2*dq4*m*cos(2*q4)*cos(q2)*sin(q3))/2;
C(3,1)=(I2yy*dq1*sin(2*q3))/2 - (I2zz*dq1*sin(2*q3))/2 - (I2xx*dq2*sin(q2))/2
- (I2yy*dq2*sin(q2))/2 + (I2zz*dq2*sin(q2))/2 + I2yy*dq2*cos(q3)^2*sin(q2) -
I2zz*dq2*cos(q3)^2*sin(q2) - (I2xx*dq4*cos(q3)*sin(q2))/2 +
(I2yy*dq4*cos(q3)*sin(q2))/2 - (I2zz*dq4*cos(q3)*sin(q2))/2 +
I2xx*dq2*cos(q3)^2*cos(q4)^2*sin(q2) - I2yy*dq2*cos(q3)^2*cos(q4)^2*sin(q2) +
I2xx*dq4*cos(q2)*cos(q4)*sin(q4) - I2yy*dq4*cos(q2)*cos(q4)*sin(q4) +
I2xx*dq1*cos(q3)*cos(q4)^2*sin(q3) + I2xx*dq4*cos(q3)*cos(q4)^2*sin(q2) -
I2yy*dq1*cos(q2)^2*cos(q3)*sin(q3) - I2yy*dq1*cos(q3)*cos(q4)^2*sin(q3) -
I2yy*dq4*cos(q3)*cos(q4)^2*sin(q2) + I2zz*dq1*cos(q2)^2*cos(q3)*sin(q3) -
I2xx*dq1*cos(q2)^2*cos(q3)*cos(q4)^2*sin(q3) +
```

```
I2yy*dq1*cos(q2)^2*cos(q3)*cos(q4)^2*sin(q3) -
cm^2*dq2*m*cos(q3)^2*cos(q4)^2*sin(q2) +
I2xx*dq2*cos(q2)*cos(q3)*cos(q4)*sin(q4) -
I2yy*dq2*cos(q2)*cos(q3)*cos(q4)*sin(q4) - cm^2*dq4*m*cos(q2)*cos(q4)*sin(q4)
+ cm*d*dq1*m*cos(q3)*cos(q4) - cm^2*dq1*m*cos(q3)*cos(q4)^2*sin(q3) -
cm^2*dq4*m*cos(q3)*cos(q4)^2*sin(q2) +
cm^2*dq1*m*cos(q2)^2*cos(q3)*cos(q4)^2*sin(q3) -
cm^2*dq2*m*cos(q2)*cos(q3)*cos(q4)*sin(q4) +
I2xx*dq1*cos(q2)*cos(q4)*sin(q2)*sin(q3)*sin(q4) -
I2yy*dq1*cos(q2)*cos(q4)*sin(q2)*sin(q3)*sin(q4) -
cm^2*dq1*m*cos(q2)*cos(q4)*sin(q2)*sin(q3)*sin(q4);
C(4,1)=(I2yy*dq1*sin(2*q4))/8 - (I2xx*dq1*sin(2*q4))/8 -
(I2xx*dq3*sin(2*q4)*cos(q2))/2 + (I2yy*dq3*sin(2*q4)*cos(q2))/2 +
(cm^2*dq1*m*sin(2*q4))/8 - (3*I2xx*dq1*cos(2*q2)*sin(2*q4))/8 +
(I2xx*dq1*cos(2*q3)*sin(2*q4))/8 + (3*I2yy*dq1*cos(2*q2)*sin(2*q4))/8 -
(I2yy*dq1*cos(2*q3)*sin(2*q4))/8 + (I2zz*dq2*cos(q2)*sin(q3))/2 +
(I2zz*dq3*cos(q3)*sin(q2))/2 + (cm^2*dq3*m*sin(2*q4)*cos(q2))/2 -
(I2xx*dq1*cos(2*q4)*sin(2*q2)*cos(q3))/2 +
(I2yy*dq1*cos(2*q4)*sin(2*q2)*cos(q3))/2 +
(3*cm^2*dq1*m*cos(2*q2)*sin(2*q4))/8 - (cm^2*dq1*m*cos(2*q3)*sin(2*q4))/8 -
(I2xx*dq2*sin(2*q3)*sin(2*q4)*sin(q2))/4 +
(I2yy*dq2*sin(2*q3)*sin(2*q4)*sin(q2))/4 + (cm^2*dq2*m*cos(q2)*sin(q3))/2 +
(cm^2*dq3*m*cos(q3)*sin(q2))/2 - (I2xx*dq1*cos(2*q2)*cos(2*q3)*sin(2*q4))/8 +
(I2yy*dq1*cos(2*q2)*cos(2*q3)*sin(2*q4))/8 +
(I2xx*dq2*cos(2*q4)*cos(q2)*sin(q3))/2 -
(I2xx*dq3*cos(2*q4)*cos(q3)*sin(q2))/2 -
(I2yy*dq2*cos(2*q4)*cos(q2)*sin(q3))/2 +
(I2yy*dq3*cos(2*q4)*cos(q3)*sin(q2))/2 +
(cm^2*dq1*m*cos(2*q4)*sin(2*q2)*cos(q3))/2 +
(cm^2*dq2*m*sin(2*q3)*sin(2*q4)*sin(q2))/4 +
(cm^2*dq1*m*cos(2*q2)*cos(2*q3)*sin(2*q4))/8 - cm*d*dq1*m*sin(q3)*sin(q4) -
(cm^2*dq2*m*cos(2*q4)*cos(q2)*sin(q3))/2 +
(cm^2*dq3*m*cos(2*q4)*cos(q3)*sin(q2))/2;
C(1,2)=(I1xx*dq1*sin(2*q2))/2 - (I2xx*dq1*sin(2*q2))/8 -
(I2yy*dq1*sin(2*q2))/8 - (I1zz*dq1*sin(2*q2))/2 + (I2zz*dq1*sin(2*q2))/4 -
(I2xx*dq3*sin(q2))/4 - (I2yy*dq3*sin(q2))/4 - (I2xx*dq2*sin(2*q3)*cos(q2))/4
- (I2xx*dq3*cos(2*q3)*sin(q2))/4 + (I2xx*dq3*cos(2*q4)*sin(q2))/4 -
(I2yy*dq2*sin(2*q3)*cos(q2))/4 - (I2yy*dq3*cos(2*q3)*sin(q2))/4 -
(I2yy*dq3*cos(2*q4)*sin(q2))/4 + (I2zz*dq2*sin(2*q3)*cos(q2))/2 +
(I2zz*dq3*cos(2*q3)*sin(q2))/2 + (cm^2*dq1*m*sin(2*q2))/8 +
(I2xx*dq1*cos(2*q3)*sin(2*q2))/8 + (3*I2xx*dq1*cos(2*q4)*sin(2*q2))/8 +
(I2yy*dq1*cos(2*q3)*sin(2*q2))/8 - (3*I2yy*dq1*cos(2*q4)*sin(2*q2))/8 -
(I2zz*dq1*cos(2*q3)*sin(2*q2))/4 + (I2zz*dq4*cos(q2)*sin(q3))/2 -
(cm^2*dq3*m*sin(q2))/4 + (cm^2*dq2*m*sin(2*q3)*cos(q2))/4 +
(cm^2*dq3*m*cos(2*q3)*sin(q2))/4 - (cm^2*dq3*m*cos(2*q4)*sin(q2))/4 +
(I2xx*dq2*sin(2*q4)*sin(q2)*sin(q3))/2 -
(I2yy*dq2*sin(2*q4)*sin(q2)*sin(q3))/2 +
(I2xx*dq1*cos(2*q2)*sin(2*q4)*cos(q3))/2 -
(I2xx*dq2*cos(2*q4)*sin(2*q3)*cos(q2))/4 -
(I2xx*dq3*cos(2*q3)*cos(2*q4)*sin(q2))/4 -
(I2yy*dq1*cos(2*q2)*sin(2*q4)*cos(q3))/2 +
(I2yy*dq2*cos(2*q4)*sin(2*q3)*cos(q2))/4 +
(I2yy*dq3*cos(2*q3)*cos(2*q4)*sin(q2))/4 - (cm^2*dq1*m*cos(2*q3)*sin(2*q2))/8
- (3*cm^2*dq1*m*cos(2*q4)*sin(2*q2))/8 +
(I2xx*dq4*sin(2*q3)*sin(2*q4)*sin(q2))/4 -
(I2yy*dq4*sin(2*q3)*sin(2*q4)*sin(q2))/4 + (cm^2*dq4*m*cos(q2)*sin(q3))/2 +
(I2xx*dq1*cos(2*q3)*cos(2*q4)*sin(2*q2))/8 -
```

```
(I2yy*dq1*cos(2*q3)*cos(2*q4)*sin(2*q2))/8 -
(I2xx*dq4*cos(2*q4)*cos(q2)*sin(q3))/2 +
(I2yy*dq4*cos(2*q4)*cos(q2)*sin(q3))/2 -
(cm^2*dq2*m*sin(2*q4)*sin(q2)*sin(q3))/2 -
(cm^2*dq1*m*cos(2*q2)*sin(2*q4)*cos(q3))/2 +
(cm^2*dq2*m*cos(2*q4)*sin(2*q3)*cos(q2))/4 +
(cm^2*dq3*m*cos(2*q3)*cos(2*q4)*sin(q2))/4 -
(cm^2*dq4*m*sin(2*q3)*sin(2*q4)*sin(q2))/4 -
(cm^2*dq1*m*cos(2*q3)*cos(2*q4)*sin(2*q2))/8 - cm*d*dq4*m*cos(q2)*cos(q4) +
cm*d*dq2*m*sin(q2)*sin(q4) + (cm^2*dq4*m*cos(2*q4)*cos(q2)*sin(q3))/2 -
cm*d*dq2*m*cos(q2)*cos(q3)*cos(q4) + cm*d*dq3*m*cos(q4)*sin(q2)*sin(q3) +
cm*d*dq4*m*cos(q3)*sin(q2)*sin(q4);
C(2,2)=(I2xx*dq3*sin(2*q3))/4 - (I2xx*dq4*sin(2*q4))/4 +
(I2yy*dq3*sin(2*q3))/4 + (I2yy*dq4*sin(2*q4))/4 - (I2zz*dq3*sin(2*q3))/2 -
(cm^2*dq3*m*sin(2*q3))/4 + (cm^2*dq4*m*sin(2*q4))/4 +
(I2xx*dq3*cos(2*q4)*sin(2*q3))/4 + (I2xx*dq4*cos(2*q3)*sin(2*q4))/4 -
(I2yy*dq3*cos(2*q4)*sin(2*q3))/4 - (I2yy*dq4*cos(2*q3)*sin(2*q4))/4 -
(cm^2*dq3*m*cos(2*q4)*sin(2*q3))/4 - (cm^2*dq4*m*cos(2*q3)*sin(2*q4))/4;
C(3,2)=(I2zz*dq2*sin(2*q3))/2 - (I2yy*dq2*sin(2*q3))/4 -
(I2xx*dq2*sin(2*q3))/4 - (I2xx*dq1*sin(q2))/2 - (I2yy*dq1*sin(q2))/2 +
(I2zz*dq1*sin(q2))/2 + (I2zz*dq4*sin(q3))/2 - (I2xx*dq4*cos(2*q4)*sin(q3))/2
+ (I2yy*dq4*cos(2*q4)*sin(q3))/2 + (I2xx*dq1*cos(q3)^2*sin(q2))/2 +
(I2yy*dq1*cos(q3)^2*sin(q2))/2 - I2zz*dq1*cos(q3)^2*sin(q2) +
(cm^2*dq2*m*sin(2*q3))/4 + (cm^2*dq4*m*sin(q3))/2 +
(cm^2*dq4*m*cos(2*q4)*sin(q3))/2 - (cm^2*dq1*m*cos(q3)^2*sin(q2))/2 +
(I2xx*dq1*cos(2*q4)*cos(q3)^2*sin(q2))/2 -
(I2yy*dq1*cos(2*q4)*cos(q3)^2*sin(q2))/2 +
(I2xx*dq1*sin(2*q4)*cos(q2)*cos(q3))/2 -
(I2xx*dq2*cos(2*q4)*cos(q3)*sin(q3))/2 -
(I2yy*dq1*sin(2*q4)*cos(q2)*cos(q3))/2 +
(I2yy*dq2*cos(2*q4)*cos(q3)*sin(q3))/2 -
(cm^2*dq1*m*cos(2*q4)*cos(q3)^2*sin(q2))/2 -
(cm^2*dq1*m*sin(2*q4)*cos(q2)*cos(q3))/2 +
(cm^2*dq2*m*cos(2*q4)*cos(q3)*sin(q3))/2;
C(4,2)=(I2xx*dq2*sin(2*q4))/4 - (I2yy*dq2*sin(2*q4))/4 - (I2zz*dq3*sin(q3))/2
+ (I2xx*dq3*cos(2*q4)*sin(q3))/2 - (I2yy*dq3*cos(2*q4)*sin(q3))/2 -
(cm^2*dq2*m*sin(2*q4))/4 - (I2xx*dq2*cos(2*q3)*sin(2*q4))/4 +
(I2yy*dq2*cos(2*q3)*sin(2*q4))/4 + (I2zz*dq1*cos(q2)*sin(q3))/2 -
(cm^2*dq3*m*sin(q3))/2 - (cm^2*dq3*m*cos(2*q4)*sin(q3))/2 +
(cm^2*dq2*m*cos(2*q3)*sin(2*q4))/4 - (I2xx*dq1*sin(2*q3)*sin(2*q4)*sin(q2))/4
+ (I2yy*dq1*sin(2*q3)*sin(2*q4)*sin(q2))/4 + (cm^2*dq1*m*cos(q2)*sin(q3))/2 +
(I2xx*dq1*cos(2*q4)*cos(q2)*sin(q3))/2 -
(I2yy*dq1*cos(2*q4)*cos(q2)*sin(q3))/2 +
(cm^2*dq1*m*sin(2*q3)*sin(2*q4)*sin(q2))/4 -
(cm^2*dq1*m*cos(2*q4)*cos(q2)*sin(q3))/2;
C(1,3)=(I2zz*dq1*sin(2*q3))/4 - (I2yy*dq1*sin(2*q3))/8 -
(I2xx*dq1*sin(2*q3))/8 - (I2xx*dq2*sin(q2))/4 - (I2yy*dq2*sin(q2))/4 -
(I2xx*dq2*cos(2*q3)*sin(q2))/4 + (I2xx*dq2*cos(2*q4)*sin(q2))/4 +
(I2xx*dq4*sin(2*q4)*cos(q2))/2 - (I2yy*dq2*cos(2*q3)*sin(q2))/4 -
(I2yy*dq2*cos(2*q4)*sin(q2))/4 - (I2yy*dq4*sin(2*q4)*cos(q2))/2 +
(I2zz*dq2*cos(2*q3)*sin(q2))/2 + (cm^2*dq1*m*sin(2*q3))/8 +
(I2xx*dq1*cos(2*q2)*sin(2*q3))/8 - (I2xx*dq1*cos(2*q4)*sin(2*q3))/8 +
(I2yy*dq1*cos(2*q2)*sin(2*q3))/8 + (I2yy*dq1*cos(2*q4)*sin(2*q3))/8 -
(I2zz*dq1*cos(2*q2)*sin(2*q3))/4 + (I2zz*dq4*cos(q3)*sin(q2))/2 -
(cm^2*dq2*m*sin(q2))/4 + (cm^2*dq2*m*cos(2*q3)*sin(q2))/4 -
(cm^2*dq2*m*cos(2*q4)*sin(q2))/4 - (cm^2*dq4*m*sin(2*q4)*cos(q2))/2 -
(I2xx*dq3*sin(2*q4)*sin(q2)*sin(q3))/2 +
```

```
(I2yy*dq3*sin(2*q4)*sin(q2)*sin(q3))/2 -
(I2xx*dq2*cos(2*q3)*cos(2*q4)*sin(q2))/4 +
(I2yy*dq2*cos(2*q3)*cos(2*q4)*sin(q2))/4 - (cm^2*dq1*m*cos(2*q2)*sin(2*q3))/8
+ (cm^2*dq1*m*cos(2*q4)*sin(2*q3))/8 -
(I2xx*dq1*sin(2*q2)*sin(2*q4)*sin(q3))/4 +
(I2yy*dq1*sin(2*q2)*sin(2*q4)*sin(q3))/4 + (cm^2*dq4*m*cos(q3)*sin(q2))/2 +
(I2xx*dq1*cos(2*q2)*cos(2*q4)*sin(2*q3))/8 -
(I2yy*dq1*cos(2*q2)*cos(2*q4)*sin(2*q3))/8 +
(I2xx*dq4*cos(2*q4)*cos(q3)*sin(q2))/2 -
(I2yy*dq4*cos(2*q4)*cos(q3)*sin(q2))/2 +
(cm^2*dq3*m*sin(2*q4)*sin(q2)*sin(q3))/2 +
(cm^2*dq2*m*cos(2*q3)*cos(2*q4)*sin(q2))/4 +
(cm^2*dq1*m*sin(2*q2)*sin(2*q4)*sin(q3))/4 -
(cm^2*dq1*m*cos(2*q2)*cos(2*q4)*sin(2*q3))/8 - cm*d*dq1*m*cos(q3)*cos(q4) -
(cm^2*dq4*m*cos(2*q4)*cos(q3)*sin(q2))/2 - cm*d*dq3*m*cos(q2)*cos(q3)*cos(q4)
+ cm*d*dq2*m*cos(q4)*sin(q2)*sin(q3) + cm*d*dq4*m*cos(q2)*sin(q3)*sin(q4);
C(2,3)=(I2xx*dq2*sin(2*q3))/4 + (I2yy*dq2*sin(2*q3))/4 -
(I2zz*dq2*sin(2*q3))/2 + (I2xx*dq1*sin(q2))/2 + (I2yy*dq1*sin(q2))/2 -
(I2zz*dq1*sin(q2))/2 - (I2zz*dq4*sin(q3))/2 - (I2xx*dq3*sin(2*q4)*cos(q3))/2
- (I2xx*dq4*cos(2*q4)*sin(q3))/2 + (I2yy*dq3*sin(2*q4)*cos(q3))/2 +
(I2yy*dq4*cos(2*q4)*sin(q3))/2 - (I2xx*dq1*cos(q3)^2*sin(q2))/2 -
(I2yy*dq1*cos(q3)^2*sin(q2))/2 + I2zz*dq1*cos(q3)^2*sin(q2) -
(cm^2*dq2*m*sin(2*q3))/4 - (cm^2*dq4*m*sin(q3))/2 +
(cm^2*dq3*m*sin(2*q4)*cos(q3))/2 + (cm^2*dq4*m*cos(2*q4)*sin(q3))/2 +
(cm^2*dq1*m*cos(q3)^2*sin(q2))/2 - (I2xx*dq1*cos(2*q4)*cos(q3)^2*sin(q2))/2 +
(I2yy*dq1*cos(2*q4)*cos(q3)^2*sin(q2))/2 -
(I2xx*dq1*sin(2*q4)*cos(q2)*cos(q3))/2 +
(I2xx*dq2*cos(2*q4)*cos(q3)*sin(q3))/2 +
(I2yy*dq1*sin(2*q4)*cos(q2)*cos(q3))/2 -
(I2yy*dq2*cos(2*q4)*cos(q3)*sin(q3))/2 +
(cm^2*dq1*m*cos(2*q4)*cos(q3)^2*sin(q2))/2 +
(cm^2*dq1*m*sin(2*q4)*cos(q2)*cos(q3))/2 -
(cm^2*dq2*m*cos(2*q4)*cos(q3)*sin(q3))/2;
C(3,3)=-(dq4*sin(2*q4)*(m*cm^2 - I2xx + I2yy))/2;
C(4,3)=(I2yy*dq3*sin(2*q4))/2 - (I2xx*dq3*sin(2*q4))/2 - (I2zz*dq2*sin(q3))/2
- (I2xx*dq1*sin(2*q4)*cos(q2))/2 + (I2xx*dq2*cos(2*q4)*sin(q3))/2 +
(I2yy*dq1*sin(2*q4)*cos(q2))/2 - (I2yy*dq2*cos(2*q4)*sin(q3))/2 +
(cm^2*dq3*m*sin(2*q4))/2 + (I2zz*dq1*cos(q3)*sin(q2))/2 -
(cm^2*dq2*m*sin(q3))/2 + (cm^2*dq1*m*sin(2*q4)*cos(q2))/2 -
(cm^2*dq2*m*cos(2*q4)*sin(q3))/2 + (cm^2*dq1*m*cos(q3)*sin(q2))/2 -
(I2xx*dq1*cos(2*q4)*cos(q3)*sin(q2))/2 +
(I2yy*dq1*cos(2*q4)*cos(q3)*sin(q2))/2 +
(cm^2*dq1*m*cos(2*q4)*cos(q3)*sin(q2))/2;
C(1,4)=(I2xx*dq1*sin(2*q4))/8 - (I2yy*dq1*sin(2*q4))/8 +
(I2xx*dq3*sin(2*q4)*cos(q2))/2 - (I2yy*dq3*sin(2*q4)*cos(q2))/2 -
(cm^2*dq1*m*sin(2*q4))/8 + (3*I2xx*dq1*cos(2*q2)*sin(2*q4))/8 -
(I2xx*dq1*cos(2*q3)*sin(2*q4))/8 - (3*I2yy*dq1*cos(2*q2)*sin(2*q4))/8 +
(I2yy*dq1*cos(2*q3)*sin(2*q4))/8 + (I2zz*dq2*cos(q2)*sin(q3))/2 +
(I2zz*dq3*cos(q3)*sin(q2))/2 - (cm^2*dq3*m*sin(2*q4)*cos(q2))/2 +
(I2xx*dq1*cos(2*q4)*sin(2*q2)*cos(q3))/2 -
(I2yy*dq1*cos(2*q4)*sin(2*q2)*cos(q3))/2 -
(3*cm^2*dq1*m*cos(2*q2)*sin(2*q4))/8 + (cm^2*dq1*m*cos(2*q3)*sin(2*q4))/8 +
(I2xx*dq2*sin(2*q3)*sin(2*q4)*sin(q2))/4 -
(I2yy*dq2*sin(2*q3)*sin(2*q4)*sin(q2))/4 + (cm^2*dq2*m*cos(q2)*sin(q3))/2 +
(cm^2*dq3*m*cos(q3)*sin(q2))/2 + (I2xx*dq1*cos(2*q2)*cos(2*q3)*sin(2*q4))/8 -
(I2yy*dq1*cos(2*q2)*cos(2*q3)*sin(2*q4))/8 -
(I2xx*dq2*cos(2*q4)*cos(q2)*sin(q3))/2 +
```

```
(I2xx*dq3*cos(2*q4)*cos(q3)*sin(q2))/2 +
(I2yy*dq2*cos(2*q4)*cos(q2)*sin(q3))/2 -
(I2yy*dq3*cos(2*q4)*cos(q3)*sin(q2))/2 -
(cm^2*dq1*m*cos(2*q4)*sin(2*q2)*cos(q3))/2 -
(cm^2*dq2*m*sin(2*q3)*sin(2*q4)*sin(q2))/4 -
(cm^2*dq1*m*cos(2*q2)*cos(2*q3)*sin(2*q4))/8 - cm*d*dq2*m*cos(q2)*cos(q4) +
cm*d*dq1*m*sin(q3)*sin(q4) + cm*d*dq4*m*sin(q2)*sin(q4) +
(cm^2*dq2*m*cos(2*q4)*cos(q2)*sin(q3))/2 -
(cm^2*dq3*m*cos(2*q4)*cos(q3)*sin(q2))/2 - cm*d*dq4*m*cos(q2)*cos(q3)*cos(q4)
+ cm*d*dq2*m*cos(q3)*sin(q2)*sin(q4) + cm*d*dq3*m*cos(q2)*sin(q3)*sin(q4);
C(2,4)=(I2yy*dq2*sin(2*q4))/4 - (I2xx*dq2*sin(2*q4))/4 - (I2zz*dq3*sin(q3))/2
- (I2xx*dq3*cos(2*q4)*sin(q3))/2 + (I2yy*dq3*cos(2*q4)*sin(q3))/2 +
(cm^2*dq2*m*sin(2*q4))/4 + (I2xx*dq2*cos(2*q3)*sin(2*q4))/4 -
(I2yy*dq2*cos(2*q3)*sin(2*q4))/4 - (I2zz*dq1*cos(q2)*sin(q3))/2 -
(cm^2*dq3*m*sin(q3))/2 + (cm^2*dq3*m*cos(2*q4)*sin(q3))/2 -
(cm^2*dq2*m*cos(2*q3)*sin(2*q4))/4 + (I2xx*dq1*sin(2*q3)*sin(2*q4)*sin(q2))/4
- (I2yy*dq1*sin(2*q3)*sin(2*q4)*sin(q2))/4 - (cm^2*dq1*m*cos(q2)*sin(q3))/2 -
(I2xx*dq1*cos(2*q4)*cos(q2)*sin(q3))/2 +
(I2yy*dq1*cos(2*q4)*cos(q2)*sin(q3))/2 -
(cm^2*dq1*m*sin(2*q3)*sin(2*q4)*sin(q2))/4 +
(cm^2*dq1*m*cos(2*q4)*cos(q2)*sin(q3))/2;
C(3,4)=(I2xx*dq3*sin(2*q4))/2 - (I2yy*dq3*sin(2*q4))/2 + (I2zz*dq2*sin(q3))/2
+ (I2xx*dq1*sin(2*q4)*cos(q2))/2 - (I2xx*dq2*cos(2*q4)*sin(q3))/2 -
(I2yy*dq1*sin(2*q4)*cos(q2))/2 + (I2yy*dq2*cos(2*q4)*sin(q3))/2 -
(cm^2*dq3*m*sin(2*q4))/2 - (I2zz*dq1*cos(q3)*sin(q2))/2 +
(cm^2*dq2*m*sin(q3))/2 - (cm^2*dq1*m*sin(2*q4)*cos(q2))/2 +
(cm^2*dq2*m*cos(2*q4)*sin(q3))/2 - (cm^2*dq1*m*cos(q3)*sin(q2))/2 +
(I2xx*dq1*cos(2*q4)*cos(q3)*sin(q2))/2 -
(I2yy*dq1*cos(2*q4)*cos(q3)*sin(q2))/2 -
(cm^2*dq1*m*cos(2*q4)*cos(q3)*sin(q2))/2;
C(4,4)=0;
```

Gravitational matrix terms

```
G1=g*m*(d*cos(q1) - cm*cos(q4)*(cos(q1)*sin(q3) + cos(q2)*cos(q3)*sin(q1)) +
cm*sin(q1)*sin(q2)*sin(q4)) + (d*g*md*cos(q1))/2;
G2=-cm*g*m*cos(q1)*(cos(q2)*sin(q4) + cos(q3)*cos(q4)*sin(q2));
G3=-cm*g*m*cos(q4)*(cos(q3)*sin(q1) + cos(q1)*cos(q2)*sin(q3));
G4=g*m*(cm*sin(q4)*(sin(q1)*sin(q3) - cos(q1)*cos(q2)*cos(q3)) -
cm*cos(q1)*cos(q4)*sin(q2));
```

A.1.2 Dielectric Elastomer Actuator Modelling Code

ogdenfmincon.m

```
global eap11strain
global eap11stress
global eap11volt
global eap11widthstretch
eap11strain=importdata('eap11strain.mat');
eap11stress=importdata('eap11stress.mat');
eap11volt=importdata('eap11volt.mat');
eap11widthstretch=importdata('eap11widthstretch.mat');


options = optimoptions('fmincon');
options.ConstraintTolerance=1e-12;
options.StepTolerance=1e-15;
options.MaxFunctionEvaluations=1e10;

mu1=1e6;
mu2=1e6;
mu3=mu2;
alpha1=10; alpha2= 10; alpha3=10;

x0=[mu1, mu2,mu3, alpha1, alpha2,alpha3];
lb=0; ub=10000*x0;

[x err]= fmincon(@ogdentest3rd, x0, [], [], [],[], lb, ub, [])
```

ogdentest.m

```
%ogden 3rd order function
[ogden]= ogdentest3rd(X)

global eap11strain
global eap11stress
global eap11volt global
eap11widthstretch
    mu1=X(1); mu2=X(2); mu3=X(3);
alpha1=X(4); alpha2=X(5); alpha3=X(6);

stress=zeros(35,1);
stress2=zeros(35,1);
e0=8.85e-12; er=3; t0=40e-6;
    for i=1:35
lam2=eap11strain(i)+1;
    V=eap11volt(i);

lam1=eap11widthstretch(i);
      dW2=((mu1*(alpha1*lam2^(alpha1 - 1) -
(alpha1*(1/(lam1*lam2))^(alpha1 -
1))/(lam1*lam2^2)))/alpha1)+((mu2*(alpha2*lam2^(alpha2 - 1) -
(alpha2*(1/(lam1*lam2))^(alpha2 -
1))/(lam1*lam2^2)))/alpha2)+((mu3*(alpha3*lam2^(alpha3 - 1) -
(alpha3*(1/(lam1*lam2))^(alpha3 - 1))/(lam1*lam2^2)))/alpha3);
    Ue=e0*er*0.79*0.7*(lam1*lam2*V/t0)^2;
stress(i)=lam2*dW2-(Ue);      stress2(i)=0.017/(t0*0.048/lam2);

end
errr=stress-eap11stress*1.0625; ogden=rms(errr);
```

ogdenmodel.m

```
%ogden model
mu1=0.06136e6;
mu2=1.2027e6;
mu3=1.203e6;
alpha1=3.312;
alpha2=0.2682;
alpha3=-0.1631;

t0=40e-6; W=0.048;
e0=8.85e-12; er=3;
strain=[0:0.01:1.4];
m=0.0949533;
g=9.81;
F=m*g;
Vs=zeros(141,1); for
i=1:141
lam2=strain(i)+1;
         if(i==1)
V=0;     elseif
(Vs(i-1)<0)
V=0;     else
        V=real(Vs(i-1));
             end %m=45
if(m<0.045) lam1=3e-8*V^2-
2e-5*V+0.9007;
%m=55 elseif(m<0.055)
lam1=4e-8*V^2-2e-5*V+0.8667;
%m=75 elseif(m<0.075)
lam1=5e-8*V^2-2e-5*V+0.8395;
%m=85 elseif(m<0.085)
lam1=4e-8*V^2+9e-5*V+0.8014;
%m=95
else
lam1=1e-8*V^2+2e-5*V+0.7915; end    dW2=((mu1*(alpha1*lam2^(alpha1 - 1)
- (alpha1*(1/(lam1*lam2))^(alpha1 -
1))/(lam1*lam2^2)))/alpha1)+((mu2*(alpha2*lam2^(alpha2 - 1) -
(alpha2*(1/(lam1*lam2))^(alpha2 -
1))/(lam1*lam2^2)))/alpha2)+((mu3*(alpha3*lam2^(alpha3 - 1) -
(alpha3*(1/(lam1*lam2))^(alpha3 - 1))/(lam1*lam2^2)))/alpha3);

    Vs(i)=(t0/(lam1*lam2*0.79*0.8))*sqrt((1/(e0*er))*(lam2*dW2-
(lam2*F/(W*t0)))); end
```

Appendix B

Data Sheets

B.1 Maxon EC-Max 22 Brushless DC Motor

maxon EC-max

EC-max 22 ∅22 mm, brushless, 12 Watt

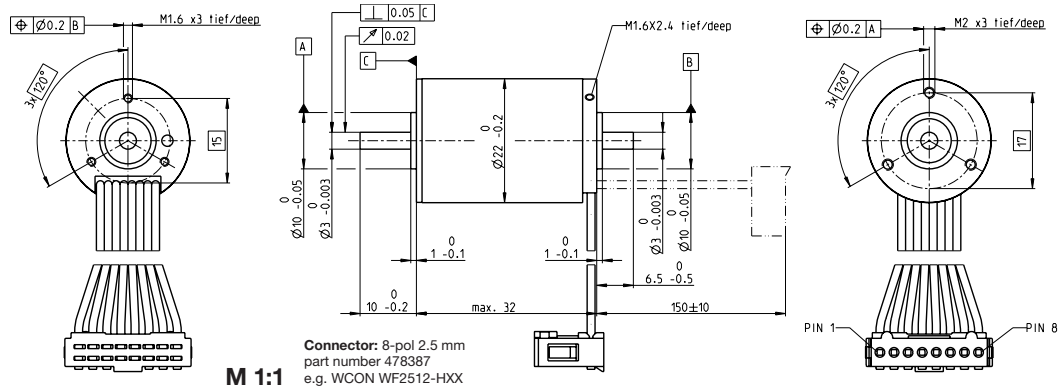

M 1:1

Connector: 8-pol 2.5 mm
part number 478387
e.g. WCON WF2512-HXX

Stock program
Standard program
Special program (on request)

			Part Numbers							
			283837	283838	283839	283840	283841			
Motor Data										
	Values at nominal voltage									
1	Nominal voltage	V	6	12	18	24	36			
2	No load speed	rpm	11400	12100	12100	12100	12100			
3	No load current	mA	282	155	103	77.3	51.6			
4	Nominal speed	rpm	7230	8040	8250	8250	8210			
5	Nominal torque (max. continuous torque)	mNm	10.5	10.2	10.9	10.8	10.6			
6	Nominal current (max. continuous current)	A	2.41	1.25	0.88	0.657	0.432			
7	Stall torque	mNm	30	31.3	35.4	35.1	34.1			
8	Stall current	A	6.23	3.47	2.6	1.94	1.25			
9	Max. efficiency	%	63	63	65	65	65			
	Characteristics									
10	Terminal resistance phase to phase	Ω	0.963	3.46	6.93	12.4	28.7			
11	Terminal inductance phase to phase	mH	0.0343	0.121	0.275	0.488	1.09			
12	Torque constant	mNm/A	4.81	9.02	13.6	18.1	27.2			
13	Speed constant	rpm/V	1990	1060	701	526	352			
14	Speed/torque gradient	rpm/mNm	397	406	356	360	371			
15	Mechanical time constant	ms	9.36	9.56	8.39	8.47	8.75			
16	Rotor inertia	gcm²	2.25	2.25	2.25	2.25	2.25			

Specifications

Thermal data

17	Thermal resistance housing-ambient	13.5 K/W
18	Thermal resistance winding-housing	1.72 K/W
19	Thermal time constant winding	1.69 s
20	Thermal time constant motor	567 s
21	Ambient temperature	-40…+100°C
22	Max. winding temperature	+155°C

Mechanical data (preloaded ball bearings)

23	Max. speed	18000 rpm
24	Axial play at axial load < 4 N	0 mm
	> 4 N	0.14 mm
25	Radial play	preloaded
26	Max. axial load (dynamic)	3.5 N
27	Max. force for press fits (static)	53 N
	(static, shaft supported)	1400 N
28	Max. radial load, 5 mm from flange	16 N

Operating Range

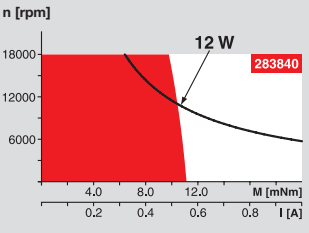

Comments

Continuous operation
In observation of above listed thermal resistance (lines 17 and 18) the maximum permissible winding temperature will be reached during continuous operation at 25°C ambient.
= Thermal limit.

Short term operation
The motor may be briefly overloaded (recurring).

Assigned power rating

B.2 LSM9DS1 9 DOF Data Sheet

life.augmented

LSM9DS1

iNEMO inertial module: 3D accelerometer, 3D gyroscope, 3D magnetometer

Datasheet - production data

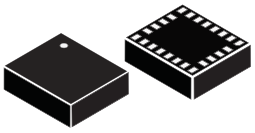

LGA-24L (3.5x3x1.0 mm)

Features

- 3 acceleration channels, 3 angular rate channels, 3 magnetic field channels
- ±2/±4/±8/±16 *g* linear acceleration full scale
- ±4/±8/±12/±16 gauss magnetic full scale
- ±245/±500/±2000 dps angular rate full scale
- 16-bit data output
- SPI / I^2C serial interfaces
- Analog supply voltage 1.9 V to 3.6 V
- “Always-on” eco power mode down to 1.9 mA
- Programmable interrupt generators
- Embedded temperature sensor
- Embedded FIFO
- Position and motion detection functions
- Click/double-click recognition
- Intelligent power saving for handheld devices
- ECOPACK®, RoHS and “Green” compliant

Applications

- Indoor navigation
- Smart user interfaces
- Advanced gesture recognition
- Gaming and virtual reality input devices
- Display/map orientation and browsing

Description

The LSM9DS1 is a system-in-package featuring a 3D digital linear acceleration sensor, a 3D digital angular rate sensor, and a 3D digital magnetic sensor.

The LSM9DS1 has a linear acceleration full scale of ±2*g*/±4*g*/±8/±16 *g*, a magnetic field full scale of ±4/±8/±12/±16 gauss and an angular rate of ±245/±500/±2000 dps.

The LSM9DS1 includes an I^2C serial bus interface supporting standard and fast mode (100 kHz and 400 kHz) and an SPI serial standard interface.

Magnetic, accelerometer and gyroscope sensing can be enabled or set in power-down mode separately for smart power management.

The LSM9DS1 is available in a plastic land grid array package (LGA) and it is guaranteed to operate over an extended temperature range from -40 °C to +85 °C.

Table 1. Device summary

Part number	Temperature range [°C]	Package	Packing
LSM9DS1	-40 to +85	LGA-24L	Tray
LSM9DS1TR	-40 to +85	LGA-24L	Tape and reel

Appendix C

DEA Part Drawings

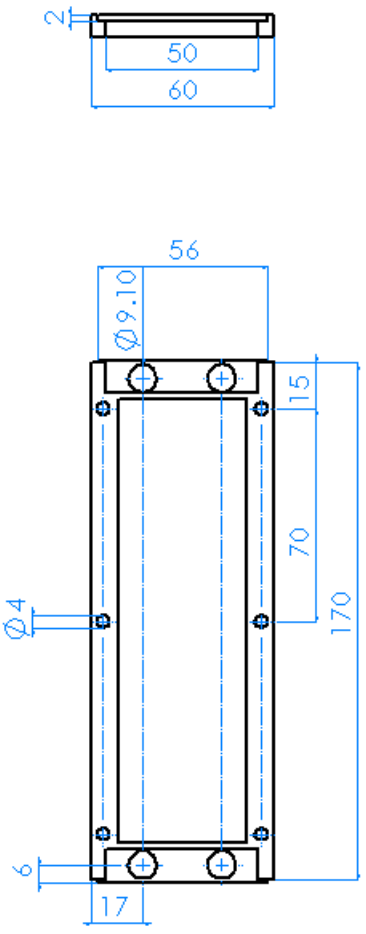

Date: July 4, 2017	Dimensions in mm
Material: Vero Magenta	Part Name: DEA FRAME V3

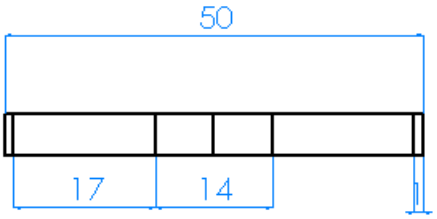

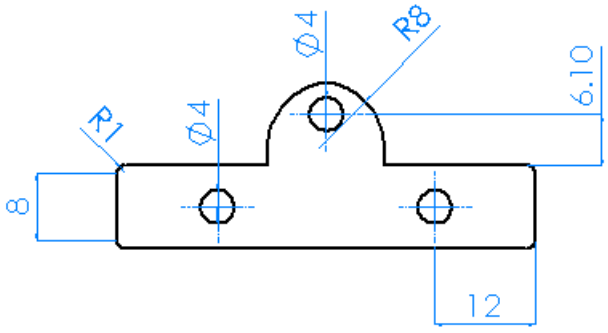

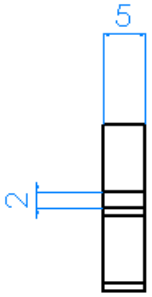

Date: July 4, 2017	Dimensions in mm
Material: Vero Magenta	Part Name: DEA END

Appendix D

Permissions

IOP Publishing LICENSE TERMS AND CONDITIONS

Aug 28, 2017

This is a License Agreement between Myles Lidka ("You") and IOP Publishing ("IOP Publishing") provided by Copyright Clearance Center ("CCC"). The license consists of your order details, the terms and conditions provided by IOP Publishing, and the payment terms and conditions.

All payments must be made in full to CCC. For payment instructions, please see information listed at the bottom of this form.

License Number	4177760297341
License date	Aug 28, 2017
Licensed content publisher	IOP Publishing
Licensed content title	Bioinspiration
Licensed content date	Jan 1, 2006
Type of Use	Thesis/Dissertation
Requestor type	Academic institution
Format	Electronic
Portion	image/photo
Number of images/photos requested	1
Title or numeric reference of the portion(s)	Figure 4
Title of the article or chapter the portion is from	A survey on dielectric elastomer actuators for soft robots
Editor of portion(s)	N/A
Author of portion(s)	Guo-Ying Gu , Jian Zhu , Li-Min Zhu and Xiangyang Zhu
Volume of serial or monograph.	Volume 12
Issue, if republishing an article from a serial	Issue 1
Page range of the portion	10
Publication date of portion	23 January 2017
Rights for	Main product
Duration of use	Current edition and up to 5 years
Creation of copies for the disabled	no
With minor editing privileges	no
For distribution to	Canada
In the following language(s)	Original language of publication
With incidental promotional use	no
The lifetime unit quantity of	Up to 499

VITA

Name:	Myles Lidka
Post-secondary Education and Degrees:	The University of Western Ontario London, Ontario, Canada 2010–2014 B.E.Sc., Mechatronic Systems Engineering
	The University of Western Ontario London, Ontario, Canada 2014–2017 M.E.Sc. Electrical and Computer Engineering
Honours and Awards:	Ontario Graduate Scholarship 2013–2014
	Dean's Honour List 2010–2014
Related Work Experience:	Teaching Assistant *MSE 2201 – Introduction to Electrical Instrumentation* *MSE 3302 – Sensors and Actuators* *MSE 4401 – Robotic Manipulators* The University of Western Ontario 2014–2016
	Research Assistant The University of Western Ontario 2014–2017